Environmental Cracking of Aerospace Aluminum Alloys in High Altitude Environments

---

A Dissertation

Presented to:

The Faculty of the School of Engineering and Applied Science

University of Virginia

In Partial Fulfillment

Of the Requirements for the Degree of

Doctor of Philosophy in Materials Science and Engineering

Prepared by:

Luke B. Brown

July 27th 2022

Abstract

Aluminum alloys have been used extensively in a number of different industries due to their advantageous properties. These properties include high-strength-to-weight ratio, as well as good workability and strong corrosion resistance. In many applications, environmental degradation mechanisms are responsible for a significant number of failures. Recent work has demonstrated that a significant portion of loading for airframe structural components can occur at high altitudes where the environment is typified by low temperatures and low water vapor pressures. At these temperatures and pressures, crack growth kinetics of aluminum alloys are drastically reduced. As such, incorporating low temperature, low water vapor pressure effects into the next generation of airframe structural integrity management has the potential to increase accuracy and reduce over-conservatism.

This dissertation will further explore the effect of a high-altitude environment with a particular focus given to the role low water vapor pressure plays in the fatigue behavior of aerospace aluminum alloys. To this end, four tasks will be explored: (1) Efficacy of water vapor pressure over frequency (P_{H2O}/f) as an exposure parameter to describe the environment. (2) Effect of limiting sample thickness to eliminate irregular crack front behavior at certain stress intensities (ΔKs) and water vapor pressures. (3) Extension of high-altitude behavior in AA 7075 to 2xxx series aluminum alloys. (4) Incorporation of high-altitude fatigue crack growth rates (FCGR) data into linear elastic fracture mechanics (LEFM) based models to determine the magnitude of fatigue life extension.

While researchers had previously studied the role of P_{H2O}/f in describing the environment, this is the first study to comprehensively study this parameter across a wide

range of water vapor pressures in the near-threshold region. Several critical findings on the limitations of using the exposure parameter were found. K-shed testing showed that exposure parameter performed better than water vapor pressure at describing the environmental cracking of 7075. Constant water vapor curves diverged between ΔKs of 4 to 6 MPa√m. Constant K-hold testing revealed two regions, one where water vapor pressure describes the environment, and another where P_{H2O}/f is a better proxy for environmental severity. At low to intermediate water content, the environment appears to be well-described by the P_{H2O}/f exposure parameter. At higher water vapor content, the effect of frequency seems to be diminished, such that water vapor pressure is an adequate descriptor. These results show that while P_{H2O}/f is widely used in literature, and it is the best singular parameter to describe environment, it is important that its limitations are understood.

Literature has previously shown that in certain test conditions, a sharp decrease in growth rates could occur termed the threshold transition regime (TTR). Testing of the TTR this behavior had been suggested to be due to limitations in the transport of water vapor to the crack tip. This was investigated by performing testing on multiple thickness samples to give insights into the possible mechanism controlling this behavior. Varying sample thickness testing did not show any impact on the fatigue crack growth behavior at any water vapor pressures and the fractures surfaces were very similar as well. This invalidates the hypothesis that shrinking the sample thickness the TTR might be eliminated. Modeling efforts using Franc3D confirmed that at as an irregular crack front forms, the stress intensity spikes in the center of the sample, likely resulting in cleavage fracture. Additionally, modeling of constant semi-elliptical cracks on the edge of the sample for different thicknesses are not consistent with experimental results. This indicates that the irregular crack front is unique for each sample thickness. Further work is needed to give insight into how the irregular crack front develops in order to better explain why changing sample thickness had no effect on the TTR behavior.

Environmental fatigue testing of aluminum alloy 2199 in high altitude environments established over a wide range of ΔK was performed. Reduction of P_{H2O} at 23 °C resulted in a systematic reduction of crack growth rates, resulting from a reduction in H needed for the hydrogen embrittlement process. Above 165 Pa, changes in P_{H2O} do not result in increased crack growth rates, indicating the environmental contribution reaches a saturation point. At 0.5 Pa FCGR matched those at ultra-high vacuum (UHV), indicating that at these low pressures, there is no longer any environmental contribution to cracking. Low-temperature testing showed that at temperatures above -15 °C no change in FCGR was observed. Decreased crack rates were observed at -30 °C and -50 °C. When temperature was again lowered to -65 °C at 0.5 Pa, temperature had no effect on crack behavior indicating that temperature is affecting environmental cracking only. This behavior was suggested to be due to dislocation interactions with H changing as temperature decreased.

Utilizing an LEFM program, AFGROW, the environmental effect on fatigue life on AA 7075-T651 in aerospace applications was able to be quantitatively predicted. Through several different modeling conditions, the fatigue life in low water vapor environments consistently produced significant increases in fatigue life. At low stresses, the relative change in fatigue life was greater across all different modeling conditions. While environmental effects are most potent in the near-threshold regime of the da/dN vs. ΔK relationship, targeted modeling demonstrates that the majority of the crack extension occurs at high stresses (thus high ΔK).

This leads to the counter-intuitive conclusion that, despite the lower relative impact of environmental on the da/dN at high ΔK, the environmental effect at high stress levels has a more significant impact on the total fatigue life. Through these results, it is clear that implementation of low water vapor pressure, low temperature, environmental FCGR into the next generation of airframe structural integrity management models can have a profound impact.

Table of Contents

Contents

Abstract i

Table of Contents v

List of Tables viii

List of Figures viii

Chapter 1 – Introduction to Low Water Vapor Environment 13

1.1 Motivation 13

1.2 Mechanisms 14

1.2.1 Hydrogen Embrittlement 14

1.2.2 Environmental Damage Process Model 15

1.3 Effect of Exposure on Fatigue Crack Growth 20

1.4 Threshold Transition Regime 22

1.5 Research Tasks 24

Chapter 2 – Verification of P_{H2O}/f as an Environmental Exposure Parameter 28

2.1 Introduction 28

2.1.1 Literature Overview 28

2.1.2 Test Matrix 29

2.2 Experimental 30

2.2.1 Material 30

2.2.2 Loading Protocol 30

2.2.3 Environmental Control 33

2.3 Results 33

2.3.1 ΔK-shed Loading Experiments 33

2.3.2 Constant ΔK Experiments 35

2.4 Discussion 37

2.4.1 Exposure Parameter Describing K-shed Data 37

2.4.2 Exposure Parameter Describing Constant ΔK Data 38

2.4.3 Exposure Parameter Versus Water Vapor Pressure 40

2.4.4 Impact on Process Zone H Diffusion Limited Hypothesis 41

2.4.5 Implication on Applying an Environmental Parameter in LEFM Models 45
2.5 Conclusions 49
Chapter 3: Investigation into the Factors Effecting the Threshold Transition Regime 51
3.1 Introduction 51
3.2 Experimental 53
3.3 Results 54
3.4 Discussion 58
3.4.1 Review of Previous Experimental Results Relating to the TTR 58
3.4.2 Development of the irregular crack front 65
3.4.3 Modeling of ΔK Profile for an irregular crack front 66
3.4.4 Modeling of Constant Size Semi-Elliptical Edge Cracks in the TTR 70
3.5 Conclusions 73
Chapter 4 Effect of Low Temperature, Low Water Vapor Pressure Environments on the Fatigue Behavior of an Al-Li Alloy 74
4.1 Introduction 74
4.1.1 motivation for the study of 2199 74
4.1.2 Effect of Temperature on FCGR 75
4.1.3 Research Goals 75
4.2 Experimental: 76
4.2.1 Material 76
4.2.2 Loading Protocol 77
4.2.3 Environmental control 77
4.3 Results 79
4.3.1 Comparison of 7075 and 2199 aluminum alloys at high humidity and UHV 79
4.3.2 Fatigue crack growth rates versus ΔK at variable P_{H2O} 81
4.3.3 Analysis of fracture surface 85
4.3.4 Effect of temperature on fatigue crack growth rates versus ΔK at variable P_{H2O} 92
4.4 Discussion 94
4.4.1 Transport Limitation Induced TTR in 2199 95
4.4.2 Alloy Specific TTR Behavior in 2199 97
4.4.3 Effect of temperature on crack growth 99

4.5 Conclusions 104
Chapter 5 – Incorporation of High-Altitude Environmental Effects in the LEFM-based Modeling of Aluminum Alloy 7075 106
5.1 Introduction: 106
5.1.1 Overview of Current Approaches to Fatigue Life Estimates 106
5.1.2 Current Growth Rates Being Applied in Fatigue Life Models 107
5.1.3 Required Components for LEFM Models 108
5.1.4 Research Goals 109
5.2 Experimental Methods 110
5.2.1 High Altitude da/dN vs. ΔK Relationships 110
5.2.2 Modeling Condition 1: Constant Stress, Constant Environments 113
5.2.3 Modeling Conditions 2: Variable Stress, Variable Environment 114
5.2.4 Modeling Condition 3: ENSTAFF Generalized Load-Environment Spectrum 115
5.2.5 Modeling Condition 4: Boeing 707 Wing Station 360 Spectrum 117
5.2.6 Modeling Condition 5: Commercial Jet Wing Spectrum 120
5.3 Results 120
5.3.1 Modeling Condition 1: Constant Stress, Constant Environments 120
5.3.2 Modeling Condition 2: Variable Stress, Variable Environments 122
5.3.3 Modeling Condition 3: ENSTAFF Generalized Load-Environment Spectrum 123
5.3.4 Modeling Conditions 4 and 5: Boeing 707 and Business Jet 126
5.4 Discussion: 128
5.4.1 Stress Level Dependent Environmental Fatigue Impact 128
5.4.2 Modeling of Real-world Airframe Components 131
5.4.3 Opportunities and Challenges 133
5.5 Conclusions: 135
Chapter 6 – Final Conclusions 137
Acknowledgments 139
References 140

List of Tables

Table 1: Aluminum alloy 7075 composition (Wt %).. 30
Table 2: Test matrix for constant ΔK testing. Colored exposure parameters are done to easily reference which tests have identical exposure parameters 32
Table 3: The average absolute value of the slope of da/dN vs frequency graph of each of the constant water pressure (left side) and constant exposure curves (right side), as well as the average standard deviation of da/dN at each constant water vapor pressure or constant exposure parameter These where then divided into two regions for each graph, low water content (blue shading), and high-water content (orange shading). The slope was multiplied by 10^8 and the standard deviation by 10^6 to ease in understanding 40
Table 4: Aircraft fatigue load cycle frequencies[62] 47
Table 5: Aluminum alloy 2199 composition (Wt %).. 77
Table 6:The ΔK at threshold for various water vapor pressures. 82
Table 7: The temperature of and water vapor pressures at altitudes relevant to airframe operation. The water vapor pressure for each temperature corresponds to the vapor pressure above ice for of the temperatures listed. 113
Table 8: Stress and environment spectrum for modeling Condition 1 for both high humidity and mixed environment conditions. FCGR for each water vapor pressure (shown in Figure 34) were then applied appropriately applied according to this table. This loading spectrum was repeated until crack growth reaches a free surface or K max for the material was exceeded................. 115
Table 9: Comparison of structure temperature and corresponding water vapor content with actual water vapor pressure FCGR utilized for ENSTAFF spectrum. This data was previously generated and shown in Figure 34 116
Table 10: Cycles to failure for modeling Condition 3 at a variety of stresses for both mixed da/dN and high humidity FCGR data as well as the relative difference between them. 125
Table 11: Load and environmental spectrum for modeling Condition 6. σ is a stress that can be varied (σ = 50 MPa and 100 MPa for this study) 130

List of Figures

Figure 1: $(da/dn)_{cf}$ vs P_{H2O}/f for AA 2219 for water environments[15] 19
Figure 2: Room temperature growth rates of AA 7075 plotted versus exposure parameter, P_{H2O}/f, for several different constant ΔK at R = 0.5, f = 20 Hz[10] Solid lines are fit to the data and reflect theoretically based models.[40,53]... 21
Figure 3: Crack growth rate versus ΔK (a) from K-shed fatigue testing of 7075-T651 at various P_{H2O} values at R of 0.5 and a frequency of 20 (or 2) Hz. Corresponding optical fractography is presented for the 0.2 (b), 0.5 (c), and 1.8 (d) Pa exposures where the solid, dashed, and dotted lines locate the crack location at given ΔK values in (a) 23
Figure 4: Room temperature growth rates of AA 7075 plotted versus exposure parameter, P_{H2O}/f, for several different constant ΔK at R = 0.5, f = 20 Hz[10] Solid lines are fit to the data

and reflect theoretically based models.[40,53] Vertical lines mark exposures tested at constant ΔK 33
Figure 5: da/dN vs ΔK for the PH2O testing matrix. Each graph tests that either contain a constant exposure parameter (P_{H2O}/f) or constant water vapor pressure. 35
Figure 6: Constant Δk of 6 MPa√m at several constant water vapor pressure growth rates versus exposure parameter. 40.5 Pa had two tests, one with a crack length of 32-35 mm (long) and one at 15-18 mm (long) 36
Figure 7: Constant ΔK of 6 MPa√m at several constant exposure parameters growth rates versus water vapor pressure 37
Figure 8: The concentration of H, C_H is shown as a function X, distance from the crack tip. This is done for three different frequencies and for low-water content (dependent on frequency) and high-water content (independent of frequency). Below the max stress is graphed versus X as well. The critical concentration of H for crack extension to occur, C_H^*, is shown (purple line) as a flat line to ease understanding, but this will actually vary as the max stress also varies. 43
Figure 9: The concentration of H, C_H is shown as a function X, distance from the crack tip. This is done for three different frequencies and for high-water content and max experimental-water content. Below the max stress is graphed versus X as well. The critical concentration of H for crack extension to occur, C_H^*, is shown (purple line) as a flat line to ease understanding, but this will actually vary as the max stress also varies. 45
Figure 10: da/dN versus ΔK relationship (A) for thick medium and thin specimens in an UHV environment. Optical fractography of the thick, medium, and thin specimens are shown in B, C, and D. Orange lines marks onset of SBC. (Image created by Adam Thompson) 54
Figure 11: da/dN versus ΔK relationship (A) for thick medium and thin specimens at 0.675 Pa. Optical fractography of the thick, medium, and thin specimens are shown in B, C, and D. Orange lines marks onset of SBC, blue lines mark the bottom of the TTR, and the yellow lines mark the top of the spike after the false threshold. (Image created by Adam Thompson) 56
Figure 12: da/dN versus ΔK relationship (A) for thick medium and thin specimens at 0.54 Pa. Optical fractography of the thick, medium, and thin specimens are shown in B, C, and D. Orange lines marks onset of SBC, blue lines mark the bottom of the TTR, and the yellow lines mark the top of the spike after the false threshold. (Image created by Adam Thompson) 56
Figure 13: da/dN versus ΔK relationship (A) for thick medium and thin specimens at 38 Pa. Optical fractography of the thick, medium, and thin specimens are shown in B, C, and D. (Image created by Adam Thompson) 57
Figure 14: da/dN versus ΔK relationship (A) for thick medium and thin specimens at 2668 Pa. Optical fractography of the thick, medium, and thin specimens are shown in B, C, and D. (Image created by Adam Thompson) 57
Figure 15: Marker bands produced during a K-shed loading protocol at 0.54 Pa. The crack front deduced via marker bands is shown in black while the measured crack length according to compliance measurments is indicated in blue. Marker bands were performed at ΔK of 5, 4, and 3 MPa√m. Crack growth occurs from left to right.[27,28,54] 59

Figure 16: (a) FCGR versus crack length at a constant ΔK 5 MPa√m at 0.54 Pa. 0.5 mm of surface roughness was introduced onto the surface before the beginning of the test. (b) Optical fractography of the sample. This crack lengths in the graph correspond to the optical image.[27,28,54] 61
Figure 17: (a) FCGR versus crack length at a constant ΔK 5 MPa√m at 0.54 Pa. 3.0 mm of surface roughness was introduced onto the surface before the beginning of the test. (b) Optical fractography of the sample. This crack lengths in the graph correspond to the optical image.[27,28,54] 62
Figure 18: (a) FCGR versus crack length at a constant ΔK 3 MPa√m at 0.54 Pa. no surface roughness was introduced onto the surface before the beginning of the test. (b) Optical fractography of the sample. This crack lengths in the graph correspond to the optical image. [27,28,54] 63
Figure 19: FCGR versus ΔK for both K-shed and K-rise loading protocol at 0.675 Pa. Fracture surface of the K-shed (b) and K-rise (c) are shown. For (b). orange lines indicate the start of roughness, the blue line indicates the local minima, and yellow lines mark the local maxima. For (c), blue lines represent the local maxima.[59] 64
Figure 20: Stress intensity across the entire crack width at a target ΔK of 5 MPa√m and an R of 0.5. The crack shape is shown above the curve marked in red with the crack growing from left-to-right 68
Figure 21: Stress intensity across the entire crack width at a target ΔK of 4 MPa√m and an R of 0.5. The crack shape is shown above the curve marked in red with the crack growing from left-to-right 69
Figure 22: Stress intensity across the entire crack width at a target ΔK of 3 MPa√m and an R of 0.5. This was done for both the irregular crack front and a through crack. The crack shape is shown above the curve marked in red with the crack growing from left-to-right and the through crack marked in blue 70
Figure 23: Modeling of thick, medium, and thin stress intensities with a constant sized, semi-elliptical crack on each edge using Franc3D. Simulated loading occurred at a ΔK of 4 MPa√m and a R ratio of 0.5 72
Figure 24: Fatigue crack growth rates versus ΔK from K-shed testing comparing 2199 and 7075-T651 aluminum alloys in UHV and high humidity environments at room temperature. 80
Figure 25: Crack growth rates versus ΔK from K-shed testing of 2199 at various P_{H2O}. R of 0.5, and a frequency of 20 Hz (unless noted) at room temperature. Side-grooved samples are indicated as (SG). 165 Pa, plot is a combination of side-grooved (above ΔK = 4.8 MPa√m) 82
Figure 26: Room temperature growth rates plotted versus exposure parameter, PH2O/f for several different constant ΔKs. A trend from a separate lot of 2199 at 7 MPa√m, R=0.58, and f=20 Hz[42] at various exposures (black line) 84
Figure 27: Optical fractography of the fracture surface of side grooved samples at 23 ◦C for UHV (a), 0.05 Pa (b), 1.8 Pa (c), 4 Pa (d), 18 Pa (e), and 38 Pa (f). Red boxes indicate the area cracked during the K-shed. Black lines locate the crack position at ΔK of 9 (solid), 7 (dashed) and 5 (dotted) MPa√m 87

Figure 28: Crack growth rate versus ΔK and corresponding optical fractography and SEM micrographs illustrating the transition from smooth to rough topography on the fatigue crack surface of 2199 at 4 Pa. ΔKs of interest are marked both on the graph and on the fracture surface. The green line indicates the start of the K-shed after the precrack. 88
Figure 29: SEM images of the fatigue crack surface of 2199 tested at constant R = 0.5, f = 20 Hz and constant ΔK = 9 MPa√m for an L-T oriented specimen exposed to PH2O of: UHV (a), 0.5 Pa (b), 1.8 (c), 4 (d), 18 (e), 38 (f), and 2668 Pa (g). Crack growth is from left to right in each image. (Figure created by Jenny Jones) 90
Figure 30: SEM images of the fatigue crack surface of 2199 tested at constant R = 0.5, f = 20 Hz and constant ΔK = 7 MPa√m for an L-T oriented specimen exposed to PH2O of: UHV (a), 0.5 Pa (b), 1.8 (c), 4 (d), 18 (e), 38 (f), and 2668 Pa (g). Crack growth is from left to right in each image. (Figure created by Jenny Jones) 91
Figure 31: SEM images of the fatigue crack surface of 2199 tested at constant R = 0.5, f = 20 Hz and constant ΔK = 5 MPa√m for an L-T oriented specimen exposed to PH2O of: UHV (a), 0.5 Pa (b), 1.8 (c), 4 (d), 18 (e), 38 (f), and 2668 Pa (g). Crack growth is from left to right in each image (Figure created by Jenny Jones) 92
Figure 32: Crack growth rates versus ΔK at constant R of 0.5, f of 20 Hz for 2199 with varying temperature from 23 ◦C to -65 ◦C. Side-grooved samples are indicated as (SG). 23 ◦C, 165 Pa, plot is a combination of side-grooved (above ΔK = 4.8 MPa√m) and standard thickness (below ΔK = 4.8 MPa√m) 94
Figure 33: Crack growth rates versus ΔK at constant R of 0.5, f of 20 Hz and standard thickness for 2199 at 38 Pa for both 23 ◦C and -30 ◦C. Optical fractography of both 23 ◦C (a) and -30 ◦C (b) are shown as well. Red boxes indicate the area cracked during the K- shed. Black lines locate the crack position at ΔK of 9 (solid), 7 (dashed) 5 (dotted), and 3 (dash-dot) MPa√m on both the fracture surfaces and on the growth rate graph. 102
Figure 34: Experimental data truncated to 30 data points for application into AFGROW growth rate tabular input. Da/dN data was generated using K-shed loading protocol at an R=0.5 and a frequency at 20 Hz (unless otherwise noted) 111
Figure 35: Initial specimen design for modeling conditions 3 and 6 is shown. A surface center elliptical flaw in a bar where the width (W) and length (L) are 7.62 mm for condition 3 and 100 mm for condition 6. The initial flaw has parameters A and C of 0.5 mm for both condition 3 and condition 6. (Definitions of A and C are shown) 115
Figure 36: Boeing 707 Load-Environment spectrum. 118
Figure 37: AFGROW model for Boeing 707 and business jet crack life predictions. From top to bottom, double corner crack at holes specimen design, spectrum preview, model inputs. 119
Figure 38: Business Jet Load-Environment Spectrum 120
Figure 39: Modeling Condition 1: Max stress (MPa) versus cycles to 1.5 mm crack length for constant load, constant environment model. This was done at a variety of water vapor pressures and max stresses and are shown here. 121
Figure 40: Modeling Condition 2: Crack growth versus cycles for an arbitrary variable load and environment loading condition. Constant water vapor pressure (green) utilized da/dN data

generated at 2668 Pa while the variable water pressure curve (red) utilized da/dN from a variety of pressures, detailed in Table 7. The blue curve represents the stress at each cycle and high stresses can be seen to correspond with large jumps in crack length. 123
Figure 41: Modeling Condition 3: Crack growth versus cycles to failure for realistic loading-environment spectrum for a general fighter generated from ENSTAFF. High humidity curves (orange) utilized da/dN data from 2668 at all cycles. Realistic pressures curves (blue) utilized da/dN a variety of da/dN curves based on ENSTAFF environmental temperature data and relating these temperatures to an altitude and then a corresponding pressure detailed in Table 5. This was repeated for max stresses of 50 MPa (A), 100 MPa (B), 200 MPa and 300 MPa (C). 126
Figure 42: Comparison in inspection intervals for the Boeing 707 using the environmental/mechanical loading spectrum compared to laboratory air fatigue crack growth rates, based on cycles to critical crack length using AFGROW models. 127
Figure 43: Comparison in inspection intervals for the business jet using the environmental/mechanical loading spectrum compared to laboratory air fatigue crack growth rates, based on cycles to critical crack length using AFGROW models. 128
Figure 44: Modeling Condition 6: Crack length versus cycles for study on the effects of low water vapor pressure at high or low stresses. The legend details which environment is assigned at each of the stress levels (shown in Table 9), and what σ is equal to (50 MPa in A, 100 MPa in B). The first pressure corresponds with 1000 cycles at 0.5 σ and the second pressure with 30 cycles at σ. 130

Chapter 1 – Introduction to Low Water Vapor Environment

1.1 Motivation

Aluminum alloys have been used extensively in a number of different industries due to their advantageous properties. These properties include high strength to weight ratio, good workability, as well as strong corrosion resistance. In many applications, environmental degradation mechanisms are responsible for a significant number of failures.[1–4] To properly manage the structural integrity of these alloys in-service, the effect of the in-service environment needs to be understood and incorporated into life management techniques. This research effort will focus on high altitude environments, which are critical environments for these applications.

Recent work has demonstrated that a significant portion of loading for airframe structural components can occur at high altitudes where the environment is typified by low temperatures and low water vapor pressures.[5] Analyses of the primary wing loads for transport aircraft shows that [6][7] 17% of these loads occur at or above 9150 m and 42% of these loads occur at or above 3050 m.[7] Similarly, cabin pressurization loads for commercial aircraft are estimated to start at 2450 m and continue to increase until the cruising altitude of roughly 12,200 m.[8] These examples suggest that significant loading occurs in high altitude environments where the temperature can range from-5 °C (at 3000m) to -60 °C (at 15,000 m).[9] The ambient water vapor pressure at these altitudes is also expected to decrease.[10–12] At these temperatures and pressures, crack growth kinetics of aluminum alloys are drastically reduced.[5,10,20,21,11,13–19] As such, incorporating low temperature, low water vapor pressure effects into the next generation of airframe structural integrity management has the potential to increase accuracy and reduce over-conservatism.[22] Functionally, this is accomplished by incorporating environmental effects into linear elastic fracture mechanics (LEFM) models that inform damage-tolerant based structural integrity management strategies.[22] To do so, environment specific fatigue crack growth rate (FCGR; da/dN) versus stress intensity (ΔK) relationships must be used as inputs to the LEFM models that predict crack progression. The successful application of these approaches requires (1) a coupled load-environment spectrum that accurately reflects the component conditions, (2) a rigorous testing protocol that generates environment specific growth kinetics that exhibit similitude with the operational component, and (3) a software interface, (such as AFGROW) that will allow integration of the environment specific growth rates. Coupled load-environment spectra can be gathered from inflight sensors or flight profiles from operational components[6,7,23–25] or generalized spectrum.[26] However, ensuring that laboratory generated environmental da/dN vs. ΔK relationships exhibit similitude with component conditions is challenging and requires a detailed understanding of the environmental cracking process that goes beyond standard fracture mechanics considerations. This research will investigate knowledge gaps in (2) and (3).

1.2 Mechanisms

1.2.1 Hydrogen Embrittlement

Significant literature efforts have been performed to quantify the low moisture environmental cracking behavior of aerospace Al-alloys,[5,10,13,15,16,27–31] to gather mechanistic understanding of these behaviors,[32–35] to generate models that quantitatively describe these mechanisms,[36–41] and to postulate how these mechanisms impact the data generation process[10,27,30,40,42,43]. The mechanism by which moist gaseous environments increase fatigue crack growth is hydrogen environment embrittlement (HEE).[15,35,44–46] In this process, water molecules react with the aluminum surface at the crack tip to produce atomic hydrogen which then diffuses into the crack tip process zone to cause embrittlement. The exact mechanism governing this embrittlement is controversial.[13,35,47] Many different proposed mechanisms have been proposed for different alloy systems.[48] Hydrogen-Enhanced Localized Plasticity (HELP), Hydrogen-Enhanced Decohesion (HEDE), and Hydrogen and Deformation-Assisted Vacancy Production are some of the mechanisms of particular interest.[48] HELP relies on the solute hydrogen atoms increasing the development and movement of dislocations around the crack tip. This can be accomplished by increasing the dislocation nucleation and the dislocation velocity.[49] This is potentially accomplished via hydrogen shielding the dislocations from high stress fields in certain directions, lowering the stress required to move in these directions.[50] Meanwhile, in HEDE, the presence of hydrogen solutes in the lattice stretch and weaken the solvent metal bonds and/or reduce the cohesion energy between grain boundaries.[48] These then lead to a decrease in the stress required for brittle rupture, resulting in decohesion.

Regardless of the specific mechanism at work, the HEE process involves several important time dependent steps (1) water molecular transport from the bulk environment to the crack tip, (2) the rate of the surface reaction, (3) H diffusion from the crack tip to the crack tip process zone, and finally, (4) H-plasticity/stress interaction in the process zone.[15,16,52,29–31,33,37,39,41,51]

1.2.2 Environmental Damage Process Model

These four steps in the HEE process were further investigated by R. P. Wei, as well as other researchers, who attempted to quantify this process and determine the rate limiting steps.

By examining the data that had previously been published, Wei was able to determine that crack growth was controlled by either the rate of surface reaction or by the rate of transport and concluded that neither H diffusion or H plasticity interactions were controlling.[36] In 1980, Wei developed a model for environmental cracking for two conditions, one where the surface reaction is the rate limiting step, and one where the transport of water molecules is limiting.[38] Wei began by assuming that the water vapor was transporting to a reactive surface, reacting at the surface to produce H which is then adsorbed into the aluminum.[41] H then diffuses to the crack tip process zone where it embrittles the alloy. A critical assumption of this approach is that the diffusion and embrittlement are not rate limiting compared to water vapor transport or the surface reactions. Additionally, the "reactive surface" only appears at the newly cracked surface, whereas all other aluminum surfaces have reacted with oxygen to form aluminum oxide which inhibits H adsorption. Finally, he assumes that the FCGR is proportional to the exposed surface area multiplied by the extent of surface reaction.

While Wei developed a model for both surface reaction limited and transport limited, only transportation limited will be closely examined. A very similar process is followed for a surface reaction limited model. One of the critical and unique aspects of this problem is the transport of water molecules from the bulk environment to the crack tip. Wei began by assuming this transport was governed by Knudsen flow and developed the following equation:[15]

$$\frac{dp}{dt} = \frac{-SN_oRT}{V}\frac{d\theta}{dt} + \frac{F}{V}(p_o - p)$$

(1)

S is equal to the area of the newly created crack tip per cycle = [α(2BΔa)] where Δa is the crack growth per cycle, B is the specimen thickness, and α is a constant that accounts for the surface roughness and crack geometry. N_o is the available sites per surface area, R is the gas constant, and T is the temperature in Kelvin. V is the volume at the crack tip, p is the pressure at the crack tip, and p_0 is the bulk water vapor pressure. F is a Knudsen flow parameter dependent on the molecular weight of the vapor species, the temperature, capillary action, as well as empirical crack growth data.[15] $\frac{d\theta}{dt}$ is the rate of surface reaction and is given by the following formula:

$$\frac{d\theta}{dt} = k_c p(1-\theta)$$

(2)

K_c is the reaction rate constant, p is the crack tip pressure, and θ is the fractional surface coverage. These equations were then combined and solved for the pressure at the crack tip and inserted into equation 2 which was then integrated to yield the following:

$$\theta \approx \frac{F}{SN_oRT} p_o t$$

(3)

Wei assigns $t = 1/2f$ (where f is the frequency of loading) assuming that the surface reaction can only occur during the active loading portion of a sine wave loading profile as during the unloaded portion the crack tip will close, blocking the reactive surface. This results in the extent of reaction θ, being proportional to the bulk pressure and inversely proportional to the loading frequency and the crack extension, Δa (from the S term). It is important to remember, however, that θ is the extent of reaction per surface area, so in order to calculate the total hydrogen adsorbed, θ needs to be multiplied by Δa, which removes crack length extension dependance.

Based on superposition, the total fatigue crack growth rate can be broken down into the inherent mechanical crack advance independent of environment and then an environmental fatigue portion. It was hypothesized that this environmental fatigue damage is proportional to the total adsorbed hydrogen in the alloy, yielding the following equation:

$$\left(\frac{da}{dN}\right)_{cf} = \left(\frac{da}{dN}\right)_{e} - \left(\frac{da}{dN}\right)_{r} \propto \frac{F}{SN_oRT}\frac{p_o}{2f}$$

(4)

With $(da/dn)_{cf}$ being the environmental contribution to FCGR, $(da/dn)_{e,}$ the total FCGR in an aggressive environment, and $(da/dn)_{r,}$ the FCGR in an inert environment. This result is only relevant when θ < 1. If θ approaches 1, the sample becomes saturated, and the reaction rate determines the amount of H adsorbed. In this condition, the following equation would be governing:

$$\left(\frac{da}{dN}\right)_{cf} = \left(\frac{da}{dN}\right)_{e} - \left(\frac{da}{dN}\right)_{r} \propto \Delta a\left(1 - exp\left(-k_c\frac{p_o}{2f}\right)\right)$$

(5)

The two dependencies should result in linear dependence of $(da/dn)_{cf}$ versus p/f below saturation until it transitions when a saturation pressure is reached. This is exactly what Wei saw in comparing the corrosion fatigue rate of AA 2219-T851 in water vapor as well as in distilled water (saturated).

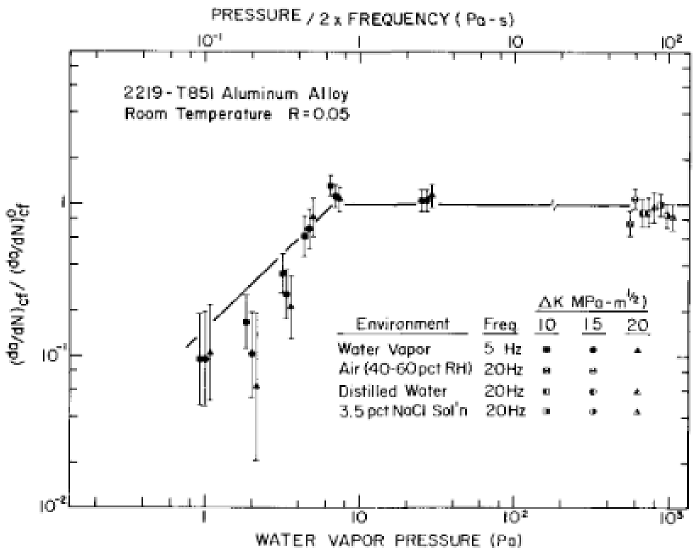

Figure 1: $(da/dn)_{cf}$ vs P_{H2O}/f for AA 2219 for water environments[15]

This result showed that indeed these models have relatively good agreement with the data and could be used as a basis for further study into the mechanism of aluminum alloys in water vapor environments. Further work was done to expand this model to conditions where an inhibitor gas is competing with the embrittling species,[38] as well as determining the effect that yield strength and surface roughness have in changing the saturation transition pressure in water vapor.[30]

While these models do not fully describe some of the complicated behaviors that can be observed in aluminum alloys in this environment, they do model the general behavior that is seen and are still in use in the field 40 years later. These models helped to establish P_{H2O}/f as an exposure parameter to describe the environmental severity.[13,15,16,31,36]

1.3 Effect of Exposure on Fatigue Crack Growth

Based on the pioneering work by Wei, growth rate data from moist gaseous environments are often plotted at a constant ΔK against P_{H2O}/f, as demonstrated in Figure 2.[10] This figure shows three distinct behaviors. First, at low exposures, there is no hydrogen embrittlement, as there is not enough water vapor to begin this process. As such, all observed crack growth is purely mechanical, and no environmental cracking is occurring. At intermediate exposures, the hydrogen embrittlement process has started, and it is governed by molecular transport to the crack tip.[10] This region has a steep slope, and its growth rate is strongly dependent on the environmental exposure. Finally, at high water vapor pressure, there is a change in slope to a very minimal exposure dependence on da/dN. This has been suggested that there is a change in the rate limiting step to H diffusion from the crack tip to the process zone.[53]

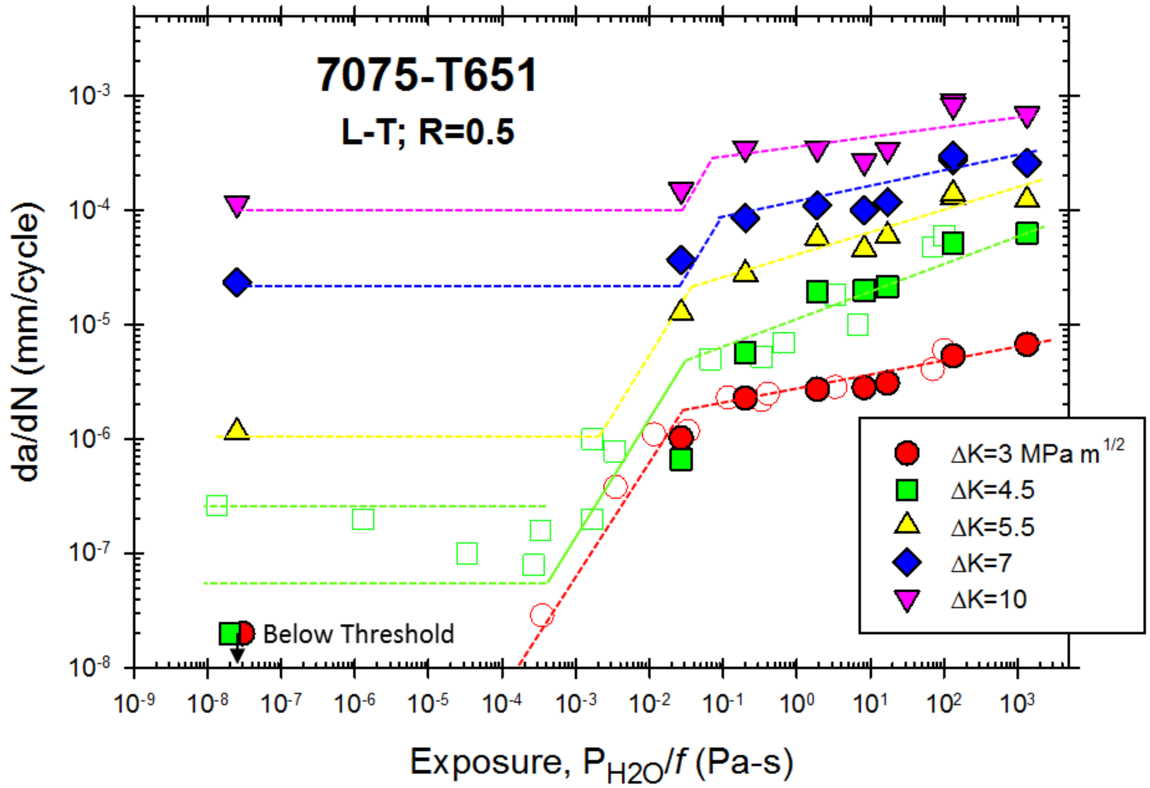

Figure 2: Room temperature growth rates of AA 7075 plotted versus exposure parameter, P_{H2O}/f, for several different constant ΔK at R = 0.5, f = 20 Hz[10] *Solid lines are fit to the data and reflect theoretically based models.*[40,53]

It is helpful to recognize the region in which you are testing/operating when analyzing environmental cracking behavior of 7075 since each region has its own rate limiting mechanism. As such, the expected behavior and dependencies on variables (e.g., loading frequency, stress intensity level, etc.) will vary between cracking regimes. This emphasizes the importance of testing protocol and experimental design when generating data for input into LEFM modeling approaches. P_{H2O}/f appears to be a good proxy for environmental severity for aluminum alloys. However, there is limited research attempting to verify this claim, particularly near ΔK threshold. Further research is needed before P_{H2O}/f can be verified as the best proxy for environment, though current findings are promising.

1.4 Threshold Transition Regime

The above discussion establishes that P_{H2O}/f is an effective environmental parameter for environmental severity for well controlled fracture mechanics samples. However, for non-ideal testing with conditions where molecular transport is hypothesized to be the rate controlling step, the flow path may impact the environmental crack growth data for use in LEFM based modeling for engineering components for two reasons. First, there will likely be differences in transport path geometry (e.g., CT sample versus a thumbnail crack) between a laboratory specimen and a crack in an operational component. Second, molecular flow will intrinsically be impacted by the channel dimensions, roughness, and fluctuation due to the loading protocol (e.g., as a function of R-value). Critically, there is a transition from flat-transgranular cracking to tortuous slip-band cracking (SBC) at low values of P_{H2O}/f regimes and low-to-intermediate ΔK values in 7075-T651.[28,54] This is important for LEFM modeling, as changes in one of these two can impact the growth rates in the transport controlled region.

Considering the latter, decreasing ΔK testing in low water vapor environments demonstrates that at intermediate ΔK and water vapor pressures, there is a severe drop in growth rate, followed by a rapid spike, shown in Figure 3 at 0.5 Pa and 0.2 Pa.[13,27,28,54] It has been hypothesized that this behavior is caused by the change in fracture morphology to a rougher fracture surface induced by a change in cracking mechanism.[28] This rough surface then impedes the flow of water vapor from the bulk environment to the crack tip.[28] This in turn, reduces the environmental cracking contribution, resulting in a decrease in da/dN. After marker band testing and fracture surface analysis, it appeared that an irregular crack front developed and the crack increased at a much greater rate on the sides of the sample than in the center[28,54]. Again, this was hypothesized that the rough crack wake impeded molecular flow down the center of the sample, while flow from the crack flanks allowed the aggressive environment cracking to continue at a faster rate.[28] This finally results in an increased stress intensity in the center of the sample which causes the crack to "snap" forward, which is seen in the growth rate spike.[27]

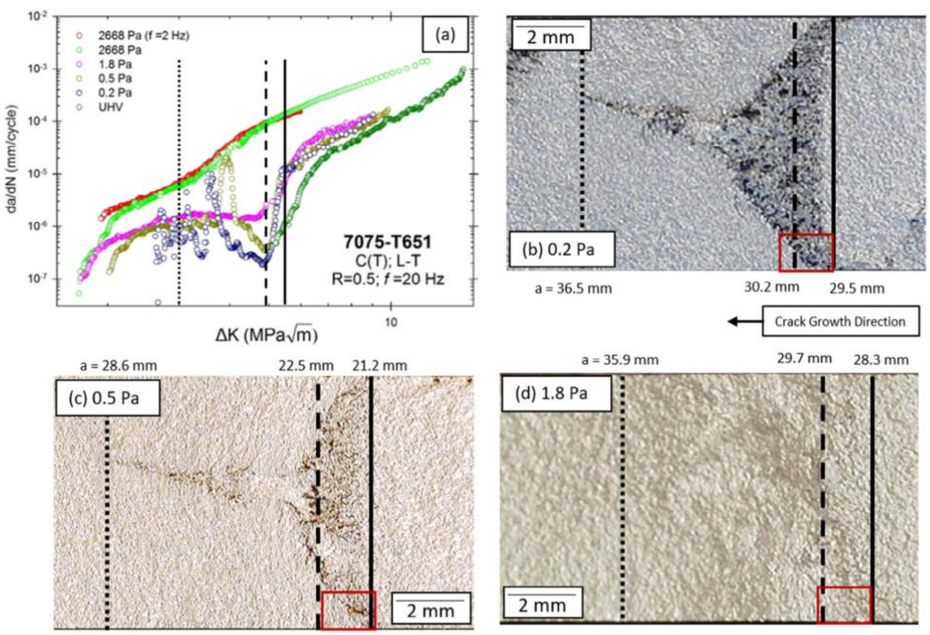

Figure 3: Crack growth rate versus ΔK (a) from K-shed fatigue testing of 7075-T651 at various P_{H2O} values at R of 0.5 and a frequency of 20 (or 2) Hz. Corresponding optical fractography is presented for the 0.2 (b), 0.5 (c), and 1.8 (d) Pa exposures where the solid, dashed, and dotted lines locate the crack location at given ΔK values in (a)

The TTR behavior can complicate generation of da/dN versus ΔK curves for implementation into fatigue life models. Eliminating the TTR would allow for these growth curves to be generated without issue and would aid in implementing high altitude environments into the next generation of fatigue life modeling.

1.5 Research Tasks

In order to implement high altitude environment growth rates in fatigue life estimates, it is crucial that all required inputs be investigated and understood. First, a parameter that accurately describes the environmental parameter is needed. As discussed previously, P_{H2O}/f is the parameter that is currently used to do this. However, more testing is needed to verify that this parameter is consistent across a range of testing conditions.

Once the environment is properly described, da/dN versus ΔK data needs to be generated across a wide range of these environments. Currently, the TTR is proving to be a challenging behavior that makes it difficult to cleanly generate this data. As a modification to the transport of water molecules to the crack tip is currently hypothesized to be causing this behavior, a study on the modification of the transport distance might be able to limit or even eliminate this behavior. Additionally, since the rougher SBC morphology is believed to play a critical role in the TTR event, a study on an alloy that experiences more severe SBC morphology could provide insights into the TTR behavior. To this end, 2199 has a far rougher SBC morphology and a study into the behavior of this alloy in low water vapor pressure, low temperature environments should serve as a useful comparison to the large quantity of work that has previously been performed on 7075.

Finally, after fatigue behavior curves have been generated, applying these growth rates to fatigue life estimates allows for the impact of these environments to be determined. Literature has clearly established the strong beneficial impact of high-altitude environments on the da/dN vs. ΔK behavior in 7xxx-Al alloys. Quantitative evaluation of the effect of these environments on the fatigue life and subsequent inspection intervals that are relevant to the structural integrity community has not been performed.

This dissertation will further explore the effect of high-altitude environment with a particular focus given to the role low water vapor pressure plays in the fatigue behavior of aerospace aluminum alloys. To this end, four tasks will be explored: (1) Efficacy of P_{H2O}/f as an exposure parameter to describe the environment. (2) Effect of limiting sample thickness to eliminate irregular crack front behavior at certain ΔKs and pressures. (3) Extension of high-altitude behavior in AA 7075 to 2xxx series aluminum alloys. (4) Incorporation of high altitude FCGR data into LEFM based models to determine the magnitude of fatigue life extension. A brief overview with each task is given below with a deeper discussion at the start of each dissertation chapter detailing the background for each project.

- *Task 1: P_{H2O}/f verification as an exposure parameter.*

As previously discussed, models developed by Wei, proposed P_{H2O}/f as an exposure parameter to describe the impact of most gas environments on fatigue. While some work has been performed to verify this parameter, a systematic study in the near-threshold has not been performed yet. **Question: Does P_{H2O}/f work across a wide range of pressures as an exposure parameter in the near threshold crack growth regime?**

- *Task 2: Effect of specimen thickness.*

Prior work demonstrated that at certain pressures and ΔKs a false threshold would occur where the growth rates would rapidly decrease before increasing at a lower ΔK, termed the threshold transition region (TTR). Additional testing showed that an irregular crack front was forming where cracking occurred faster on the edges compared to the center of the specimen when a rough crack wake was present. It was hypothesized that limited water vapor transport was decreasing the effective water vapor pressure at the center of the sample. Since this behavior is governed by water transport, it is possible that a change in sample geometry could modify the transport dimensions and enable a testing protocol to preclude the TTR. **Question: By limiting sample thickness is it possible to mitigate TTR behavior by decreasing the transport distance?**

- *Task 3: Extension of high-altitude environment to 2xxx series aluminum alloys*

The TTR behavior was shown to occur in AA 7075, when slip band cracking (SBC) is present. 2xxx series aluminum alloys have a rougher SBC which could result in a modified TTR behavior. **Question: The TTR has been shown to occur in AA 7075, but will the behavior be modified in a material with a rougher SBC morphology?**

- Task 4: High-altitude environment FCGR effect on fatigue life predictions.

The current generation of LEFM utilizes FCGR data generated in lab air. These growth rates have been shown to have significantly faster crack kinetics than growth generated in low water vapor pressure environments. These result in overconservative life and repair estimates which increase inspection burden and plan downtime for maintenance. **Question: Will LEFM fatigue life predictions substantially change if high-altitude FCGR data are incorporated into damage tolerant models?**

Answering these questions will provide meaningful insight into the high-altitude fatigue of aluminum alloys. These questions will be discussed and explored in more detail in each chapter of the thesis.

Chapter 2 – Verification of P_{H2O}/f as an Environmental Exposure Parameter

2.1 Introduction

2.1.1 Literature Overview

It is necessary to establish an environmental exposure proxy to properly compare growth rate behavior for different moist air environments. However, it has been shown that water vapor pressure alone is not capable of fully describing the environment at low water vapor pressure.[13,15,16,31,36,55,56] Wei has proposed P_{H2O}/f as an exposure parameter to describe the environment. This parameter not only takes into account the quantity of water available for the reaction, but the frequency in the denominator which results in a parameter that is dependent on the available time of reaction as well.

Abelkis et al., found that lower frequencies did indeed crack faster in water vapor environments. However, the water vapor pressure was not controlled which makes a systematic study of exposure parameter impossible.[21] Bradshaw and Wheeler followed up this work, and while they did control the water vapor pressure, they did not compare identical exposure parameters. They graphed growth rate versus pressure for two different frequencies and did not directly compare the growth rates. Ro et al., studied the behavior of the exposure parameter by testing at a constant frequency and varying pressure, as well as at a constant pressure and varying frequency.[42] This was only done for one pressure (2 Pa) and one frequency (20 Hz), which does not fully evaluate the exposure parameter and its ability to describe the environment across a wide range of frequencies and pressures. The most comprehensive study on the veracity of the exposure parameter to describe the environment to date was performed by Ruiz and

Elices.[16,31] Ruiz held constant several exposure parameters as the pressure and frequency were both varied in a way to maintain the target exposure parameter. It was found that there was good agreement at low water vapor pressures. However, as the water vapor pressure increased, a region was found where growth rates were insensitive to frequency.[16] While the Ruiz results support the Wei hypothesis, they also indicate a possible issue with the exposure parameter. It is important to note that Ruiz and Elices measured growth rates in the Paris regime and did not report any growth rates in the near threshold regime. It is critical that the near threshold regime is studied, as it has been shown that environmental cracking is exacerbated at lower ΔKs.[57] Further study is needed to verify the exposure parameter is able to properly describe the environment at these low ΔK values.

2.1.2 Test Matrix

To verify P_{H2O}/f as an exposure parameter, a two-pronged approach will be applied. First, a full ΔK-shed (interchangeably referred to as K-shed) testing were performed where frequency and pressure are varied in specific intervals to hold either P_{H2O} or P_{H2O}/f constant between tests to determine which parameter is dominating crack growth behavior. The full K-shed testing matrix will be limited to testing at 20 Hz and 10 Hz. This limits the change in P_{H2O}/f to only a twofold increase when decreasing the frequency from 20 Hz to 10 HZ, a relatively small change when considering the changes in exposure parameter needed to impact the crack growth rate.

A second test matrix where larger changes in frequency are able to be investigated utilizes constant ΔK testing, where again pressure and frequency are varied in a specific fashion in order to maintain constant exposure parameters across different combinations of P_{H2O} and frequency. In order to describe the behavior across all three regions of the exposure curve, these water vapor pressures will vary across each region. These experiments are able to vary the frequency from 1-30 Hz as each test takes significantly less time compared to full K-shed testing. A ΔK of 6 MPa√m will be applied, as this avoids the TTR region and any complication that might occur, while still being at a lower ΔK, which has a greater dependence on environment.

2.2 Experimental

2.2.1 Material

Testing was performed on a 7075-T651 aluminum alloy. The iron and silicon content were purposefully increased to better model alloys typically used on older aircraft. The composition of the alloy is shown in Table 1. Compact Tension specimens with a nominal width of 50.8 mm and a thickness of 7.62 mm were machined with a notch depth of either 12.7 mm for the K-shed testing or 10.7 mm for constant ΔK testing.

Alloy (Wt%)	**Zn**	**Mg**	**Cu**	**Cr**	**Fe**	**Si**	**Al**
	5.60	2.5	1.6	0.23	0.4 max	0.4 max	Remainder

Table 1: Aluminum alloy 7075 composition (Wt %)

2.2.2 Loading Protocol

Fracture mechanics-based fatigue testing was guided by ASTM E647 using a computer-controlled servo-hydraulic machine to apply a sinusoidal waveform. The crack length was calculated via compliance measurements using a clip gauge at the crack mouth; [58] the challenges and applicability of this method for portions of the testing exhibiting an irregular crack front are detailed elsewhere.[28] Testing was performed at a constant stress ratio (R) of 0.5 and frequency (f) of 20 Hz using a K-shed protocol following the formula $\Delta K=\Delta K_o \exp[C(a-a_o)]$ with ΔK_o = 14.85 MPa√m, a_o=13.7 mm C=0.08 mm^{-1}.[13,58] This decreasing K test continued until da/dN was roughly $5x10^{-8}$ mm/cycle or ΔK reached 2 MPa√m. The effective ΔK is calculated post-test using adjusted compliance ration (ACR).

Constant ΔK testing was performed at a constant R ratio of 0.5 and a $\Delta K_{effective}$ of 6 MPa√m. Each segment will crack for between 1-2 mm, until a constant growth rate is achieved. Each segment was then graphed crack length versus cycles, and the slope of the linear section of this graph is used to determine the growth rate of each segment. In order to maintain a constant ΔK as the crack grows and crack closure increases, the ACR is measured after each segment, and the targeted ΔK is increased so the $\Delta K_{effective}$ is maintained. The testing matrix of the constant ΔK testing is shown in Table 2. This matrix isolates both the water vapor pressure and the exposure parameter, holding one of them constant for comparison for each experiment. Specific combinations of water vapor pressure and frequency were chosen in order to hold the exposure parameter constant across a range of different water vapor pressures (constant exposure parameters are color coded in Table 2). The exposures tested are shown on the exposure plot below in Figure 4, with the exposures tested marked with solid lines color coded to Table 2.

P_{H2O} (Pa)	Frequency (1/s)	P_{H2O}/f (Pa-s)
0.0675	20	0.003375
0.0675	10	0.00675
0.0675	5	0.0135
0.0675	1	0.0675
0.135	20	0.00675
0.135	10	0.0135
0.135	1	0.135
0.27	20	0.0135
0.27	8	0.03375
0.27	1	0.27
0.675	20	0.03375
0.675	10	0.0675
0.675	1	0.675
1.35	20	0.0675
1.35	10	0.135
1.35	1	1.35
2.03	30	0.0675
2.03	15	0.135
2.03	7.5	0.27
2.03	1	2.025
40.5	20	2.025
40.5	1	40.5
810	20	40.5
810	1	810
Lab air	20	N/A
Lab air	1	N/A

Table 2: Test matrix for constant ΔK testing. Colored exposure parameters are done to easily reference which tests have identical exposure parameters

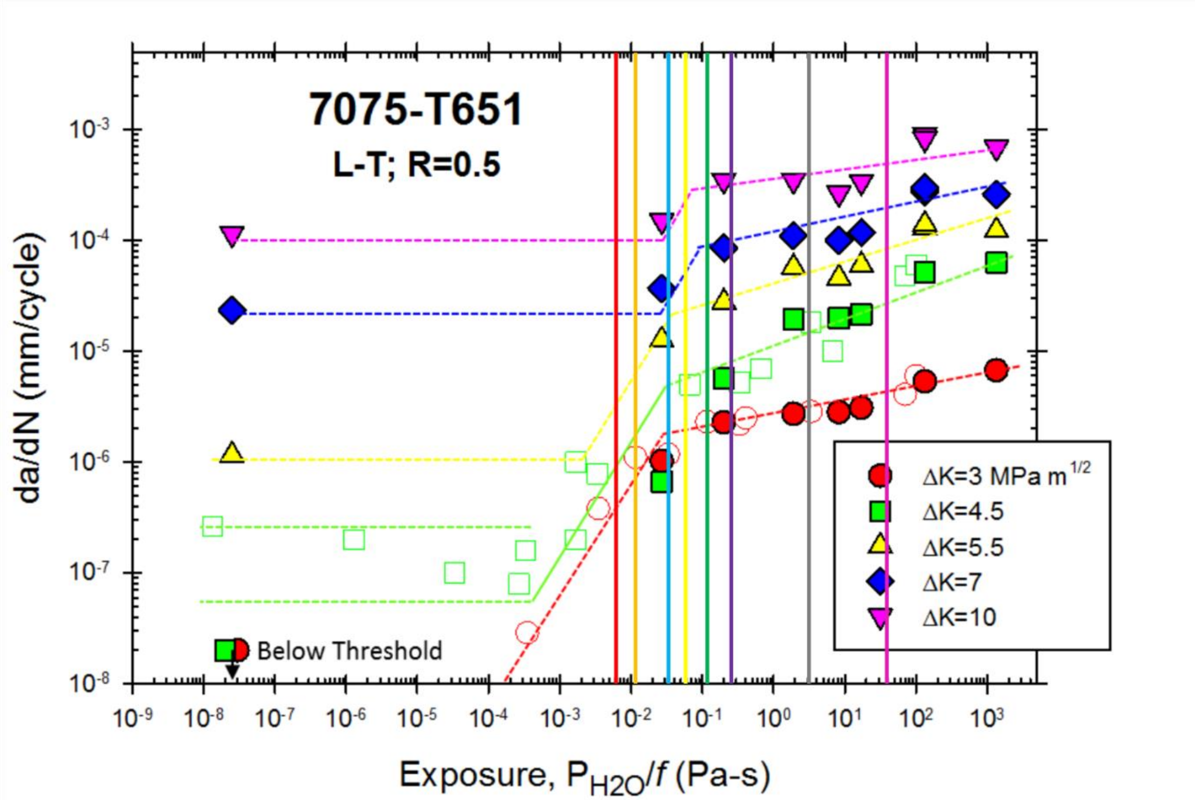

Figure 4: Room temperature growth rates of AA 7075 plotted versus exposure parameter, P_{H2O}/f, for several different constant ΔK at R = 0.5, f = 20 Hz[10] *Solid lines are fit to the data and reflect theoretically based models.*[40,53] *Vertical lines mark exposures tested at constant ΔK*

2.2.3 Environmental Control

The low water vapor environment was maintained within a Cu gasket sealed UHV chamber. For each case a multi-scale pumping procedure was used to achieve vacuum levels below 10^{-7} Pa. Subsequently high-purity, triple distilled water vapor was introduced to the chamber using a sealed glass flask with a leak valve.[13] The desired water vapor pressure was held constant throughout the test by balancing the flow of water and the degree of pumping on the chamber.

2.3 Results

2.3.1 ΔK-shed Loading Experiments

For the K-shed results, Figure 5 demonstrates that P_{H2O}/f is a useful exposure parameter, and generally, crack growth rates converge at the same exposure parameter, while they diverge at a constant water vapor pressure. Specifically, in Figure 5A, constant water vapor pressure at 1.8 Pa diverges between a ΔK of 4 to 6 MPa√m, and at 0.27 Pa, there is no spike in growth rates after the TTR at 20 Hz, as was seen at 10 Hz (Figure 5B). For constant P_{H2O}/f, there is excellent agreement, particularly in Figure 5C and Figure 5D. However, in Figure 5E, there is some divergence, again between a ΔK of 4-6 MPa√m.

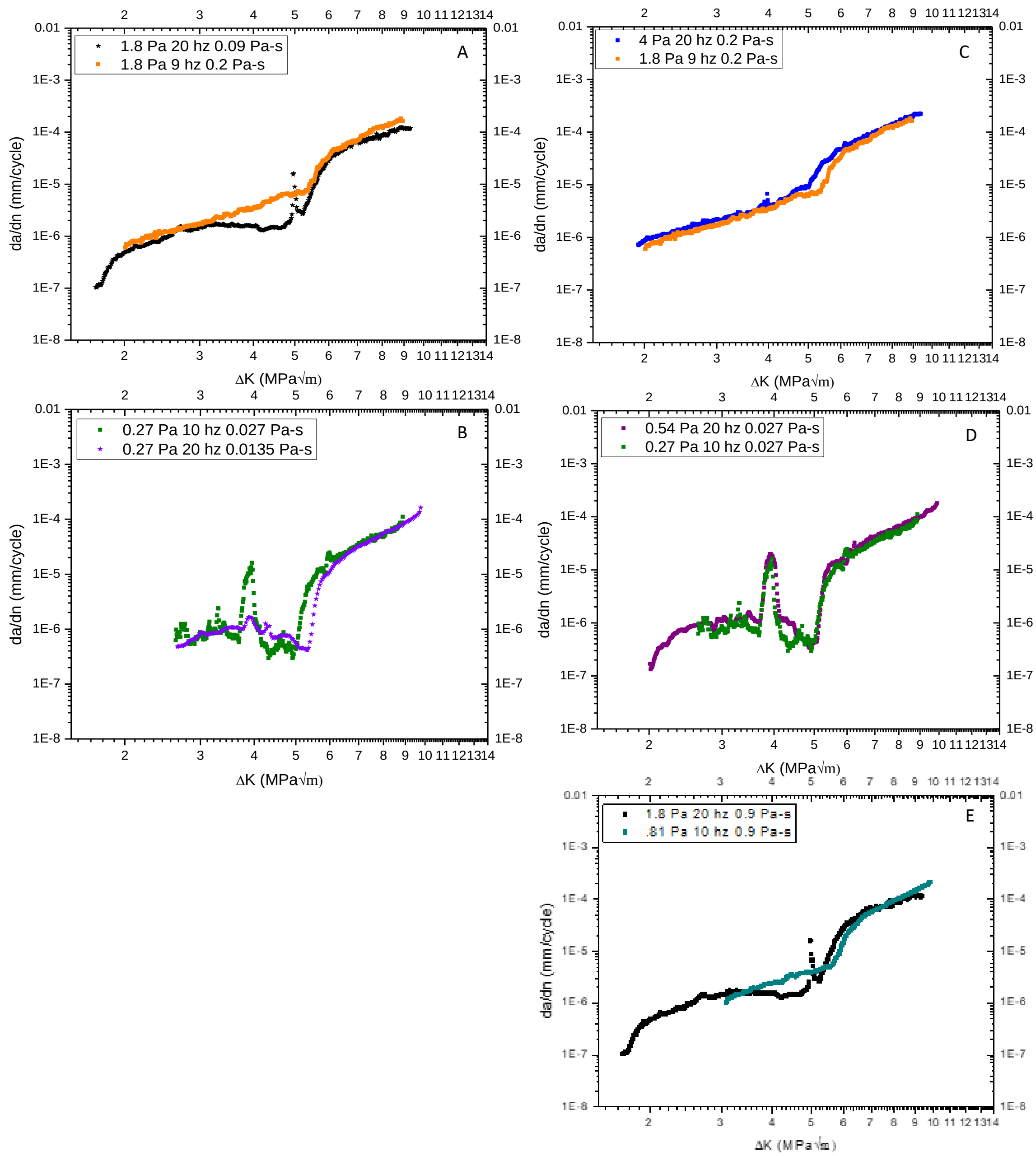

Figure 5: da/dN vs ΔK for the PH2O testing matrix. Each graph tests that either contain a constant exposure parameter (P_{H2O}/f) or constant water vapor pressure.

2.3.2 Constant ΔK Experiments

Constant ΔK testing results are shown in Figure 6 and Figure 7. There are two ways to determine which parameter is a better proxy for the environment. First, if the parameter listed in the legend is describing the environment, then each curve should have no slope. Alternatively, if the parameter listed on the X-axis is properly describing the environmental severity, then each position on the X-axis, regardless of the curve it is on, should coalesce to a single da/dN value.

Figure 6 shows the behavior of constant water vapor pressure as the exposure parameter changes. (Note: since each curve on the graph is at a single pressure, the exposure parameter is linked to and inversely proportional to the testing frequency). If the water vapor pressure properly describes the environment, then the slope of each constant water vapor pressure curve should be near zero. At 2.03 Pa and below, the curves are closely bunched together, and show a small dependence on exposure parameter (and therefore, frequency as well) before 40.5 Pa. Growth rates at 40.5 Pa and 810 Pa were significantly higher. Of note, 810 Pa has almost no slope.

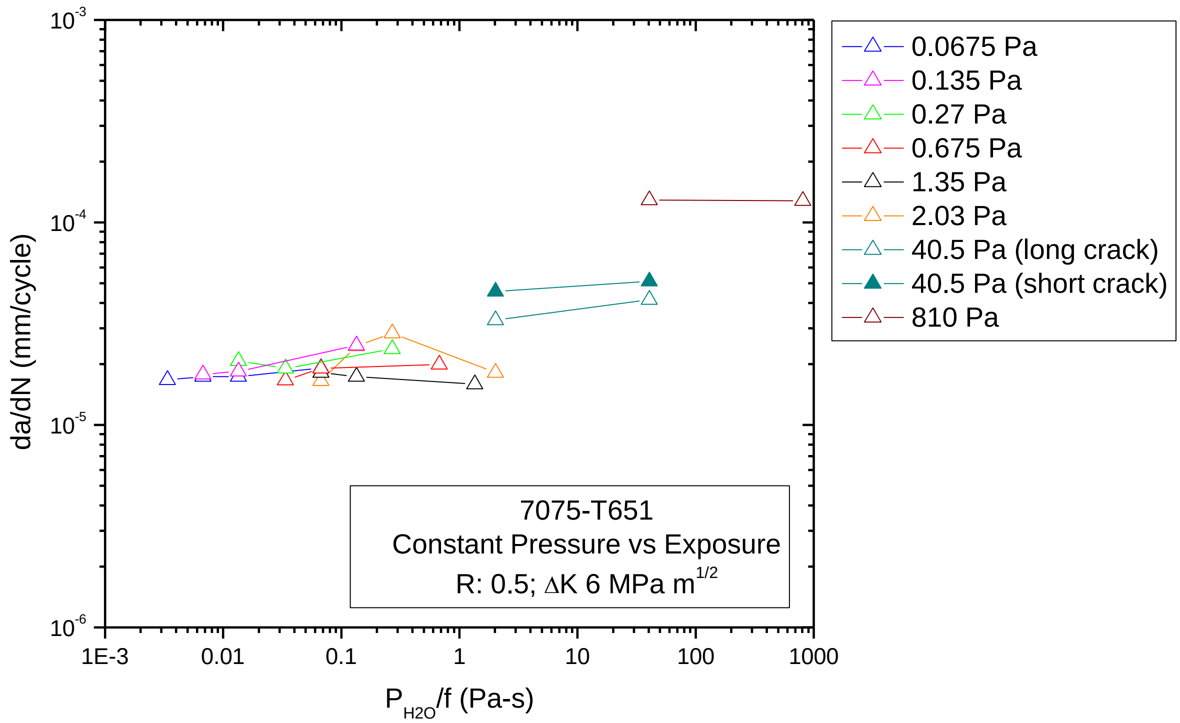

Figure 6: Constant Δk of 6 MPa√m at several constant water vapor pressure growth rates versus exposure parameter. 40.5 Pa had two tests, one with a crack length of 32-35 mm (long) and one at 15-18 mm (long)

Figure 7 describes how growth rates of a single exposure parameter vary as the water vapor pressure changes (which again is tied to the changes in frequency). If the exposure parameter is the proper environmental parameter, the slope should be zero. Until 2.03 Pa-s, the curves have mostly no slope, and then at higher exposure parameters, there is a steep increase in growth rates as pressure (and frequency) increase.

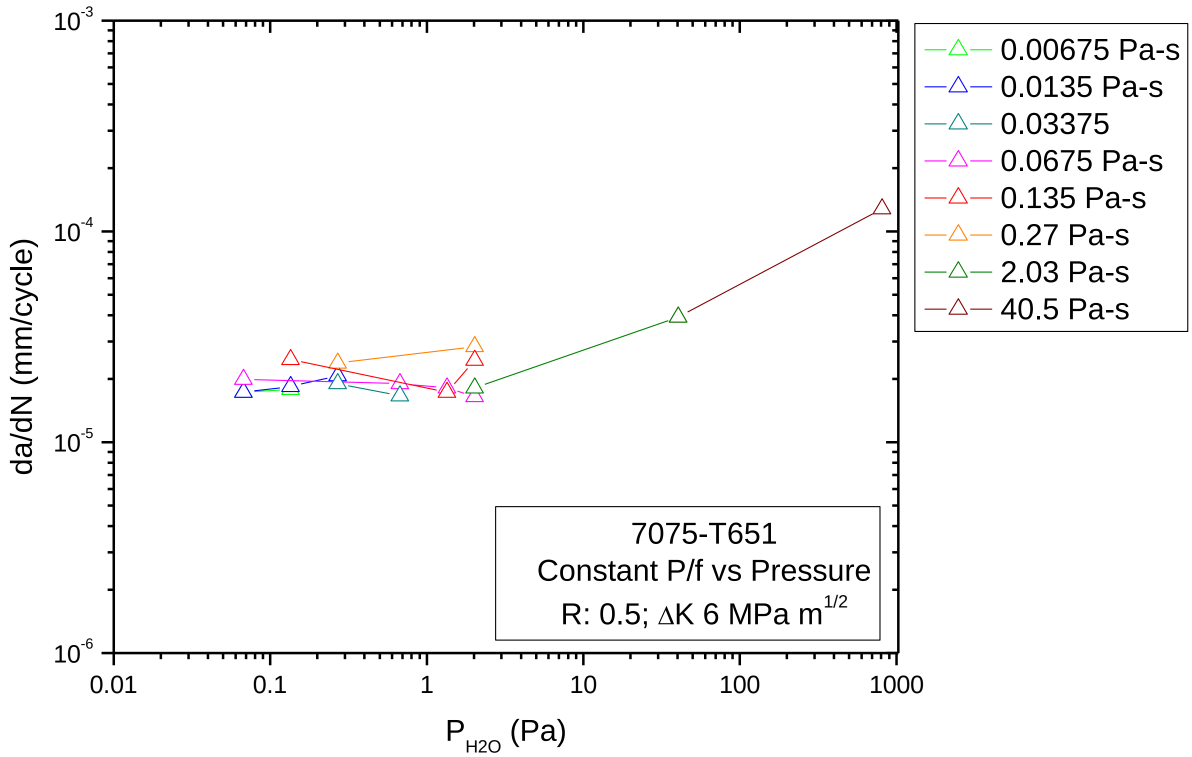

Figure 7: Constant ΔK of 6 MPa√m at several constant exposure parameters growth rates versus water vapor pressure

2.4 Discussion

2.4.1 Exposure Parameter Describing K-shed Data

The K-shed experiments show a remarkable agreement with the constant exposure parameter tests, particularly when looking at Figure 5C and Figure 5D, where there is minimal to zero divergence of the two curves. There is some divergence in Figure 5E, between ΔK of 6 and 4

MPa√m, though the difference between the curves is roughly half as small as the one between the curves in Figure 5A. The constant water vapor graphs do show agreement for the majority of the curves, but diverge from each other from a ΔK of 6 MPa√m until roughly 4 MPa√m.

It is interesting that this divergence, indicating water vapor pressure alone is not properly describing the environment, only occurs between ΔK 6 and 4 MPa√m, as this is exactly the ΔK region where the TTR is observed. The TTR behavior is kicked off by a transition to slip-band cracking which is extremely sensitive to the applied ΔK and environment.[59] This transition is highly dependent on having the correct environmental parameter, which would suggest that water vapor pressure is not accurately describing the environment throughout the test, however, outside of this region, the discrepancy is small enough that no effect on crack growth rate is observed.

For the K-shed testing, the exposure parameter does a better job at describing the environmental cracking behavior of 7075. However, the limited range of ΔKs where the exposure parameter outperforms water vapor pressure is surprising.

2.4.2 Exposure Parameter Describing Constant ΔK Data

Analyzing the constant ΔK testing provides some interesting insights into the environmental cracking behavior of AA 7075 in low water vapor pressure environments. It is important to first define what either water vapor pressure or the exposure parameter controlling the environment would look like. If the variable is successfully describing the environment, the growth rates of different tests should remain constant as the frequency of loading is changed at either a constant water vapor pressure or a constant exposure parameter. A curve with no slope would indicate that the parameter in the legend for the figure is successfully describing the environment.

The exposure vs water vapor pressure graph (Figure 7), shows that in certain regions the exposure parameter does not fully describe the environmental severity. At higher water vapor pressures, the curves show a dependence of da/dN on the frequency. The average slopes of the constant exposure curves are roughly five times steeper than the constant water vapor pressure curves in this same region. However, a more careful analysis uncovers two regions, one better described by the exposure parameter, and one better described by water vapor pressure.

In order to tease out this dependence, the absolute value of the slope of the growth rate vs. frequency curve for both constant P_{H2O}/f and constant water vapor pressure is calculated. Again, there should be no dependence on frequency if the parameter is properly describing the environment. Additionally, the standard deviation of da/dN at each P_{H20}/f and water vapor content was also calculated, with lower standard deviations corresponding with a better proxy for the environmental severity. Shown in Table 3, at low to intermediate water content, (blue shading) the exposure parameter does a better job of describing the environment, while at high water content, (orange shading) water vapor pressure more accurately describes the environment. Critically, in this high-water content region, the exposure parameter does not describe the environmental severity as there is a strong dependence on frequency, as well as a high standard deviation in this region. This is contrasted by constant water vapor pressure having a near zero slope in this region. This indicates that at this higher water vapor content, any time dependent processes that were limiting environmental cracking are no longer the rate limiting step and water content alone determines the environmental damage. This behavior had been observed previously in literature in 95% relative humidity environmental testing where tests were performed at 2 Hz and 20 Hz and no change in crack growth rate was observed for both 7075 and 2199.[10,13,27,60]

It is both a critical and unexpected result that in one region, water vapor pressure is a better proxy for environment, and in the other, the exposure parameter describes the environmental severity.

Constant Water Vapor Pressure			Constant Exposure Parameter		
Water Vapor Pressure	Avg |slope|*10^8	Avg StdDev*10^6	P_{H20}/f	Avg |slope|*10^8	Avg StdDev*10^6
<810 Pa	26.9 (mm*sec/cycle)	3.17	**<0.27 Pa-s**	13.8 (mm*sec/cycle)	1.89
≥810 Pa	5.26 (mm*sec/cycle)	0.71	**≥0.27 Pa-s**	217 (mm*sec/cycle)	27.01

Table 3: The average absolute value of the slope of da/dN vs frequency graph of each of the constant water pressure (left side) and constant exposure curves (right side), as well as the average standard deviation of da/dN at each constant water vapor pressure or constant exposure parameter These where then divided into two regions for each graph, low water content (blue shading), and high-water content (orange shading). The slope was multiplied by 10^8 and the standard deviation by 10^6 to ease in understanding

2.4.3 Exposure Parameter Versus Water Vapor Pressure

The water content dependent region indicates that only in certain regions is the exposure parameter an appropriate metric to describe the environment. This result, combined with the limited stress intensity range that the exposure parameter outperforms constant water vapor pressure, shown in the K-shed testing results, indicates that the exposure parameter is only useful in a specific range of water content and stress intensity. This is a critical finding as it indicates that while the exposure parameter is used universally in literature, a careful consideration of the testing parameters is needed to ensure that either exposure parameter or water vapor pressure is the appropriate parameter. Additionally, it is surprising how well water vapor pressure performed in the K-shed testing, and even in the intermediate region of the constant ΔK testing, water vapor pressure performed better than expected. While the constant ΔK testing allows for a wide range of environments to be tested, particularly at low frequencies, it has its limitations on understanding the effect of ΔK on the behavior. Further testing at a ΔK of 3 MPa√m or lower would be beneficial to study the behavior at ΔKs closer to threshold.

The findings concerning the regions where exposure or water vapor pressure are governing are an important observation, as ensuring a consistent, comparable environmental severity parameter is critical in order to compare results from laboratory to in-service conditions. It is important however to contextualize these findings with respect to their applicability to other aluminum alloys. While similar results were seen in 7017, the specific pressures where the environmental parameter transitions from exposure controlled to water vapor pressure controlled varies between the two alloys.[16,31] While there was no ΔK dependance on when exposure parameter was required to describe the environment in 7017, the lowest tested ΔK was 7 MPa√m, and it is possible that if the K-shed was continued, a stress intensity dependance would be observed. It is likely that in other aluminum alloys, a similar behavior would be observed with a general trend of the exposure parameter being a proxy for the environment at low water content and at higher water content, water vapor pressure being the parameter of choice, the specific transition pressures will vary.

2.4.4 Impact on Process Zone H Diffusion Limited Hypothesis

It has been suggested by Gasem and Gangloff that diffusion of H in the process zone is the limiting factor at some water vapor pressures for 7xxx aluminum alloys [53]. In an aqueous

NaCl environment, it was seen that as the frequency decreased, the growth rate would increase until an f_{crit} was reached, where further decreases in frequency did not affect the crack growth rate. It is believed that at these lower frequencies, the H is able to fully transport to the process zone, and more time between cycles does not result in a higher H concentration. Recall, at higher water vapor pressures, a transition occurs where changes in frequency do not affect the FCGR. This would suggest that at these higher pressures, if the hydrogen diffusion limited mechanism was previously governing the crack growth behavior, it is no longer the rate-limiting mechanism.

A thought experiment to explore what mechanism is controlling the different regions can help explore this phenomenon. It has been established that in an H assisted environmental cracking, the fracture stress required for crack extension is a function of the H concentration at a distance x away from the crack tip.[61] This stress will vary as the distance from the crack tip increases until it reaches a maximum stress at a critical distance, da^*, from the crack tip which represents the maximum crack extension.[53] Critically though, the H concentration will decrease as the distance from the crack tip increases. The concentration of H, C_H, will depend on the frequency, as the more time that is available, the more H will be able to diffuse into the process zone, assuming the diffusivity is constant. This can be visualized in Figure 8. (Note: all curves shown in Figure 8 are not based on physical parameters and are simply drawn to demonstrate the hypothesis and provide a visual representation.) The concentration of H and the max stress is graphed versus X, the distance from the crack tip. From experimental results, there appear to be two regions, one where growth rates are dependent on frequency, and one where they are independent of frequency. Gao proposed that there was some C_H where the process zone would become saturated, and further increases in hydrogen concentration would not increase the crack growth rate.[29] This value, C_H^*, is shown in Figure 8 (in actuality this value would vary with X but for ease of understanding it is shown as a constant). In the low content region where growth rates depend on frequency, it can be seen that at high frequencies, less time is given for H diffusion to occur, and the C_H is lower than at low frequencies. This results in a smaller growth increment, da, for these high frequencies. As the water vapor pressure is increased, the C_H is high enough that for all three frequencies the C_H^* is exceeded, resulting in the same growth rate for all three frequencies.

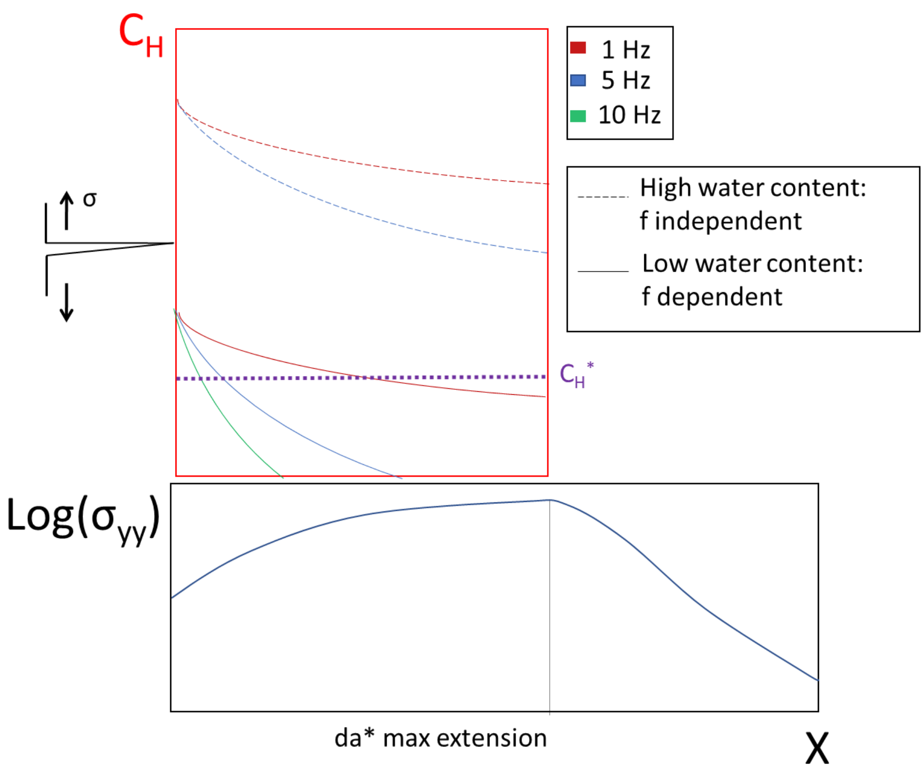

Figure 8: The concentration of H, C_H is shown as a function X, distance from the crack tip. This is done for three different frequencies and for low-water content (dependent on frequency) and high-water content (independent of frequency). Below the max stress is graphed versus X as well. The critical concentration of H for crack extension to occur, C_H^*, is shown (purple line) as a flat line to ease understanding, but this will actually vary as the max stress also varies.

The saturation hypothesis explains the transition from frequency dependent growth rates at low water vapor pressure, to growth rates independent of frequency at high water content. However, this hypothesis does not satisfy another finding that was seen in the experimental results. Recall that after the transition to a water vapor-controlled environment (frequency independent), from 40.5 Pa to 810 Pa, the growth rates increased substantially. This situation is shown in Figure 9. As the water vapor pressure is further increased, the C_H at the crack tip will also increase. This will lead to a high concentration in the process zone, but as both water contents are above C_H^*, the growth rates should not change according to Gao's hypothesis. This does not correspond with the experimental results where large increases in growth rate were observed, indicating that a saturation concentration has not yet been reached.

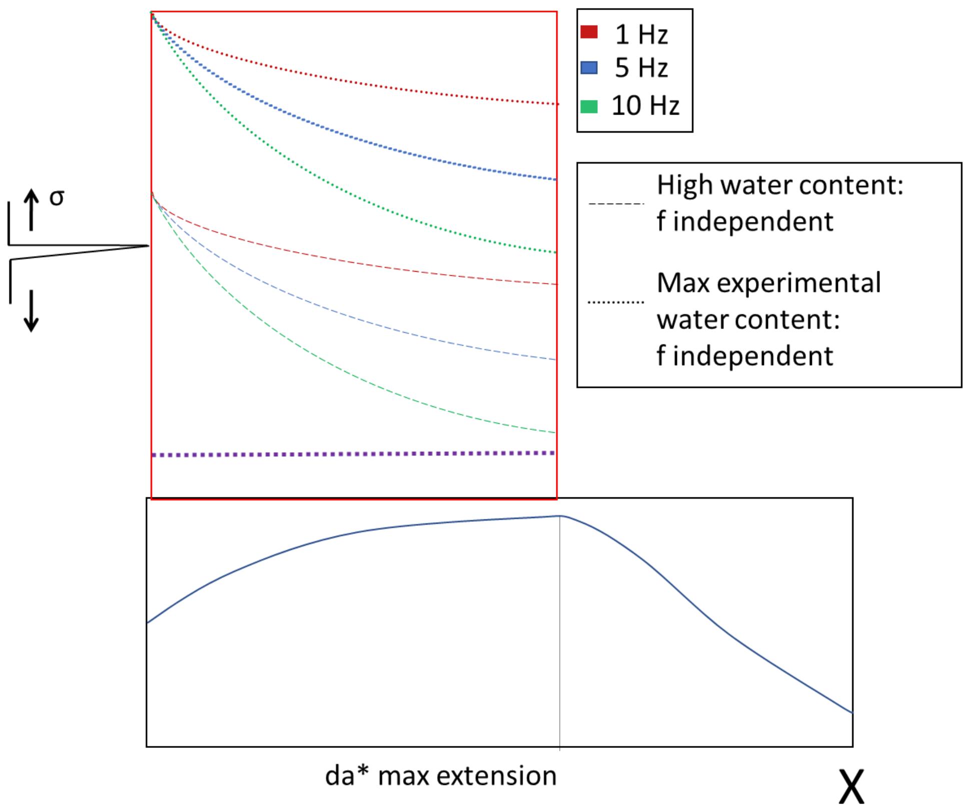

Figure 9: The concentration of H, C_H is shown as a function X, distance from the crack tip. This is done for three different frequencies and for high-water content and max experimental-water content. Below the max stress is graphed versus X as well. The critical concentration of H for crack extension to occur, C_H^*, is shown (purple line) as a flat line to ease understanding, but this will actually vary as the max stress also varies.

This suggests that while there is clearly a transition from frequency dependence consistent with the H diffusion limited model proposed by Gasem, there is another region where growth rates are not diffusion limited, and a saturation concentration of H does not occur. The determination of the mechanism behind this behavior is outside the scope of this study. However, this finding suggests a new direction of study for future projects.

2.4.5 Implication on Applying an Environmental Parameter in LEFM Models

While the impact of these results on the mechanistic understanding are important, ultimately applying what was learned into future LEFM damage-tolerant fatigue life models is a critical result. As discussed previously, there are two regions, one at high water content (≥0.27 Pa-s), where water vapor pressure best describes the environmental severity, and a second at low water content (<0.27 Pa-s) where the exposure parameter is a good proxy for environmental severity. A similar finding was found by Ruiz and Elices for AA 7017, with the transition point occurring at 10 Pa-s.[31] When applying FCGR generated in low water vapor pressure environments to fatigue life models, it is critical that the correct environmental parameter is applied. To this end, two things need to be determined: 1.) what process should be followed for generating data for an alloy that has no previous data in a low water vapor pressure environment? 2.) How should these data be applied fatigue life modeling for in-service components?

First, before full K-shed or K-rise data are generated to provide a range a series of constant ΔK testing at roughly 5 MPa√m (though exact stress intensities might change based on alloy cracking behavior) These constant ΔK tests should be performed a series at 0.27 Pa and incrementally increase the pressure. This will continue until a transition where the 20 Hz and 1 Hz test have identical growth rates. This marks the transition from P_{H2O}/f controlled to water vapor pressure controlled. As can be seen from the work in this dissertation and the work by Ruiz on 7017, the transition point will change from alloy to alloy and needs to be determined for each alloy. Once this transition point is found, a series of either K-shed or K-rise testing can be performed across a range of relevant water pressures and ΔKs. This data can be generated at any frequency with a preference for high frequencies as the time for each test will be limited. Depending on how these growth rates will be applied in LEFM fatigue life models, it is possible that the determination of the transition point can be skipped as will be detailed below.

Once the data is generated, applying the data correctly to the fatigue life models can be complex. Utilizing the correct environmental parameter (P_{H2O} or P_{H2O}/f) is critical for correctly applying high altitude data to fatigue life estimates. There are two approaches to determining the correct parameter that could be used, one being more accurate while the other approach is less rigorous but requires fewer inputs.

Types of load	Cycle Frequencies (Hz)
Ground-air-ground	0.00003-0.001
Cabin Pressurization	0.00003-0.0005
Maneuvers	0.005-0.2
Gusts	0.1-10
Taxiing	0.5-20
Buffeting	10-100
Acoustic	100-1000

Table 4: Aircraft fatigue load cycle frequencies[62]

For both approaches, it is critical that the frequency of loading for the applied loads is determined. Examining the frequency of loading that aircraft undergo in-service is required in order to properly understand what region each load occurs at. In Table 4**Error! Reference source not found.**, it can be seen that the frequency of loading varies widely. Utilizing the less rigorous approach, the parameter can be determined by a very simple test. If the frequency of loading is greater than 1 than P_{H2O} will be utilized, while if the frequency is less than 1 then P_{H2O}/f will be applied. This ensures conservatism as the parameter that describes the more aggressive environment will be applied so no matter which parameter is actually controlling the cracking behavior, the in-service growth rate will not exceed the modelled growth rate. Critically, this methodology does not require a transition point from P_{H2O} to P_{H2O}/f be found.

While this method is simple to apply it runs into issues, particularly at very low frequencies (such as cabin pressurization loads). At these low frequencies, the P_{H2O}/f value will be extremely high and as the results in this dissertation have shown, this is exactly with P_{H2O}/f is no longer describing the environment. This will result in an overconservative approach where the environment in the models will be far more aggressive than it is in actuality. While this methodology is simple to apply and conservative, a more rigorous approach can solve this issue.

The more rigorous approach will require that the transition point from P_{H2O} controlled to P_{H2O}/f controlled be found as was described previously. Once this is determined and the water vapor pressure and frequency of the load is known, the appropriate parameter can be applied based on what if the conditions of loading are above or below the transition point. This process ensures that the appropriate environment be applied in all loading conditions. While this methodology does require determining the transition point it ensures a more accurate environmental description. This process will ensure that for all loading environments, a conservative environment is maintained, while still allowing for slower FCGR be applied where appropriate. The transition point will need to be experimentally determined for each alloy. However, this process is straightforward and does not require a large amount of experimental work.

Finally, it is possible to combine aspects of each of these processes to better deal with the low frequency loading without requiring that the transition point be experimentally determined. At high to moderately low frequencies the less rigorous process will be utilized where the transition from using P_{H2O} to P_{H2O}/f is done at 1 Hz. Then at very low frequencies where P_{H2O}/f is very high for loads such as cabin pressurization, P_{H2O} will be used instead of P_{H2O}/f. At these low frequencies, it is certainly past the transition point so P_{H2O} can be safely used even though the transition point has not been determined. This eliminates the main drawback from the simplistic environment determination process without requiring additional experimental work be performed. Ultimately, the exact needs will vary for various applications and it might be required that a more rigorous process is required, but combining the two methodologies provides the best combination of limiting experimental work while still ensuring that an accurate environment is applied for most scenarios.

2.5 Conclusions

While researchers had previously studied the role of the exposure parameter in describing the environment, this is the first study to comprehensively study the exposure parameter across a wide range of water vapor pressures, as well as utilize both K-shed and constant ΔK loading. Several critical findings on the limitations of using the exposure parameter were found.

- K-shed testing showed that exposure parameter performed better than water vapor pressure at describing the environmental cracking of 7075. Constant water vapor curves diverged between ΔKs of 4 to 6 MPa√m, which is within the transport limitation regime.[13] Outside of this regime, water vapor curves converged, and either water vapor pressure or exposure are able to describe the environment.
- Constant K-hold testing revealed two regions, one where water vapor pressure describes the environment, and another where exposure is controlling. At low to intermediate

water content, the environment is controlled by exposure, before transitioning to a water vapor-controlled environment.

- A region was found where crack growth does not depend on frequency. Additional analysis demonstrated that this region had not yet reached the saturation point for H concentration and suggested a different mechanism is responsible for crack growth behavior.
- A process for applying the appropriate parameter to in-service fatigue life predictions was proposed.

These results show that while exposure parameter is widely used in literature, and it is currently the best singular parameter to describe the environment, it is important that its limitations are understood.

Chapter 3: Investigation into the Factors Effecting the Threshold Transition Regime

Note: This project shared many aspects with Adam Thompson, another PhD candidate who recently graduated. In order to help with clarifying contribution for the sake of the committee, an explanation of contribution is given. The K-shed testing of thick, medium, and thin samples was performed in tandem with Adam Thompson with both of us performing a roughly equal amount of work on the testing and optical microscopy. More complicated microscopy was performed solely by Adam Thompson. Near the end of these tests, the author switched projects to a corrosion-based aluminum alloys project and work on the TTR behavior was continued by Adam Thompson. This included the K-rise testing and analysis as well as a proposed hypothesis explaining the behavior developed by Adam Thompson. Following returning to this project a collaboration was started with Dr. Hochhalter at the University of Utah. The author helped design experimental approach and boundary conditions for modeling of crack tip driving force performed at University of Utah, as well as analysis of the results.

3.1 Introduction

In order to address the effect of changes in the molecular transport path on the extent of similitude, it is necessary to review the pertinent aspects of the HEE process. As stated previously, the crack tip P_{H2O} governs the available reactant for the surface reaction to produce atomic H that can adsorb on the crack tip surfaces and then absorb and diffuse to set the internal H concentration. The local H concentrates due to hydrostatic stress in the crack tip process zone and interacts with the local stress/strain field to result in the environmental contribution to the da/dN response.[43,47] At conditions relevant to airframe operational environments and where the HEE process is governed by molecular transport, changes in the molecular transport distances and crack wake roughness can drastically impact the crack tip P_{H2O} despite fixed bulk P_{H2O}/f, stress-ratio (R), and ΔK_{eff} [5,28].

The change in crack growth response due to modifications in the flow path is highly important to the generation of environmental crack growth data for use in LEFM based modeling for two reasons. First, there will likely be differences in transport path geometry between a laboratory specimen and a crack in an operational component (e.g., CT sample versus a thumbnail crack). Second, there is a transition from flat-transgranular cracking to tortuous slip-band cracking (SBC) in the low-to-intermediate P_{H2O}/f and ΔK regimes in 7075-T651.[28,54] The micromechanical and metallurgical mechanisms governing the transition to SBC in 7075-T651 are not fully understood, but the resulting increase in roughness has been shown to drastically impact the crack growth kinetics in a systematic manner[28]. Since the SBC behavior happens in a limited range of P_{H2O}/f and ΔK values, this gives rise to a loading history effect on the resulting environment-specific da/dN vs. ΔK relationship.

This is problematic as linear elastic fracture mechanics models (LEFM) use these growth rates as inputs into fatigue life models according to similitude. These inputs into software such as AFGROW require that cracking behavior at a constant ΔK and environment have a constant crack growth rate. This is not happening in the TTR region as crack growth history effects cracking at these low to intermediate ΔK values. It is clear that at lower ΔK values, the crack growth rate should not increase as the ΔK decreases; this loss of similitude has been shown to be due to loading history effects. In order to apply FCGR at low water vapor pressure to the next generation fatigue life models they must represent the intrinsic behavior of the material and not be an artifact of the testing protocol. While prior work proposed an interpolation approach can be conservatively applied to preclude inclusion of the TTR in LEFM predictions, the root cause of this behavior and mitigation strategies still warrant investigation.

The TTR is believed to occur due to a higher environmental contribution on the sides of the sample due to the roughness limiting transport down the mouth of the crack. It might be possible to eliminate or at least mitigate this behavior by limiting sample thickness and therefore, transport distance. To test this, a series of experiments will be performed where the sample thickness is varied. This will allow insight into how changes in transport distance impact the crack behavior at intermediate ΔKs where the TTR is present.

3.2 Experimental

The material, the K-shed loading protocol, and environmental control is largely the same as was detailed in the experimental section of Chapter 2 of this thesis, with some changes to variables. ΔK_o was 10 MPa√m and testing was stopped when growth rate reached 1.0 x 10^{-7} mm/cycle, the R^2 of the linear fit of the compliance fell below 0.8, or a ΔK of 2 MPa√m was reached. Samples of three different net thicknesses were machined. "Thick" specimens had B = 7.62 mm with no side groove. "Medium" came in two configurations, one where the sample was side grooved and the B was 7.62 mm and the B_{net} was 5.74 mm, or simply machined so that both B and B_{net} were 5.74 mm. Finally, the "thin" specimens had a B = 5.74 and were side grooved and B_{net} = 4.92 mm. Testing environment ranged from an inert environment (UHV) to intermediate pressures where the TTR was expected to occur, as well as higher water vapor pressures where the TTR was not expected to occur.

3.3 Results

K-shed testing was performed on samples with three different net thicknesses. This was done first in UHV environment to ensure that changing specimen thickness had no effect on the intrinsic mechanical response and any effects observed in water environments are due to an environmental response. As can be seen in Figure 10, there is no impact of sample thickness on the mechanical response of 7075 in a UHV environment. The optical fractography of the samples show similar behavior as well with initially a smooth, flat transgranular damage mechanism at high ΔKs, followed by a transition to a rough slip band cracking (SBC) mechanism at a ΔK of roughly 5.6 MPa√m. The edges of the thick specimen do transition at a smaller crack length than the middle, while the opposite is observed for the medium and thin specimens which were side grooved.

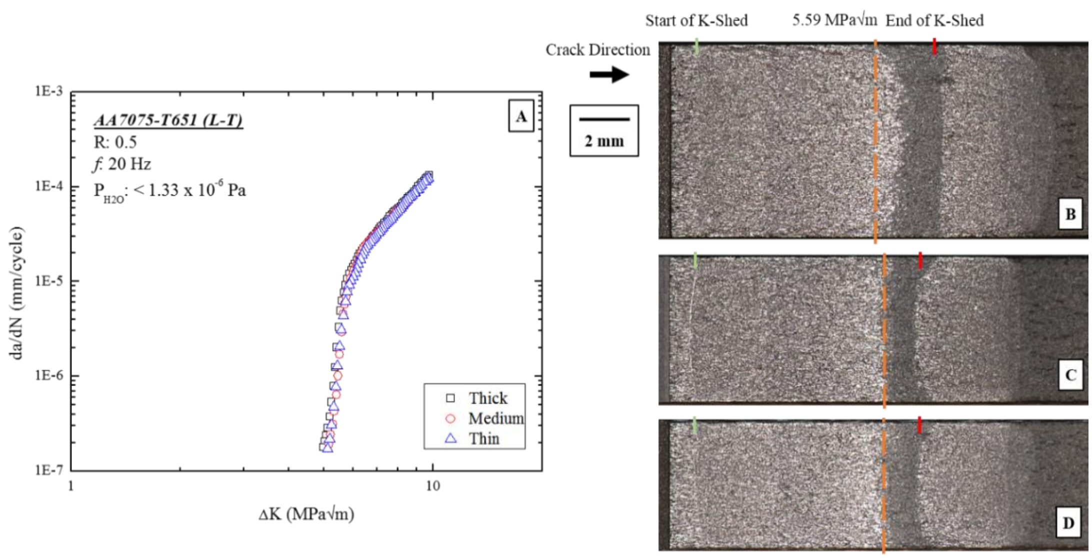

Figure 10: da/dN versus ΔK relationship (A) for thick medium and thin specimens in an UHV environment. Optical fractography of the thick, medium, and thin specimens are shown in B, C, and D. Orange lines marks onset of SBC. (Image created by Adam Thompson)

This methodology was repeated with increasing water vapor pressure at 0.0675 Pa and 0.54 Pa are shown in Figure 11 and Figure 12 respectively. All three thicknesses again showed nearly identical behavior and displayed the TTR behavior. Initially growth rates converged with UHV da/dN data, before spiking and reaching a new local maximum before decreasing again to threshold. This behavior is much more pronounced at 0.675 Pa, while 0.54 Pa has a more muted TTR behavior. Optical images at 0.675 Pa show again initially transgranular cracking before transitioning to SBC (orange line) across the entire sample. Further transgranular cracking then proceeds along the edges of the sample while the center of the specimen cracks more slowly and exhibits a rougher SBC mechanism. The faster rates at the surface and slow rates at the center result in an irregular crack front. As the severity of the crack front irregularity increases, eventually there is a transition to a distinct rough fracture surface morphology, that suggests a rapid crack advance. This corresponds with the local maximum seen in da/dN curve. After the rapid crack advance, the center transitions back to a rough, SBC morphology which continues for most of test before fully transitioning to transgranular across the width of the sample. A similar but distinct behavior was observed at 0.54 Pa. The initial behavior was identical but the transition occurred at a higher ΔK, and the thickness of the SBC region is smaller and the gradual ingress of transgranular cracking from the sides less pronounced. Additionally, there is no indication of the rapid crack extension morphology present, however there is a divot, reminiscent of a ball and cup ductile failure, present in the sample. This divot is off centered for all three specimens and much longer in length in the thick specimen. After the divot, there is no transition back to SBC morphology as was seen at 0.0675 Pa after a ductile failure morphology was present.

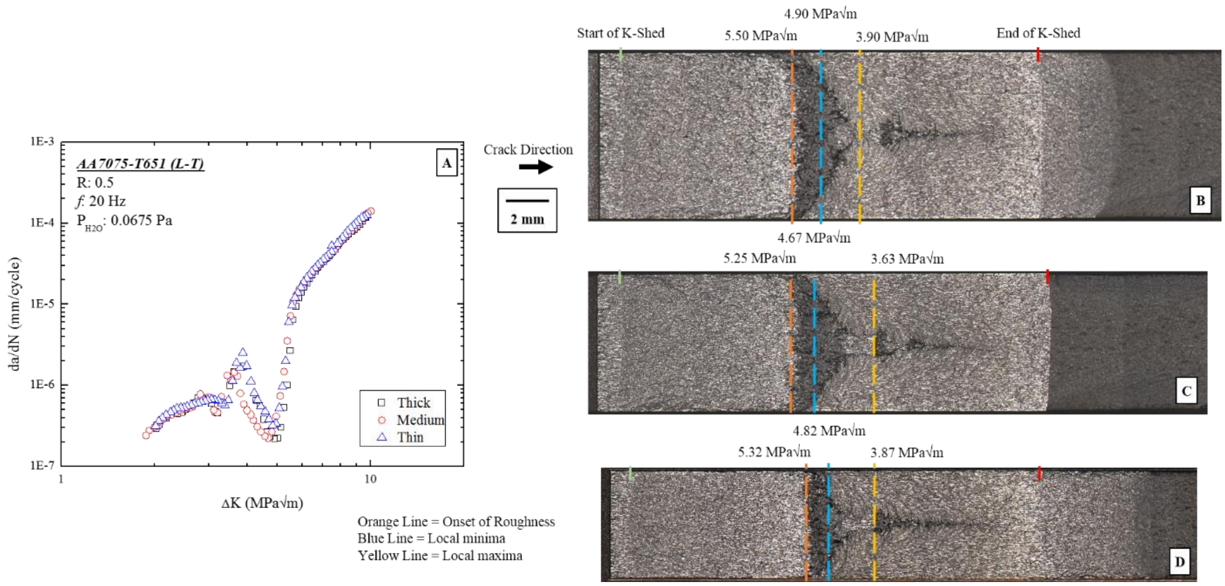

Figure 11: da/dN versus ΔK relationship (A) for thick medium and thin specimens at 0.675 Pa. Optical fractography of the thick, medium, and thin specimens are shown in B, C, and D. Orange lines marks onset of SBC, blue lines mark the bottom of the TTR, and the yellow lines mark the top of the spike after the false threshold. (Image created by Adam Thompson)

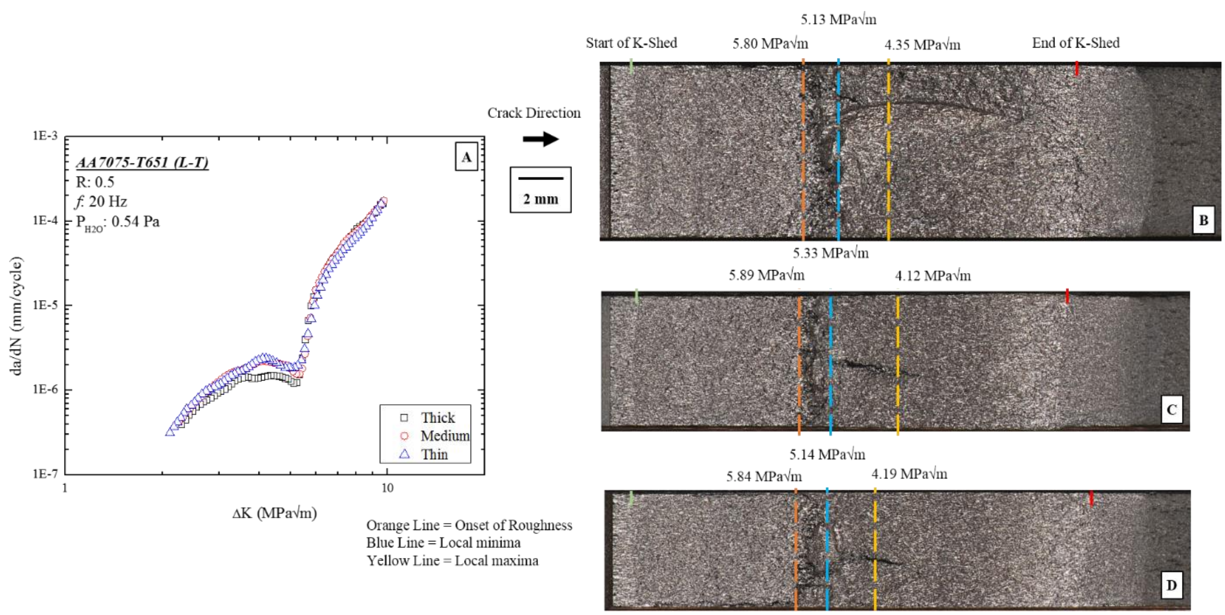

Figure 12: da/dN versus ΔK relationship (A) for thick medium and thin specimens at 0.54 Pa. Optical fractography of the thick, medium, and thin specimens are shown in B, C, and D. Orange lines marks onset of SBC, blue lines mark the bottom of the TTR, and the yellow lines mark the top of the spike after the false threshold. (Image created by Adam Thompson)

Figure 13 and Figure 14 detail the growth behavior fractography of 38 Pa and 2668 Pa (high humidity). FCGRs were higher than at UHV for the entirety of test and displayed no TTR behavior (as was expected at these pressures). Again, all three thicknesses displayed nearly identical behavior at both water vapor pressures.

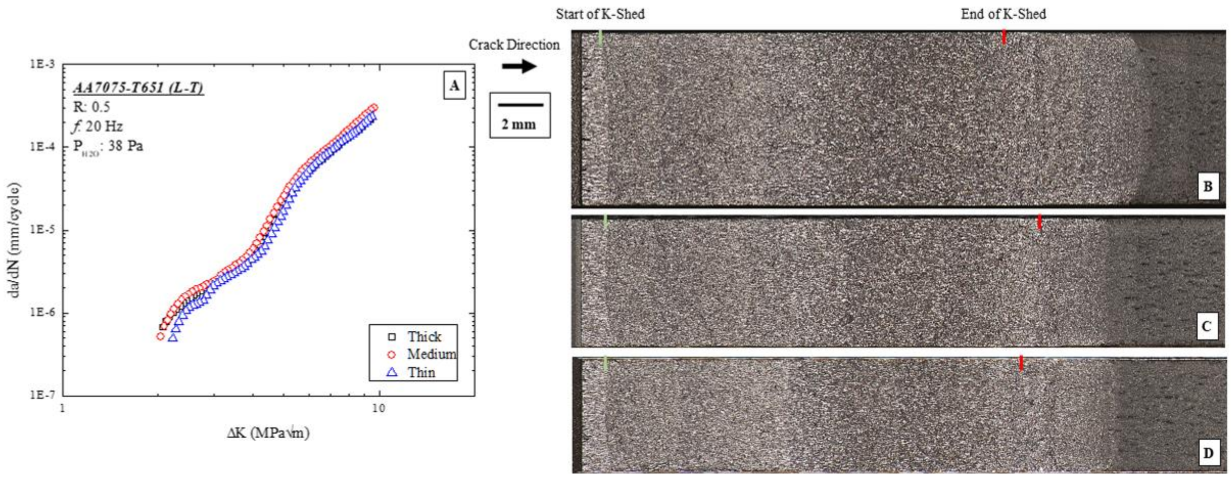

Figure 13: da/dN versus ΔK relationship (A) for thick medium and thin specimens at 38 Pa. Optical fractography of the thick, medium, and thin specimens are shown in B, C, and D. (Image created by Adam Thompson)

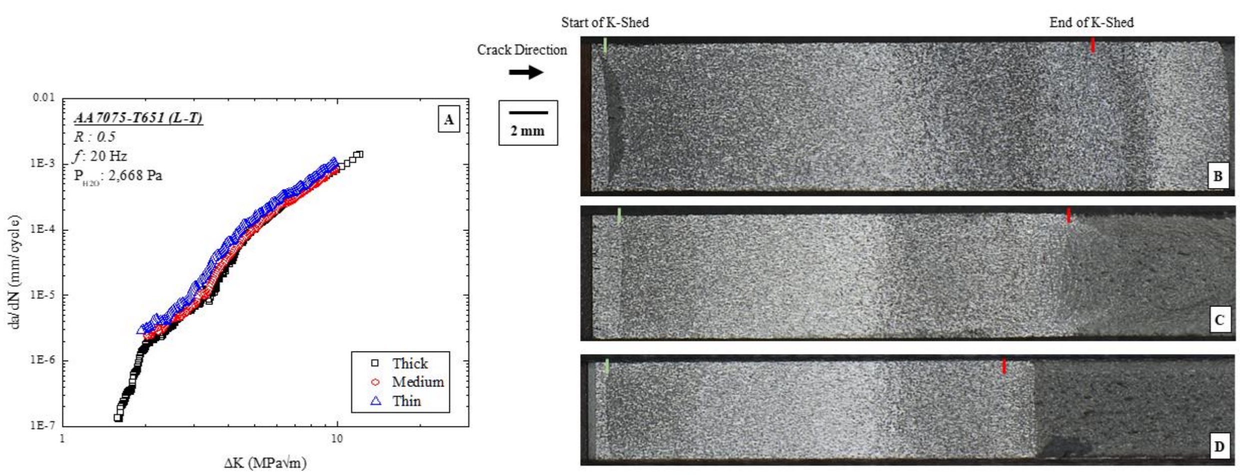

Figure 14: da/dN versus ΔK relationship (A) for thick medium and thin specimens at 2668 Pa. Optical fractography of the thick, medium, and thin specimens are shown in B, C, and D. (Image created by Adam Thompson)

3.4 Discussion

3.4.1 Review of Previous Experimental Results Relating to the TTR

The results show that limiting sample thickness is not able to affect the TTR behavior. It can be tempting to conclude that transport limitation is therefore not the controlling mechanism, however a deeper analysis is needed. To begin, a review of what previous investigations into the TTR have discovered. This analysis will not focus on proposed hypothesis, simply the experimental results so a full picture of the factors can be considered before an explanation for the sample thickness behavior is proposed. First, as explained previously, the TTR is a drop in growth rates at intermediate ΔK during a K-shed loading protocol, followed by a spike in growth rate.[13,54] This drop corresponds with an increase in roughness as the crack mechanism transitions to SBC. After this area of roughness, a flat transgranular morphology occurs on the edge of the sample while the center maintains a rough morphology. At the center of the sample, a morphology indicating rapid fracture occurs which corresponds with the spike in crack growth. Finally, the center again transitions to SBC morphology while the edges maintain a flat transgranular morphology.

Marker band testing during the TTR process was performed to investigate the crack shape during this process as it had been proposed that an irregular crack front was occurring during the TTR.[13,27,28,54] Figure 15 shows that at a ΔK of 5 MPa√m, prior to the transition to SBC, the crack front corresponds with the measured compliance crack length and has no irregularity across the entire width. At a ΔK of 4 MPa√m a severe crack front irregularity develops, where the crack has advanced far further along the edges of the sample, compared to the center. This irregular crack front is still present at a ΔK of 3 MPa√m, though it does appear to be less severe.

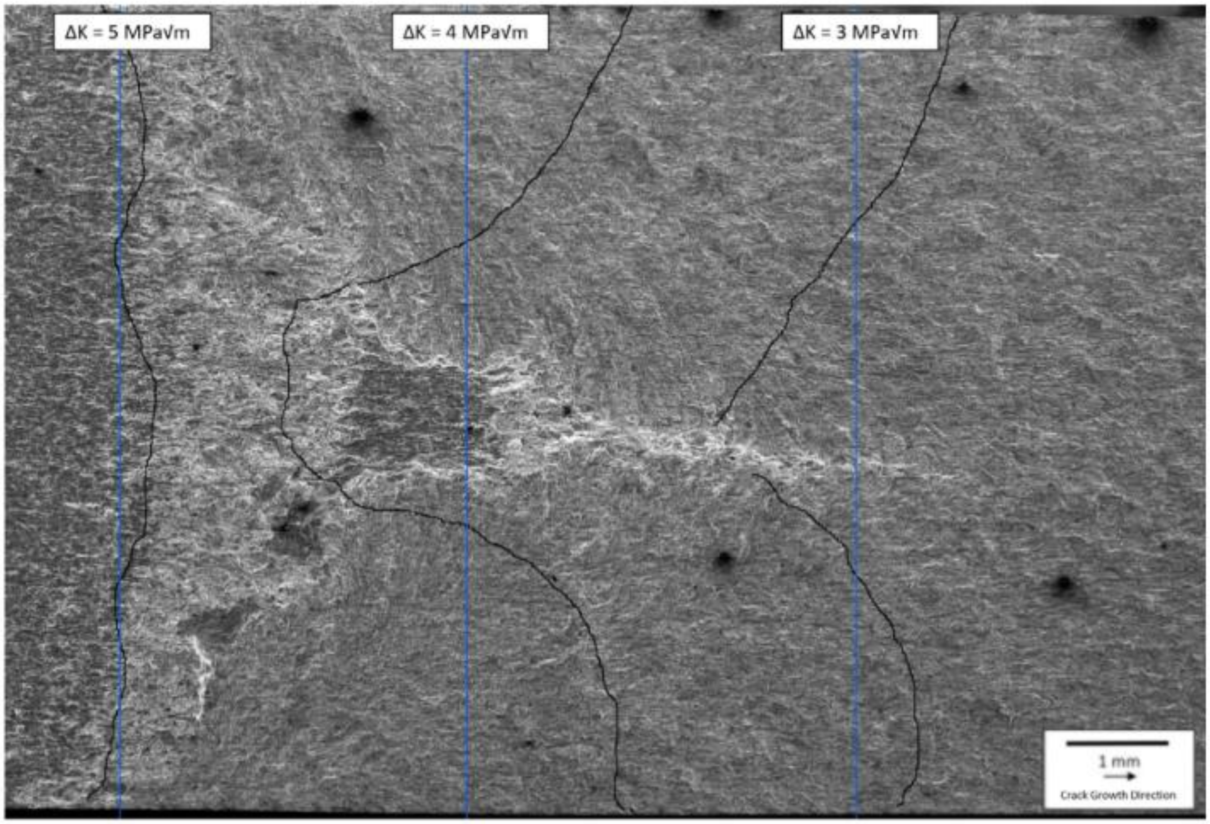

Figure 15: Marker bands produced during a K-shed loading protocol at 0.54 Pa. The crack front deduced via marker bands is shown in black while the measured crack length according to compliance measurments is indicated in blue. Marker bands were performed at ΔK of 5, 4, and 3 MPa√m. Crack growth occurs from left to right.[27,28,54]

Since the transition to SBC occurred just prior to the onset of the TTR behavior, the role of crack wake surface roughness was investigated. To do this, a constant ΔK test was performed at a ΔK of 5 MPa√m at 0.54 Pa and different spans of roughness were inserted into the crack wake prior to the beginning of the constant ΔK test. Figure 16 shows the result for 0.5 mm of roughness before the beginning of the test. The crack growth rate is very irregular with almost two order of magnitude swing in da/dN across with a minimal patter observed. The fracture surface shows a chaotic, irregular surface in the center of the sample where there is not a clear pattern. The edges of the sample do maintain a transgranular crack mechanism throughout the entirety of the test. In contrast, when 3 mm of roughness are introduced, the behavior is much more regular. Figure 17 shows that while similarly to behavior in 0.5 mm of roughness there are large swings (even larger), however the behavior is incredibly regular and consistent. The fracture surface also shows a very regular pattern, varying between SBC and ductile failure morphology in the center of the sample. The spikes in growth rate correspond with those ductile failure morphologies. The TTR behavior correspond where with the 0.0675 Pa and 0.54 Pa for the 3 mm and 0.5 mm of roughness experiments respectively. The 0.54 Pa K-sheds shown in Figure 12 have a small band of SBC morphology before the TTR and have a more chaotic and less severe behavior compared with 0.0675 Pa which has a thicker SBC band. This supports the findings that the severity, regularity, and self-perpetuating process in the TTR is dependent on the magnitude of roughness at the beginning of the process.

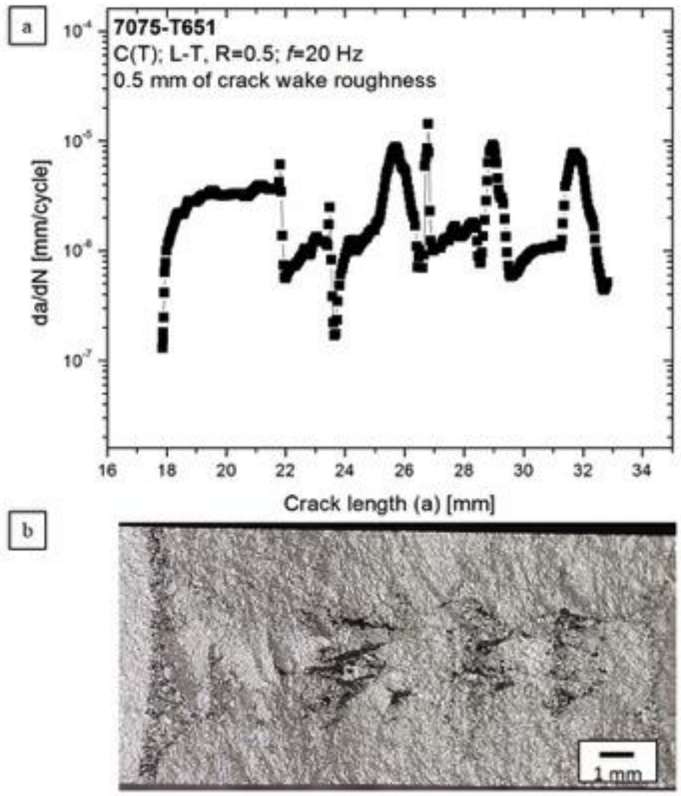

Figure 16: (a) FCGR versus crack length at a constant ΔK 5 MPa√m at 0.54 Pa. 0.5 mm of surface roughness was introduced onto the surface before the beginning of the test. (b) Optical fractography of the sample. This crack lengths in the graph correspond to the optical image.[27,28,54]

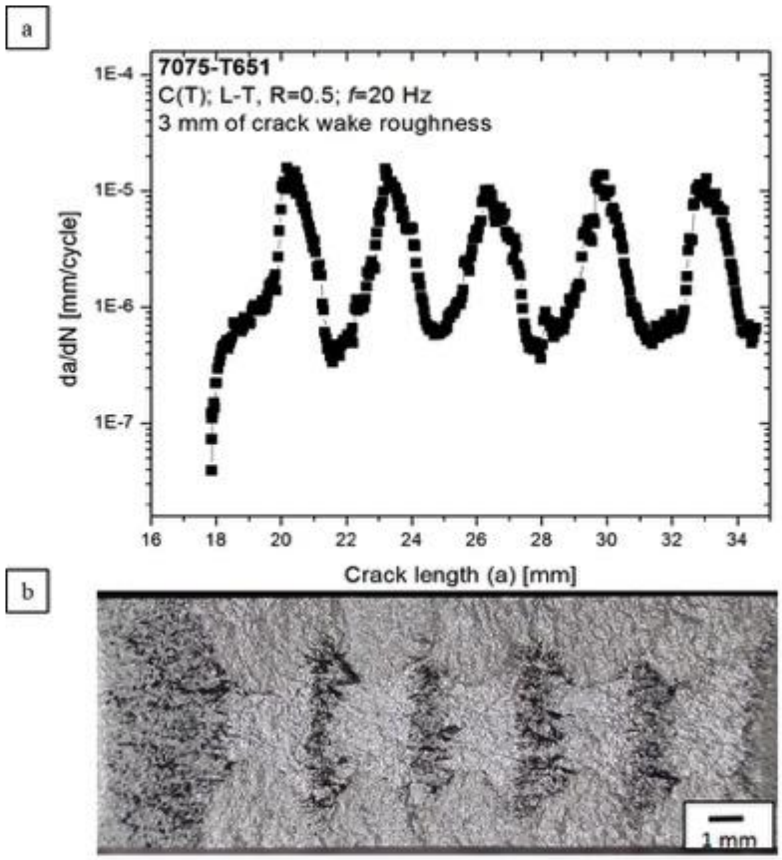

Figure 17: (a) FCGR versus crack length at a constant ΔK 5 MPa√m at 0.54 Pa. 3.0 mm of surface roughness was introduced onto the surface before the beginning of the test. (b) Optical fractography of the sample. This crack lengths in the graph correspond to the optical image.[27,28,54]

Finally, a constant ΔK test was performed where no prior roughness was induced and no large swings in growth rate were observed, shown in Figure 18. The fracture surface also shows no SBC behavior and is mostly smooth with a small spike of visible in the bottom third of the sample. While this does show that when no roughness is present, no TTR behavior is observed, critically this test was performed at a ΔK of 3 MPa√m and is therefore not a direct comparison to the tests where roughness was introduced, leaving open the possibility that even with no fracture surface roughness, a variable crack growth might occur at a ΔK of 5 MPa√m.

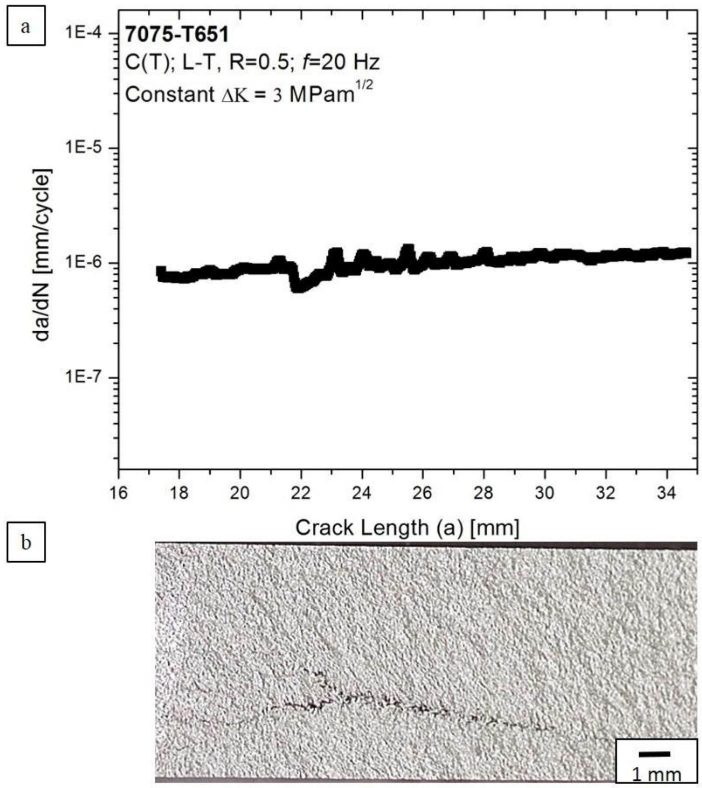

Figure 18: (a) FCGR versus crack length at a constant ΔK 3 MPa√m at 0.54 Pa. no surface roughness was introduced onto the surface before the beginning of the test. (b) Optical fractography of the sample. This crack lengths in the graph correspond to the optical image. [27,28,54]

Thompson performed K-rise testing to see what effect loading history might have on the TTR behavior.[59] The K-rise data at 0.0675 Pa, shown in Figure 19. It can be seen that multiple TTR events occur during the K-rise protocol and there are also multiple regions on the fracture surface where the morphology switches from rough SBC to a reflective, possibly cleavage morphology in the center.[59] Additionally, at the beginning of the TTR behavior there is a band of SBC across the entire sample before this varying morphology behavior begins. This is a critical finding as it had previously been thought that a specific loading history was required for the TTR to occur, however this shows that as long as low water vapor pressures are present and in a certain range of ΔK, the TTR can occur. However, it does support that a band of rough SBC is required to kick off the TTR behavior.

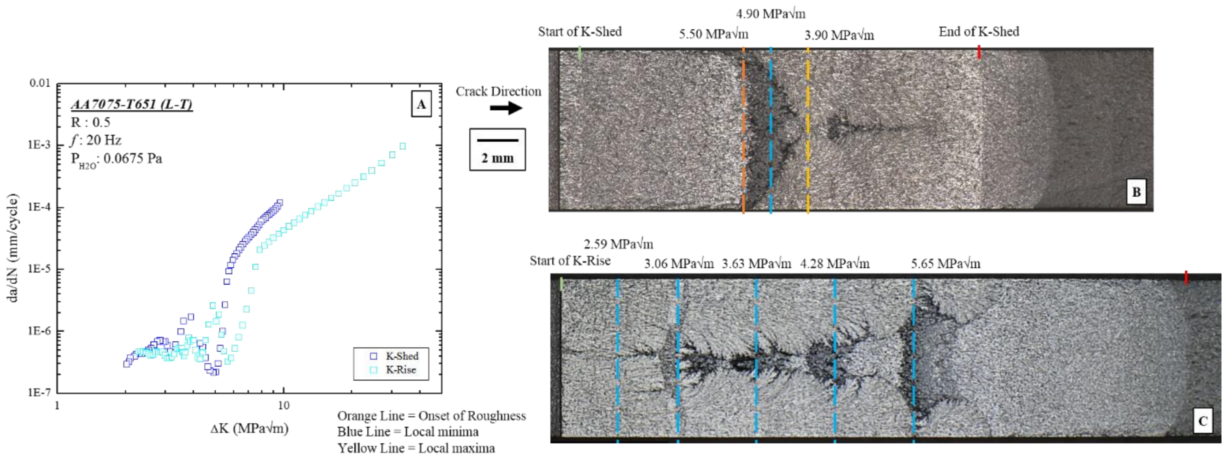

Figure 19: FCGR versus ΔK for both K-shed and K-rise loading protocol at 0.675 Pa. Fracture surface of the K-shed (b) and K-rise (c) are shown. For (b). orange lines indicate the start of roughness, the blue line indicates the local minima, and yellow lines mark the local maxima. For (c), blue lines represent the local maxima.[59]

These findings can be combined to make a list of experimental behavior that can be referred to in order to ensure that any proposed hypothesis properly takes all of these into account.

1. A band of rough, SBC morphology precedes the TTR behavior and is (most likely) required for the TTR to occur
2. An irregular crack front develops during the TTR where the crack advances faster on the edges of the sample compared to the center.
3. A rapid failure occurs in the center of the specimen after the irregular crack front develops, normalizing the crack front and resulting in the spike in growth rates.
4. A specific loading history is not required as long as cracking occurs in a specific water vapor pressure and ΔK region.
5. Changes in the sample thickness had no effect on the TTR behavior.

These findings will help guide the evaluation of the proposed hypothesis to explain the TTR behavior.

3.4.2 Development of the irregular crack front

The creation of the irregular crack front is a critical step in the TTR process and a more detailed description of how it develops is warranted. First a region of roughness needs to precede the formation of the irregular crack front. The conditions required for this roughness to develop were the subject of work by A. Thompson.[59] The roughness develops due to a transition to slip band cracking which occurs at specific ΔKs, (3-6 MPa√m) in a low to intermediate water vapor pressure environment.[59] This roughness modifies the flow behavior and impedes transport of water vapor both down the mouth of the crack tip, as well as transporting from the flanks of the specimen.[30] This starves the center of the sample of H_2O, retarding the H-embrittlement process in this area. As discussed in a previous chapter, as the concentration of H decreases the growth rate should also decrease. This occurs locally at the center of the specimen where the reduction in C_H in the center of the specimen decreases the crack growth rate locally. Meanwhile, directly where the crack meets the edge of the sample, there is no decrease in P_{H2O} as this point is directly exposed to the bulk environment. This leads to the crack growing from this point since it has a access to water vapor, increasing H-embrittlement, as well as possibly modifying the K profile, pushing the stress intensity outside of the range required for SBC.[59] These factors lead to a transition back to a flat, transgranular crack mechanism. Once this transition occurs, the smooth fracture surface no longer impedes the transport of water vapor and the semi-elliptical crack is able to progress, creating the irregular crack front. The effect of environment can be clearly seen when observing the crack direction of the irregular crack front. Pure mechanics considerations would cause the crack to lag at the edge of the sample, due to the lack of constraint at the free surface. In fact, the opposite is observed with the crack front bowing forward at the edges. This clearly demonstrates the role environment must be having for the crack to develop this way.

This process continues until a crack front observed in marker band testing (Figure 15) is formed. The same process occurs for the thick, medium, and thin specimens. It was hypothesized that the B thickness was controlling the transport distance and by limiting the sample thickness, the process detailed above would differ. However, the transport distance is not determined by the sample thickness, but by the size of the semi-elliptical side crack. As such, the transport distance between the thick, medium, and thin specimen are identical. It would be expected that as long as the local ΔKs on the edges of the sample are similar across thick, medium, and thin specimens, the side cracks will grow at a constant growth rate across all three samples as the local environment should be identical as there is no limitation of transport locally. Once the irregular crack front is formed, it has been suggested that the ΔK profile at the center of the sample increases dramatically, leading to an eventual straightening of the crack front.

3.4.3 Modeling of ΔK Profile for an irregular crack front

It had been hypothesized that as the sample thickness is changed, the location/severity of the spike should also change. This is based on two assumptions, (1) that the side cracks grow at the same growth rate across all three specimens, and (2) that the snap forward in the center of the specimen occurs at the same K_{max} for all thicknesses. In order to understand why the spike occurs at the same ΔK regardless of sample thickness, aspects of (1) and (2) need to be investigated. Before this can be done however, a better understanding of the K-profile along the irregular crack front is needed. While some work has been done, there is still a limited understanding on the K-solution for irregular crack fronts.[62–64] In order to study this, a collaboration with the University of Utah using Franc3D was performed to evaluate the stress intensity across the entire crack length. To do this, crack shapes from marker banded test showed in Figure 15 were evaluated at the loads applied at a target ΔK of 5, 4, and 3 MPa√m, shown in Figure 20, Figure 21, and Figure 22 respectively. It can be seen that at a ΔK of 5 MPa√m, when there is a relatively small change in ΔK across the crack front, with the ΔK_{max} - ΔK_{min} (ΔΔK) being just over 2 MPa√m. However, when an irregular crack front is present at a ΔK of 4 MPa√m, the ΔK ranges from 2-12 MPa√m, with the highest ΔKs occurring in the center of the specimen. This is again seen at ΔK of 3 MPa√m, though less severely with the ΔΔK being just over 4 MPa√m as the crack front is less irregular. These findings confirm that as the irregular crack front develops, the center of the sample undergoes are large increase in ΔK, giving credence to the hypothesis that the irregular crack front results in a rapid snap forward in the center due to a high applied K_{max}.

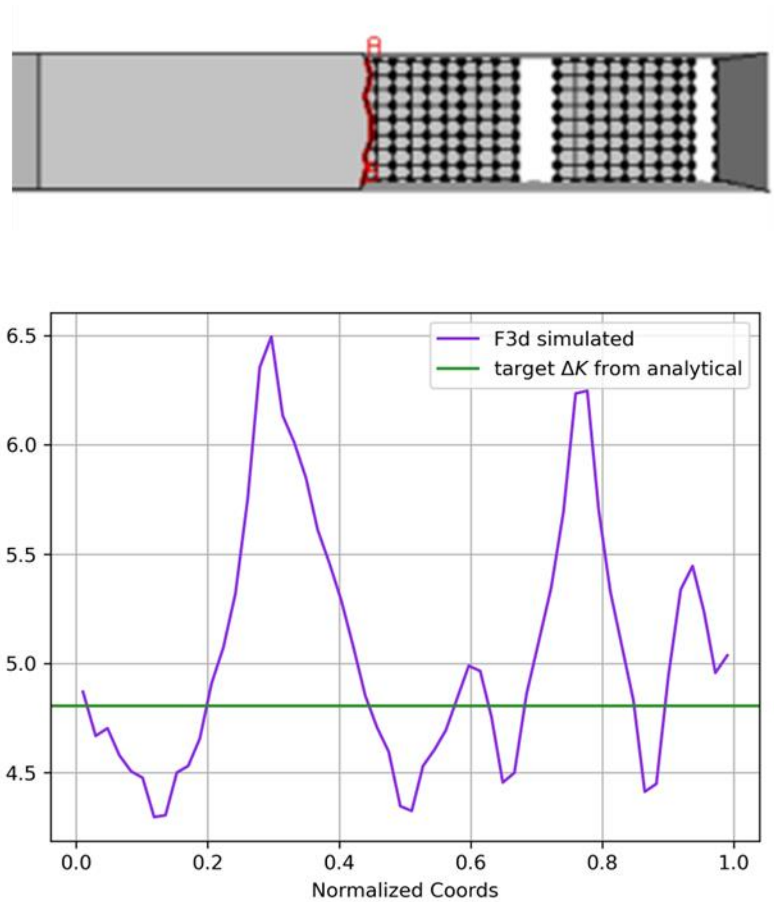

Figure 20: Stress intensity across the entire crack width at a target ΔK of 5 MPa√m and an R of 0.5. The crack shape is shown above the curve marked in red with the crack growing from left-to-right

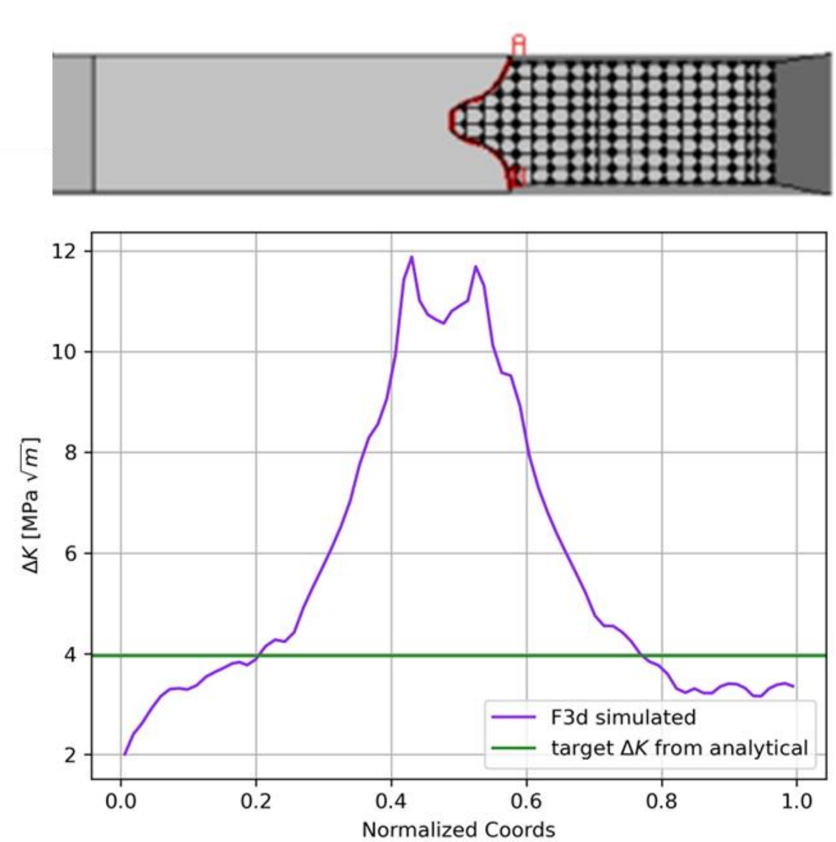

Figure 21: Stress intensity across the entire crack width at a target ΔK of 4 MPa√m and an R of 0.5. The crack shape is shown above the curve marked in red with the crack growing from left-to-right

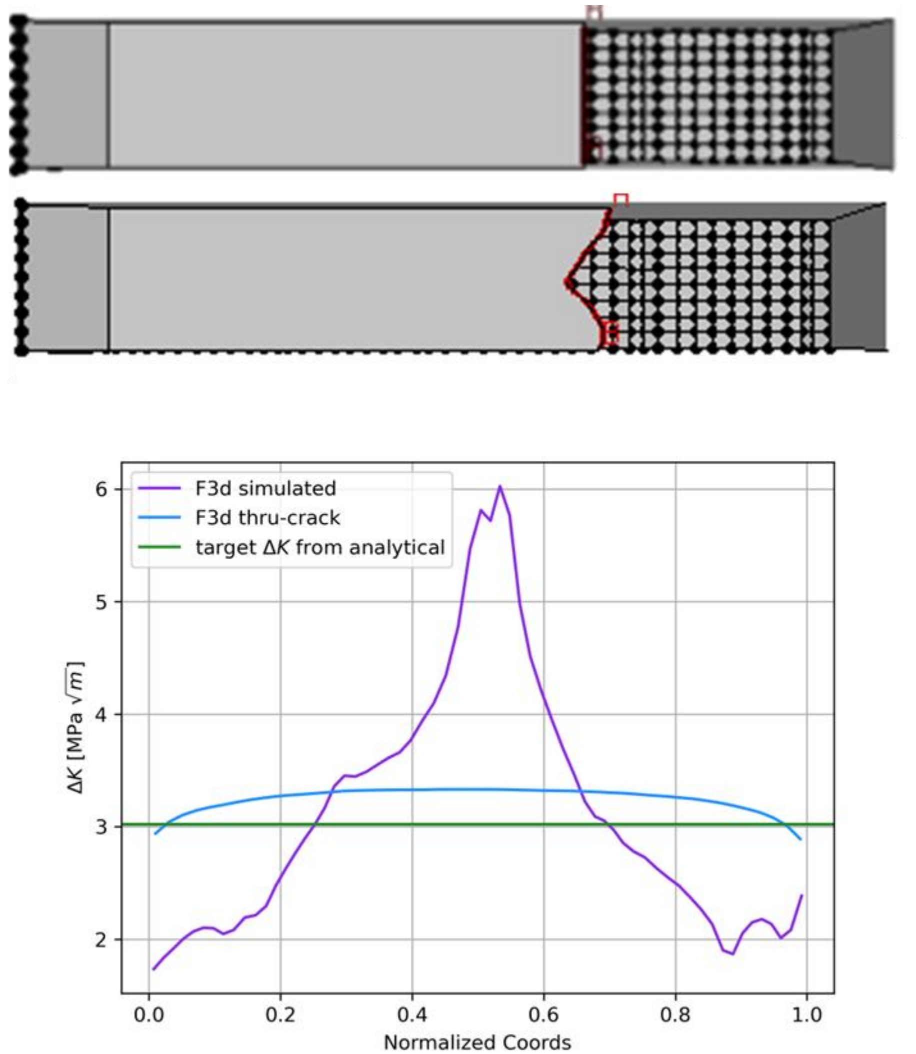

Figure 22: Stress intensity across the entire crack width at a target ΔK of 3 MPa√m and an R of 0.5. This was done for both the irregular crack front and a through crack. The crack shape is shown above the curve marked in red with the crack growing from left-to-right and the through crack marked in blue

3.4.4 Modeling of Constant Size Semi-Elliptical Edge Cracks in the TTR

Now that the ΔK-profile of the irregular crack front has been modeled, this can be utilized to investigate what is causing the identical TTR behavior in different samples with different thicknesses. As stated previously, according to the current proposed hypothesis, regardless of sample thickness, the growth rate from the side of the sample would be constant and result in the same size of edge cracks across all three thicknesses. This was modeled again using Franc3D, where semi-elliptical corner cracks of constant size were assumed to occur for thick, medium, and thin samples. At a ΔK of 4 MPa$\sqrt{m}$, these semi-elliptical cracks were placed on the edge of the samples and connected via a straight crack between them. In order to maintain a constant cracked area (suggested to be true via compliance measurements), as the ratio of semi-elliptical to straight crack changes between specimens, the semi-elliptical cracks were shifted with respect to the measured crack length. The stress intensity profile was then measured for each specimen and is shown in Figure 23. If the assumption of constant ellipse size is correct, then all three sample thicknesses should display similar K profiles in center as the three samples had a spike in growth rates at the same time. It can be seen that the thin coupon had a much larger increase in stress intensity in the center of the specimen compared to the medium and thick coupons. This would suggest that if constant sized crack fronts occurred across all three samples and the material at the center fails at the same K_{max}, the thin specimen should have a spike in growth rates earlier than the other specimens. Recalling back to Figure 11, the thick, medium, and thin specimens showed no difference in TTR behavior, suggesting that the constant sized elliptical crack assumption to develop these models is not a good assumption.

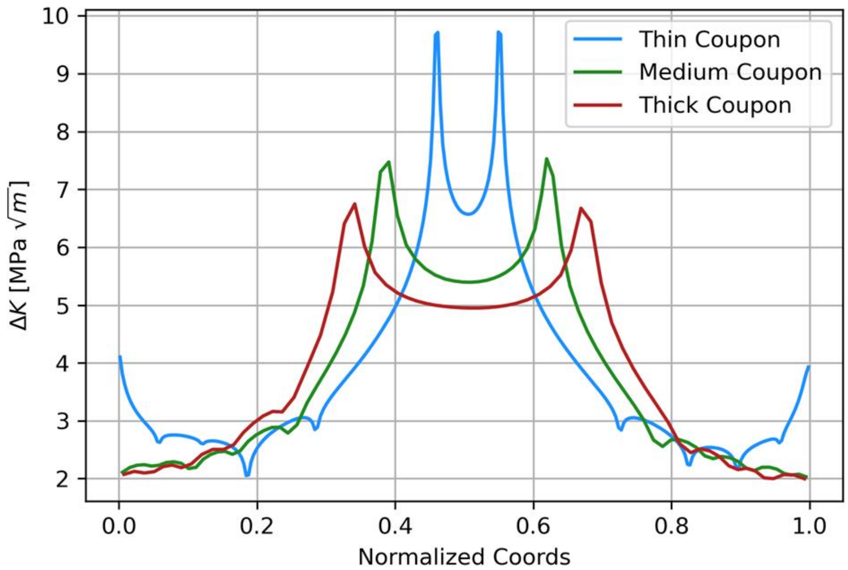

Figure 23: Modeling of thick, medium, and thin stress intensities with a constant sized, semi-elliptical crack on each edge using Franc3D. Simulated loading occurred at a ΔK of 4 MPa√m and a R ratio of 0.5

This leaves a couple of possible explanations as to why the thin and thick specimens spiked at the same ΔK. First, it is possible that K_{max} at failure in the center of the specimens is different. This could be due to differences in constraint between the specimens though this is dubious as according to ASTM E647, both samples are well within the thickness limitation to be in plane strain.[58] Secondly, the corner cracks could be growing at different growth rates, resulting in changes to the irregular crack front. There is ongoing work to continue this work to study if the corner cracks undergo the same ΔK in as they begin to grow in thick, medium, and thin specimens. This will reveal if the thin specimen has a lower applied ΔK on the edges. This would result in a slower growth rate on the edge of the sample and therefore a less severe irregular crack front, which could explain the identical behavior for the different thickness samples.

The current proposed hypothesis is not able to explain why the spike in growth rates occurred at the same ΔK for all three sample thicknesses, there are still possible explanations that would leave the hypothesis largely intact. It is critical to properly contextualize the results from this chapter and understand that it is possible that by slightly modifying the transport limited hypothesis, it is possible that this hypothesis will be able to explain why there is no difference in the TTR for samples with different thicknesses.

3.5 Conclusions

Testing of the TTR behavior was investigated by performing testing on multiple thickness samples to give insights into the possible mechanism controlling this behavior.

- Varying sample thickness testing did not show any impact on the fatigue crack growth behavior at any water vapor pressures and the fractures surfaces were very similar as well. This disproves the theory that by shrinking the sample thickness the TTR might be eliminated.
- Modeling efforts using Franc3D confirmed that at as an irregular crack front forms, the stress intensity spikes in the center, likely resulting in rapid fracture. Additionally, modeling of constant semi-elliptical cracks on the edge of the sample for different thicknesses are not consistent with experimental results. This indicates that the irregular crack front is unique for each sample thickness.
- Additional studies are needed to investigate why the varying sample tests saw spikes in growth rate at the same ΔK. The primary beliefs are that either the K_{max} is not constant between specimens or perhaps each sample experiences a different ΔK profile, resulting in unique corner crack growth rates between specimens.

Chapter 4 Effect of Low Temperature, Low Water Vapor Pressure Environments on the Fatigue Behavior of an Al-Li Alloy

Note: Previous researchers at UVA and Arconic Technology Center (ATC) had performed a series of tests at various temperatures and pressures on 2199, similar to testing done on 7075. In the current PhD effort this data was collated and further analyzed to examine the differences and similarities between 7075 and 2199 and to bring the work to the level of an archival literature paper. This resulted in a published paper entitled *Effect of low temperature, low water vapor pressure environments on the fatigue behavior of an Al-Li aerospace alloy* in the International Journal of Fatigue in 2021.[65]

4.1 Introduction

4.1.1 motivation for the study of 2199

As discussed in the previous chapter, the crack wake morphology can have drastic impacts on the FCGR in 7075. While the phenomenological details and flow path considerations have been studied for 7075-T651, such molecular flow based complexities are likely to be more prominent for Al-Li-Cu alloys, which typically are strongly textured and contain coherent and shearable δ' precipitates.[66–70] For fatigue in a wide range of environments and ΔK, these microstructural characteristics result in highly localized planar slip and a SBC cracking mechanism that produces a tortuous crack path [47,66,75–77,67–74]. Molecular flow effects are likely critical to the environmental cracking behavior in Al-Li-Cu alloy systems, but such effects have only been lightly explored.[10,27]

4.1.2 Effect of Temperature on FCGR

Prior chapters established that impedance of molecular transport via crack wake roughness can compromise FCGR similitude at a constant exposure/water vapor pressure. However, recent efforts have demonstrated that a lack of similitude in 7075-T651 between room temperature and low temperatures despite testing at a constant ΔK, R, and P_{H2O}/f value. Specifically, test temperatures below -30°C exhibited significantly slower crack growth kinetics when compared to tests conducted at the same P_{H2O}/f values at 23°C.[5,17] Such behavior could be attributed to either a temperature dependent impact on the crack tip plastic damage accumulation (independent of H)[78–84] and/or a temperature induced retardation of one of the several steps in HEE process[85–91]. A systematic evaluation of 7075-T651 demonstrated the changes in loading rate and fracture morphology were consistent with a temperature induced change in the ΔK and P_{H2O}/f ranges where SBC was observed, which in turn impacted the molecular flow aspect of the HEE process.[5] Due to the primary importance of the onset of SBC to this phenomenon it is useful to quantify how this behavior manifests in a material system that exhibits a rough SBC morphology over a wider range of loading and environmental conditions (e.g. Al-Li-Cu alloys).

4.1.3 Research Goals

The overarching objective of the current study is to evaluate the fatigue crack growth behavior of a third-generation Al-Li-Cu alloy (2199-T86) in environments relevant to high altitude flight. The propensity of SBC in these alloys will enable better understanding of the extent to which crack wake/geometry morphology impacts the molecular transport aspect of the HEE process across relevant aerospace Al alloys. Furthermore, these data and analysis will inform the data generation protocol necessary to establish rigorous environmental da/dN vs. ΔK relationships. Three specific knowledge gaps were addressed to fulfill these general goals. First, the crack growth kinetics will be quantified for 2199 via LEFM based testing at various P_{H2O} and temperatures relevant to high altitude environments. These data were coupled with fractographic analysis to determine if the observed crack growth rate behavior correlates to variations in crack wake roughness. Second, data obtained at constant P_{H2O}/f values but different temperatures will be compared to determine the extent to which similitude is compromised by different loading temperatures in an alloy that is prone to planar slip. Third, the results from each of these tests will be analyzed in the context of the HEE-based mechanisms developed in parallel work on 7075-T651.[5] This will inform the extent to which the mechanisms governing environmental cracking behavior varies for alloys prone to different bulk slip character (e.g. 7075-T651-wavy versus 2199-T86-planar).

4.2 Experimental:

4.2.1 Material

Fracture mechanics-based fatigue testing was performed on samples excised from a 50.8 mm thick plate of 2199-T86 supplied by Arconic. The nominal composition of the 2199 alloy is shown in Table 5.[92] The expected strengthening precipitates in the aluminum alloy are the T_1 (Al_2CuLi), θ’ (Al_2Cu),T_2 (Al_6CuLi_3), and the δ’ (Al_3Li).[92] The yield strength was 423 MPa in the rolling direction. The nominal plane strain fracture toughness is 47 MPa√m in the Transverse (T)-Longitudinal (L) loading orientation and 59.5 MPa√m in the L-T orientation.[92] The grain sizes and texture of the plate was not quantified. Compact tension samples (CT) were excised from the T/7.3 location of the plate thickness. The CT samples had a width of 50.8 mm and a thickness of 7.62 mm with a notch depth of 12.7 mm; some samples were side grooved to a net thickness of 6 mm along the Mode I crack path.

Alloy (Wt%)	**Cu**	**Li**	**Zn**	**Mg**	**Mn**	**Zr**	**Fe**	**Si**	**Al**
	2.3-3.9	1.4-.18	0.2-0.9	0.05-0.40	0.1-0.5	0.05-0.12	0.07 max.	0.05 max.	Remainder

Table 5: Aluminum alloy 2199 composition (Wt %)

4.2.2 Loading Protocol

Fracture mechanics-based fatigue testing was guided by ASTM E647 using a computer-controlled servo-hydraulic machine to apply a sinusoidal waveform. The crack length was calculated via compliance measurements using a clip gauge at crack mouth; [58] the challenges and applicability of this method for portions of the testing exhibiting an irregular crack front are detailed elsewhere.[28] Testing was performed at a constant stress ratio (R) of 0.5 and frequency (f) of 20 Hz using a K-shed protocol following the formula $\Delta K=\Delta K_o \exp[C(a-a_o)]$ with ΔK_o = 14.85 MPa√m, a_o=13.7 mm C=0.08 mm^{-1}.[13,58] This decreasing K test continued until da/dN was roughly $5x10^{-8}$ mm/cycle or ΔK reached 2 MPa√m. The decreasing ΔK-test was followed by an increasing ΔK-test from a ΔK of 4 to 12 at a C=0.2 mm^{-1}.

4.2.3 Environmental control

All 23 °C tests were performed at the University of Virginia, while low temperature testing was performed at the Arconic Technology Center (ATC). Replicate tests at 23 °C at high humidity were conducted to ensure consistency between labs. Further testing at 23 °C was performed at the following water vapor pressures: 2668 Pa, 340 Pa, 165 Pa, 38 Pa, 4 Pa, 0.54 Pa, and UHV. To remain consistent with previous work,[28] P_{H2O} will be used to describe the loading environment. While P_{H2O}/f is generally the operative exposure parameter, since all tests (excluding one) were performed at a constant 20 Hz frequency, this will not impact comparisons.

The 2668 Pa environment was maintained within a Plexiglas environmental cell fed with water saturated nitrogen in order to achieve >95% relative humidity. The low water vapor environment was maintained within a Cu gasket sealed UHV chamber. For each case a multi-scale pumping procedure was used to achieve vacuum levels below 10^{-7} Pa. Subsequently high-purity, triple distilled water vapor was introduced to the chamber using a sealed glass flask with a leak valve.[13] The desired water vapor pressure was held constant throughout the test by balancing the flow of water and the degree of pumping on the chamber.

Low temperature environment tests were conducted at -4 C, -15 °C, -30 °C, -50 °C, and -65 °C. This environment was detailed in previous work and is repeated here.[5] These environments were achieved by controlled flow of liquid nitrogen using a solenoid into a furnace casing affixed about a servo-hydraulic testing frame. Containers of water were placed within the furnace casing at the beginning of the cooling procedure to ensure a high initial humidity in the chamber. As the chamber is then cooled, a thin layer of ice is formed on the sample and it is assumed that the water vapor pressure at the crack mouth and flanks is equal to equilibrium water vapor pressure above ice at the achieved temperature. This assumption is justified if there is a thin layer of ice on the surface of the sample, even if the bulk pressure in the chamber deviates from the equilibrium value. The Clausius-Clapeyron relationship can be used to calculate the $P_{H2O\text{-}ice}$ at each temperature. 308 Pa at -4 °C, 125 Pa at -15 °C, 38 Pa at -30 °C, 5.4 Pa at -50 °C, and 0.54 Pa at -65°C. The global temperature and humidity were measured inside the chamber during testing at a distance 150-200 mm from the sample. The average global water vapor pressures for each temperature were 385.5 Pa at -4 °C, 125Pa at -15 °C, 95 Pa at -30 °C, 1.78 Pa at -50 °C, and 0.44 Pa at -65°C. In all, the measured bulk values of water vapor pressure correspond reasonably well with the calculated equilibrium values.

4.3 Results

4.3.1 Comparison of 7075 and 2199 aluminum alloys at high humidity and UHV

A comparison of the crack growth rates of 2199 and 7075 alloys in Figure 24 shows that the 2199 has superior fatigue performance at both UHV and high relative humidity environments. This is consistent with prior literature findings and is proposed to be controlled by extrinsic toughening mechanisms.[93] Specifically, the interaction of slip with microstructural features modifies the crack path,[42,73,94,95] which in-turn impacts the crack tip driving force. In 7xxx series over-aged alloys, precipitation of the incoherent equilibrium η-phase and semi-coherent metastable η' phase ($Mg(Zn,Al,Mg)_2$ is primary mechanism by which the alloy is strengthened. These phases encourage dislocation looping and heterogenous slip.[10] In Al-Cu-Li alloys, the T_1 (Al_2LiCu) and δ' (Al_3Li) phases allow homogenous and reversible planar slip resulting in highly facetted cracking leading to enhanced roughness that can result in enhanced fatigue propagation resistance due to increased crack closure, crack deflection, and mode II displacements.[42,73,93,96] These extrinsic toughening mechanisms reduce the crack tip driving force and have been proposed as the mechanism governing the Al-Cu-Li alloys improved fatigue performance.[95]

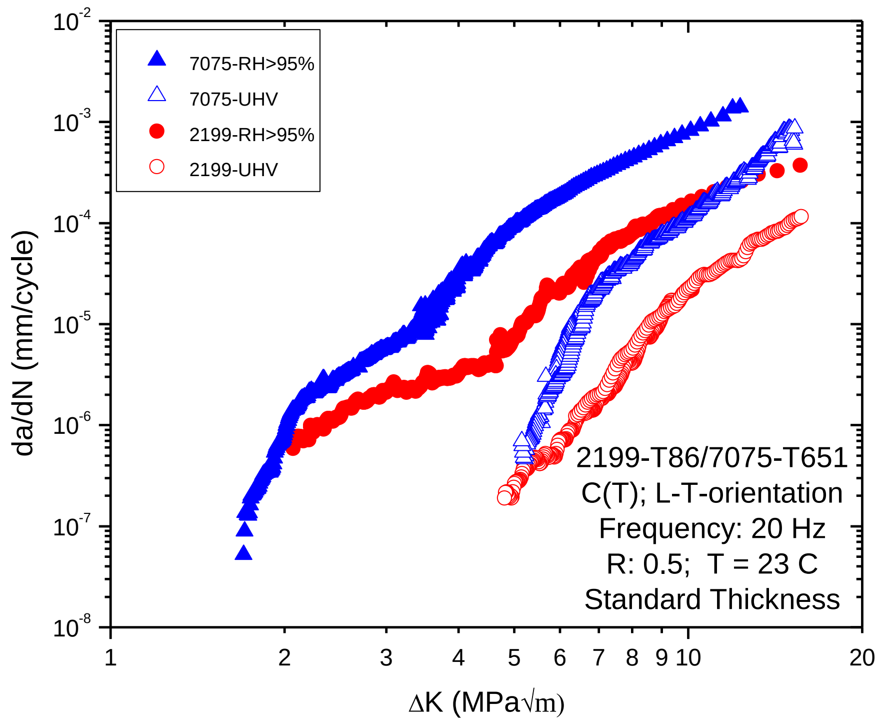

Figure 24: Fatigue crack growth rates versus ΔK from K-shed testing comparing 2199 and 7075-T651 aluminum alloys in UHV and high humidity environments at room temperature.

Near threshold, growth rates for the UHV tests began to converge for the different alloys. It has been proposed that this is due to a transition in 7075 to faceted slip band cracking at low ΔK and low water vapor environments.[17] This roughened morphology may cause the same extrinsic toughening responsible for the decreased crack growth rates in 2199. Similarly, the convergence of the two growth rates in high humidity environments is proposed to be due to another crack morphology transition in 2199 to flat sub-granular and/or cleavage cracking as has been observed in 2090 at similar ΔK values and high humidity environments.[97]

4.3.2 Fatigue crack growth rates versus ΔK at variable P_{H2O}

The fatigue crack growth rates for 2199 aluminum as a function of ΔK and P_{H2O} at 23 °C are shown in Figure 25. Growth rates at water vapor pressures of 165 Pa and above were obtained using standard CT samples. However, the onset of out-of-plane cracking necessitated the use of side-grooved samples at the lower P_{H2O} values. The correspondence between the side-grooved and standard sample results at UHV demonstrate the mechanical equivalence between the two samples when out of plane cracking is avoided. Side-groove dimensions were in accordance with ASTM E399. The results for the 2199 are largely consistent with trends observed previously for 7075.[13] Four aspects of the crack growth kinetics in Figure 25 are relevant. First, as expected, at high humidity, frequency changes from 2 to 20 Hz do not impact the crack growth rate (2668 Pa and 2668 Pa (2 Hz)). Second, for P_{H2O} of 165 Pa and above all growth rates exhibit a single trend (with the exception of a slightly higher ΔK_{TH} for 165 Pa) where da/dN decreases with ΔK in several power law segments. This behavior is consistent with prior results for Al-alloys undergoing the HEE process.[13,35,43,98] Third, decreasing P_{H2O} below 165 Pa results in a general decrease in crack growth rate over a wide range of ΔK. Threshold values steadily increased from 2.3, 2.7, and 5 MPa√m for 165 Pa, 38 Pa, and 0.5 Pa/UHV respectively (Table 6). Fourth, the 0.05 Pa results align with the UHV suggesting that the environmental contribution is fully eliminated at this P_{H2O} value and below when testing at ambient temperature.

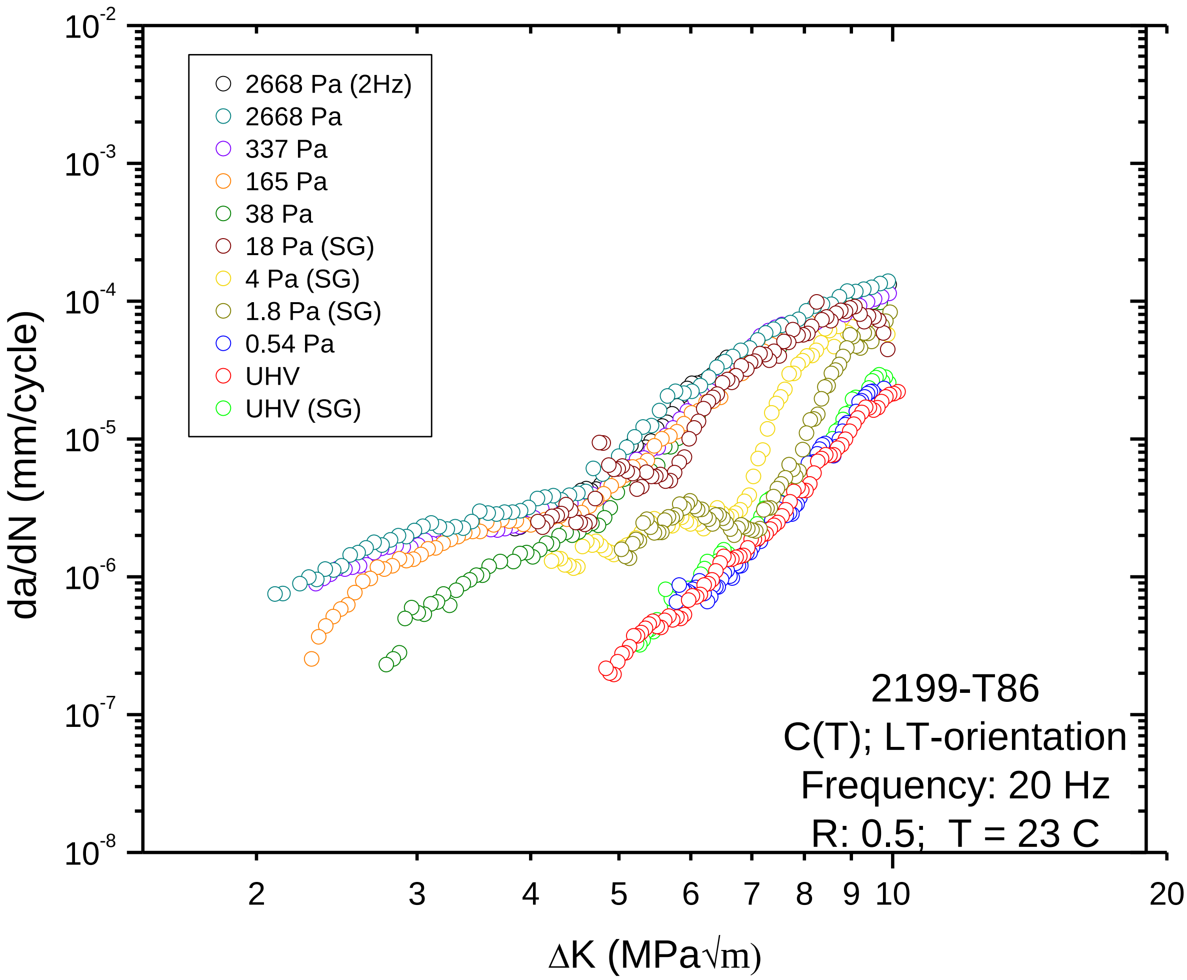

Figure 25: Crack growth rates versus ΔK from K-shed testing of 2199 at various P_{H2O}. R of 0.5, and a frequency of 20 Hz (unless noted) at room temperature. Side-grooved samples are indicated as (SG). 165 Pa, plot is a combination of side-grooved (above ΔK = 4.8 MPa√m)

P_{H2O}	ΔK threshold
165 Pa	2.3 MPa√m
38 Pa	2.7 MPa√m
0.5 Pa	5 MPa√m
UHV	5 MPa√m

Table 6:The ΔK at threshold for various water vapor pressures.

An important feature is the rapid decrease in crack growth rate from 8.5 to 5 MPa√m at 1.8, and 4 Pa, followed by an increase in da/dN. This phenomenon has previously been observed in 7075 at low/intermediate ΔK and P_{H2O} values and has been termed the threshold transition regime (TTR).[5,13,28,54] This behavior has been systematically evaluated.[28] The initial sharp decrease is attributed to a shift in the cracking morphology to a rougher/more tortuous path. While extrinsic toughening (such as closure and a reduction in the driving force due to a more tortuous path) are relevant, the sharp decrease in growth kinetics was found to be governed by a roughness induced retardation of the molecular flow from the bulk to the crack tip in 7075.[28] The result of this behavior was preferential semi-elliptical cracking progressing from the sides of the sample. The resulting irregular crack front (longer on the flanks and a shorter in the center) results in a non-homogeneous driving force along the crack front (higher ΔK at the center).[99] When this discrepancy reaches a critical value (governed by the non-homogenous K along the crack front), the center of the crack rapidly advances resulting in a sharp increase in da/dN; as is observed in the 4 Pa data in Figure 25.[5,13,28,54] The 2199 results demonstrate less dips and spikes associated with the TTR than were observed for 7075. In prior work, this behavior was quantitatively evaluated by demonstrating that the da/dN minimum scaled linearly with P_{H2O} (at constant f); a similar linear trend is observed for 2199, albeit with a less pronounced dependence.[54] Additionally, in 2199, the water vapor pressures at which the TTR occurs are higher than for 7075.[54]

A plot of da/dN (from Figure 25) versus exposure parameter at constant ΔK are shown in Figure 3 along with the trend from a separate lot of 2199 at 7 MPa√m, R=0.58, and f=20 Hz[42] (black line). Trend lines are fit to the data following theoretically based models that propose three distinct regions.[10] The first region occurs at low exposures, where there is insufficient water vapor available to support the HEE process, thus crack growth is dominated by mechanical damage accumulation and is independent of P_{H2O}. The second region is limited by transport of water molecules to the crack tip, this transport is governed by Knudsen flow and growth rate is directly proportional to the exposure parameter. Finally, the third region has mild dependence on P_{H2O} that is controversially attributed to a change in the rate limiting process to H diffusion within the process zone.[16,40] This data shows a roughly 26-, 25-, and 6-fold increase in growth rates from UHV to 2668 Pa (2Hz) at 5.5 MPa√m, 7 MPa√m, and 10 MPa√m respectively; the decreased impact of water vapor at the higher ΔK is consistent with the increasingly dominant role of mechanical damage.[40]

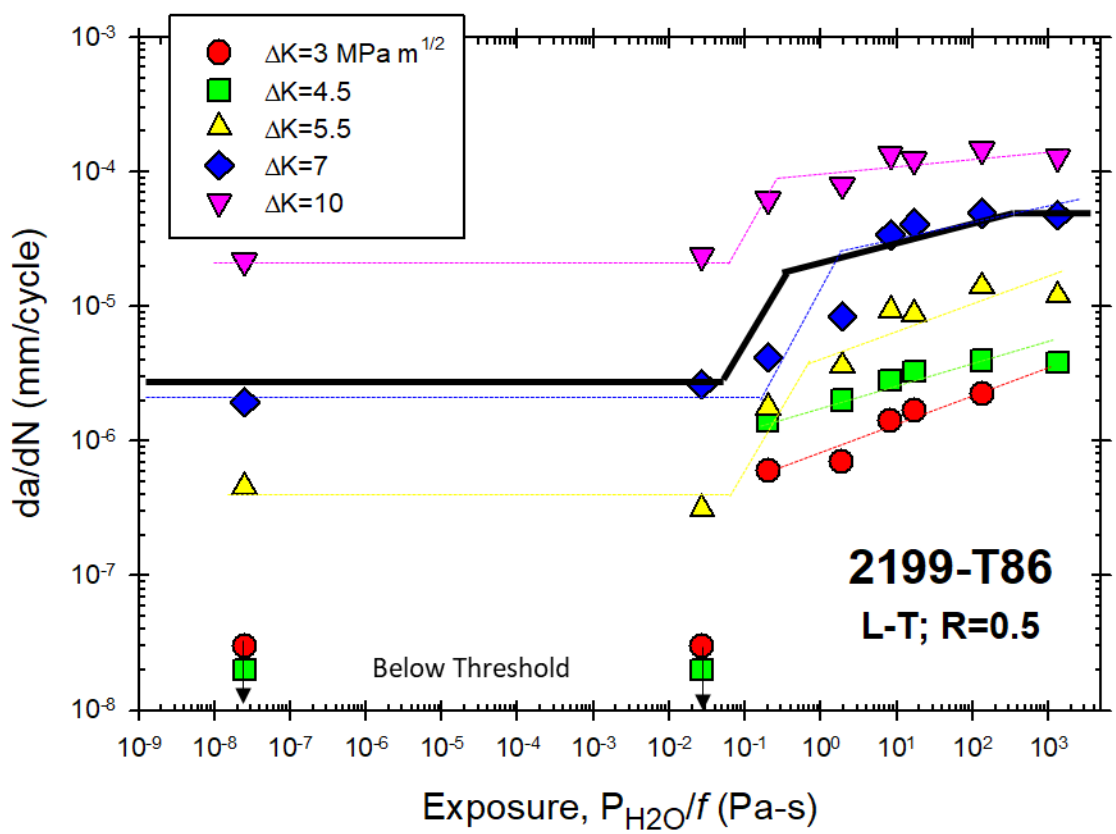

Figure 26: Room temperature growth rates plotted versus exposure parameter, PH2O/f for several different constant ΔKs. A trend from a separate lot of 2199 at 7 MPa√m, R=0.58, and f=20 Hz[42] *at various exposures (black line)*

4.3.3 Analysis of fracture surface

The onset of the TTR has been hypothesized to occur due impedance of molecular transport caused by SBC-like features at low water vapor pressures and medium-to-low ΔK.[54] Al-Li alloys are known to exhibit faceted cracking (SBC-like features) across a larger range of stress intensities than in 7075.[100] Such differences could lead to 2199 experiencing a different environmental dependence at low water vapor pressure and ΔK than that seen for 7075.[93,100] As such, investigation of the crack morphology of 2199 can provide insight on the extent of mechanistic commonality between 2199 and 7075.

Figure 27 shows optical micrographs and SEM images of the fracture surface from side-grooved fatigue tests (Figure 25) performed under several humidity levels at room temperature. The red boxes outline fracture surfaces associated with the K-shed portion of the testing, and the solid, long-dash, and short-dash lines indicate the nominal crack position at 9, 7, and 5 MPa√m. For decreasing ΔK tests, at 18 Pa and above (Figure 27e and f), as well as at UHV (Figure 27a), the fracture surface was generally uniform for the entirety of the K-shed. At 4 Pa and 1.8 Pa (Figure 27c and d), a transition from a smooth surface to areas of increased roughness in the center of the sample was observed. The change in crack wake morphology correlates with the onset of the TTR for 4 Pa and 1.8 Pa; as demonstrated in detail for 4 Pa in Figure 28. Prior to the decrease in growth rate, the fracture surface was relatively smooth. As the surface develops a roughness at ΔK ~8.5 MPa√m a corresponding drop in the growth rate is observed. Finally, as the growth rates recover, the fracture surface transitions back to a smooth surface. Additionally, after the minima there is evidence (e.g., a smoother surface) that cracking preferentially progresses from the sides, resulting in an irregular crack front. This correlates with what was observed in 7075 where an irregular crack front develops due to increased environmental contribution on the edges of the sample.[28] This was hypothesized to be due to shorter molecular transport distances enabling an enhanced level of embrittlement proximate to the crack flanks.[28]

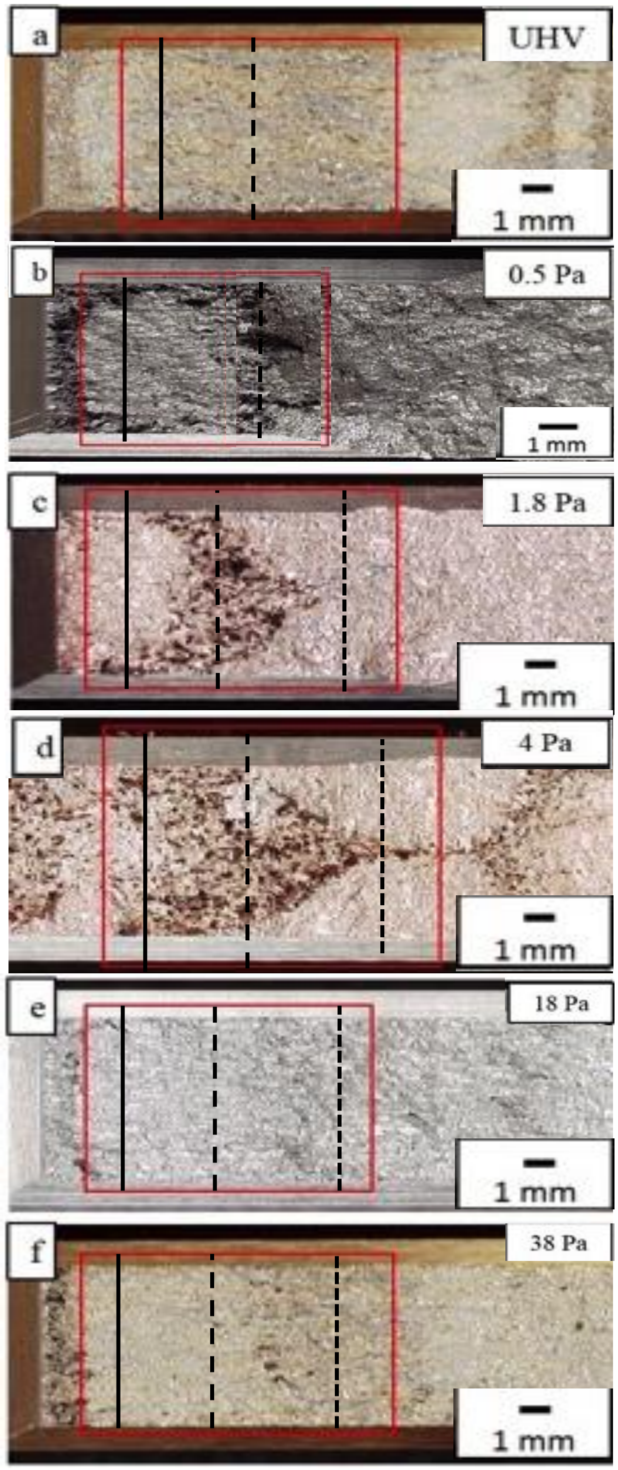

Figure 27: Optical fractography of the fracture surface of side grooved samples at 23 ◦C for UHV (a), 0.05 Pa (b), 1.8 Pa (c), 4 Pa (d), 18 Pa (e), and 38 Pa (f). Red boxes indicate the area cracked during the K-shed. Black lines locate the crack position at ΔK of 9 (solid), 7 (dashed) and 5 (dotted) MPa√m.

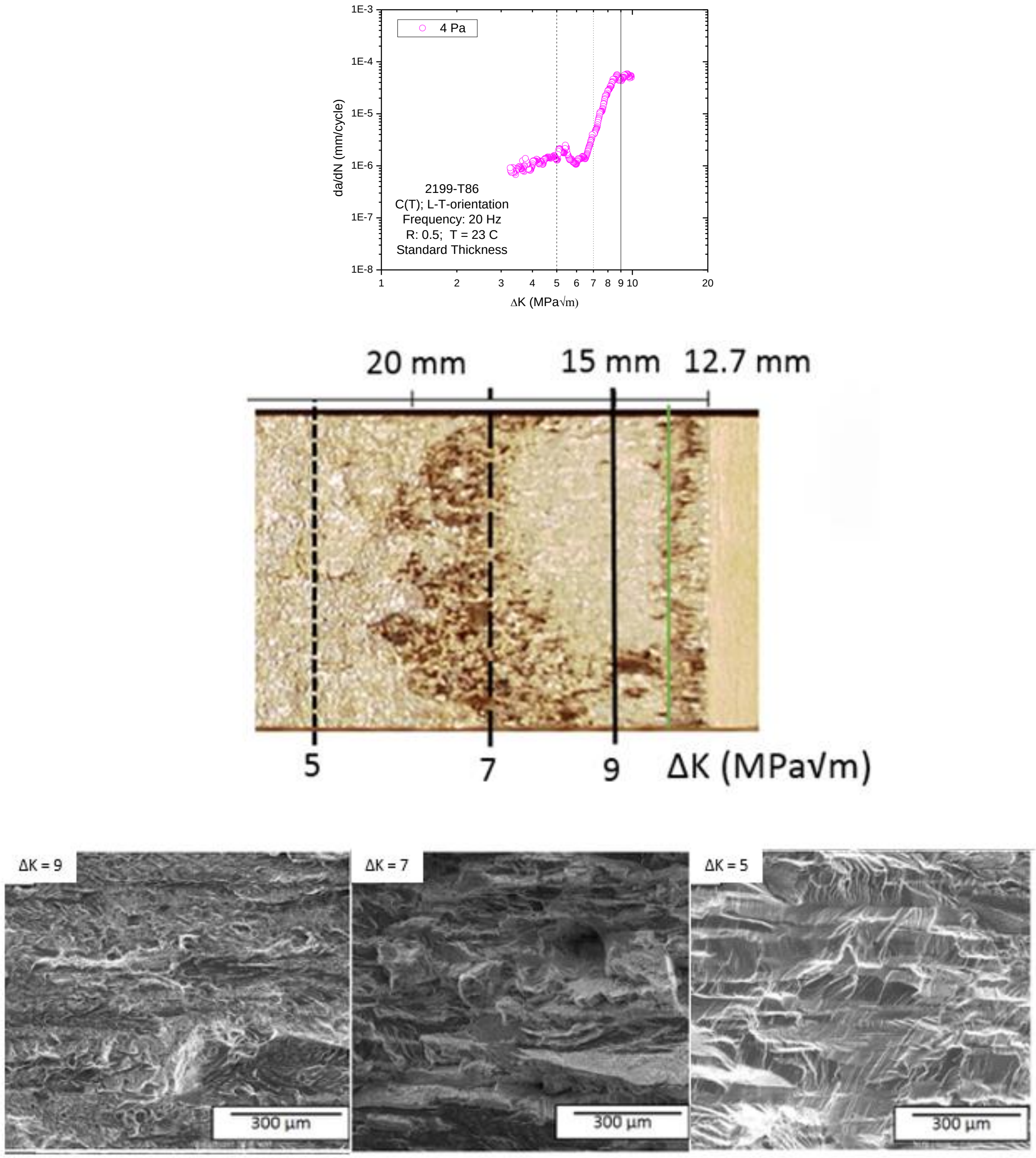

Figure 28: Crack growth rate versus ΔK and corresponding optical fractography and SEM micrographs illustrating the transition from smooth to rough topography on the fatigue crack surface of 2199 at 4 Pa. ΔKs of interest are marked both on the graph and on the fracture surface. The green line indicates the start of the K-shed after the precrack.

SEM images taken at ΔKs of 9, 7, and 5 MPa√m for all tested water vapor pressures at room temperature are shown in Figure 29, Figure 30, and Figure 31 respectively. Faceted cracking (SBC-like features) was observed at UHV for all ΔK values, with a higher degree of faceting at lower ΔK values. As the water vapor pressure increased, a transition occurred to a combination of SBC and flat transgranular cracking. At a ΔK of 7 MPa√m, faceted cracking was observed first at 4 Pa, with increasing occurrence of faceted, SBC like features as the water vapor pressure decreased to UHV. Above 4 Pa, the crack morphology exhibited less indications of crystallographic cracking which is consistent with prior investigations where hydrogen assisted cracking occurred along high-index planes in 2xxx-series Al.[13,100] At a higher ΔK of 9 MPa√m, no faceted cracking was observed at pressures greater than 0.5 Pa and only a small degree of SBC was seen at 0.5 Pa and UHV. At a ΔK of 5 MPa√m, SBC-like features were observed at 18 Pa with increasing severity as pressure decreases to UHV. These findings are consistent with the correlations between the optical fracture surface images (Figure 27) and the crack growth behavior (Figure 25). For example, the SEM images in Figure 29d, Figure 30d, and Figure 31d correspond to the growth rates and optical images in Figure 28 at a ΔK of 9, 7, and 5 MPa√m respectively. These images highlight that non-crystallographic, transgranular, and flat morphologies are observed at high ΔK (9 MPa√m). These features are similar to intersubgranular features observed by Gangloff et al. at high ΔK and H producing environments in the Al-Li-Cu alloy 2090.[69] At the onset of the TTR (ΔK = 7 MPa√m) facetted SBC-like features are present (Figure 30d) and past the TTR when the growth rate is stabilizing there is a mix of non-crystallographic and SBC-like features (Figure 31d).

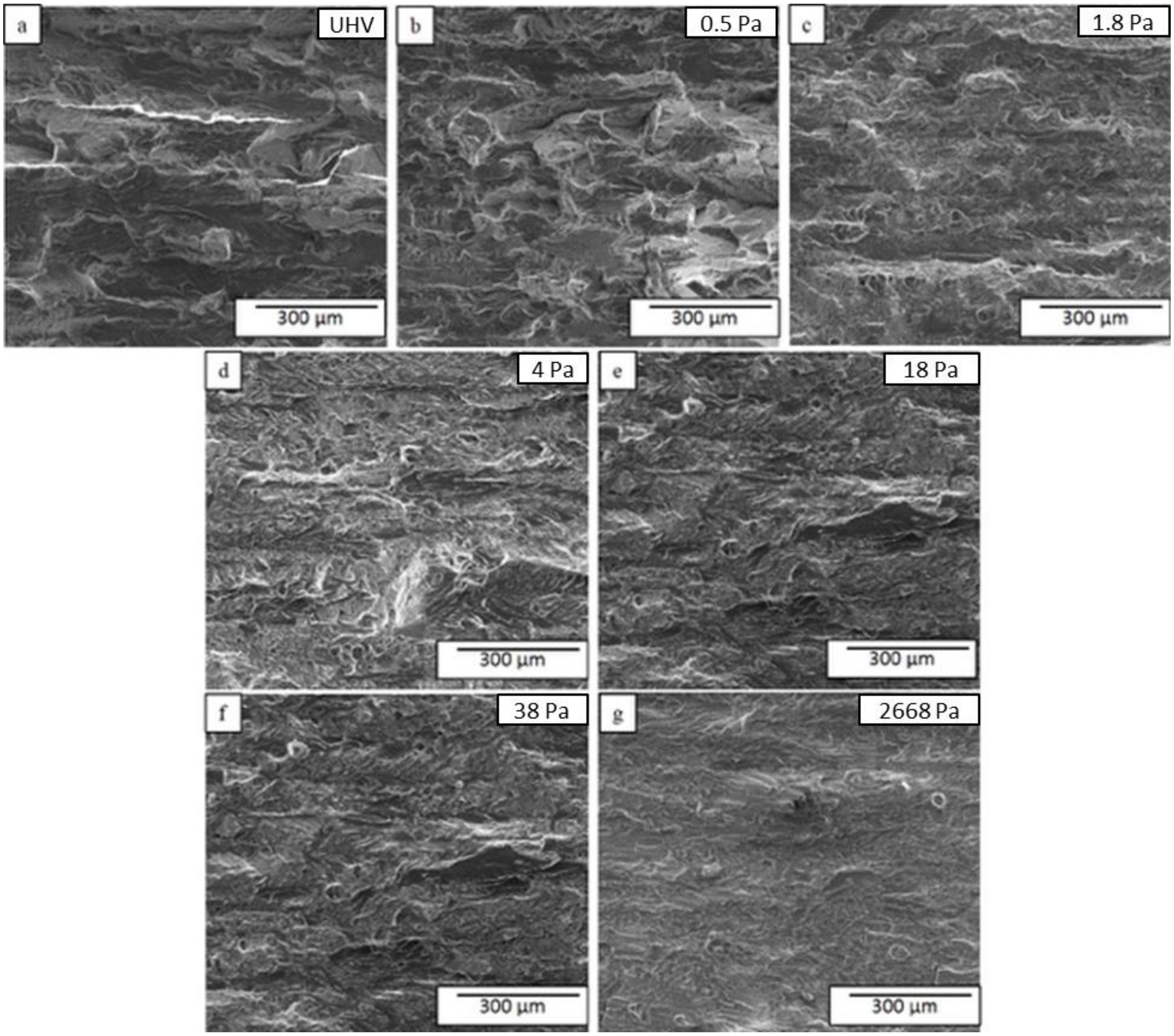

Figure 29: SEM images of the fatigue crack surface of 2199 tested at constant R = 0.5, f = 20 Hz and constant ΔK = 9 MPa√m for an L-T oriented specimen exposed to PH2O of: UHV (a), 0.5 Pa (b), 1.8 (c), 4 (d), 18 (e), 38 (f), and 2668 Pa (g). Crack growth is from left to right in each image. (Figure created by Jenny Jones)

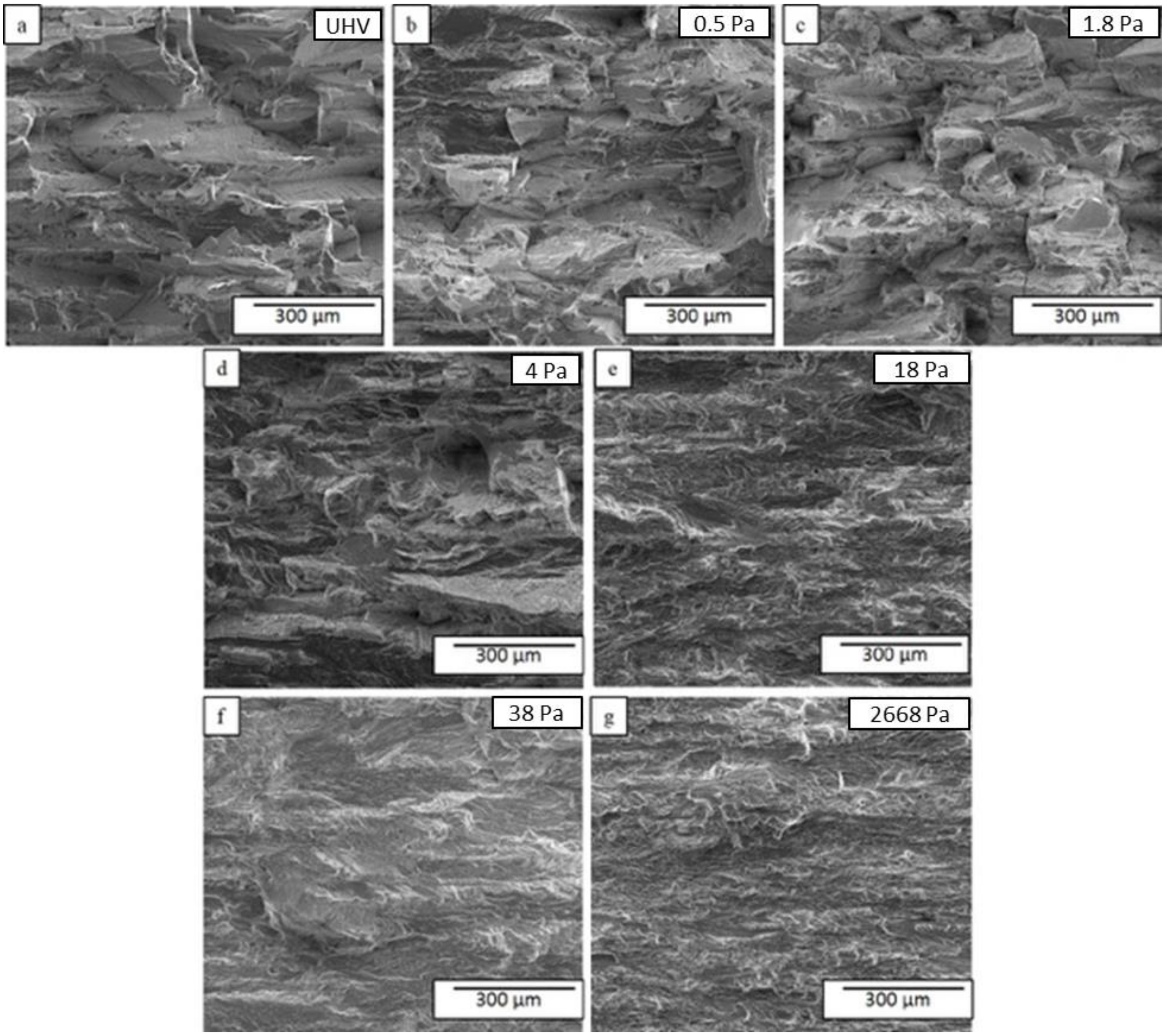

Figure 30: SEM images of the fatigue crack surface of 2199 tested at constant R = 0.5, f = 20 Hz and constant ΔK = 7 MPa√m for an L-T oriented specimen exposed to PH2O of: UHV (a), 0.5 Pa (b), 1.8 (c), 4 (d), 18 (e), 38 (f), and 2668 Pa (g). Crack growth is from left to right in each image. (Figure created by Jenny Jones)

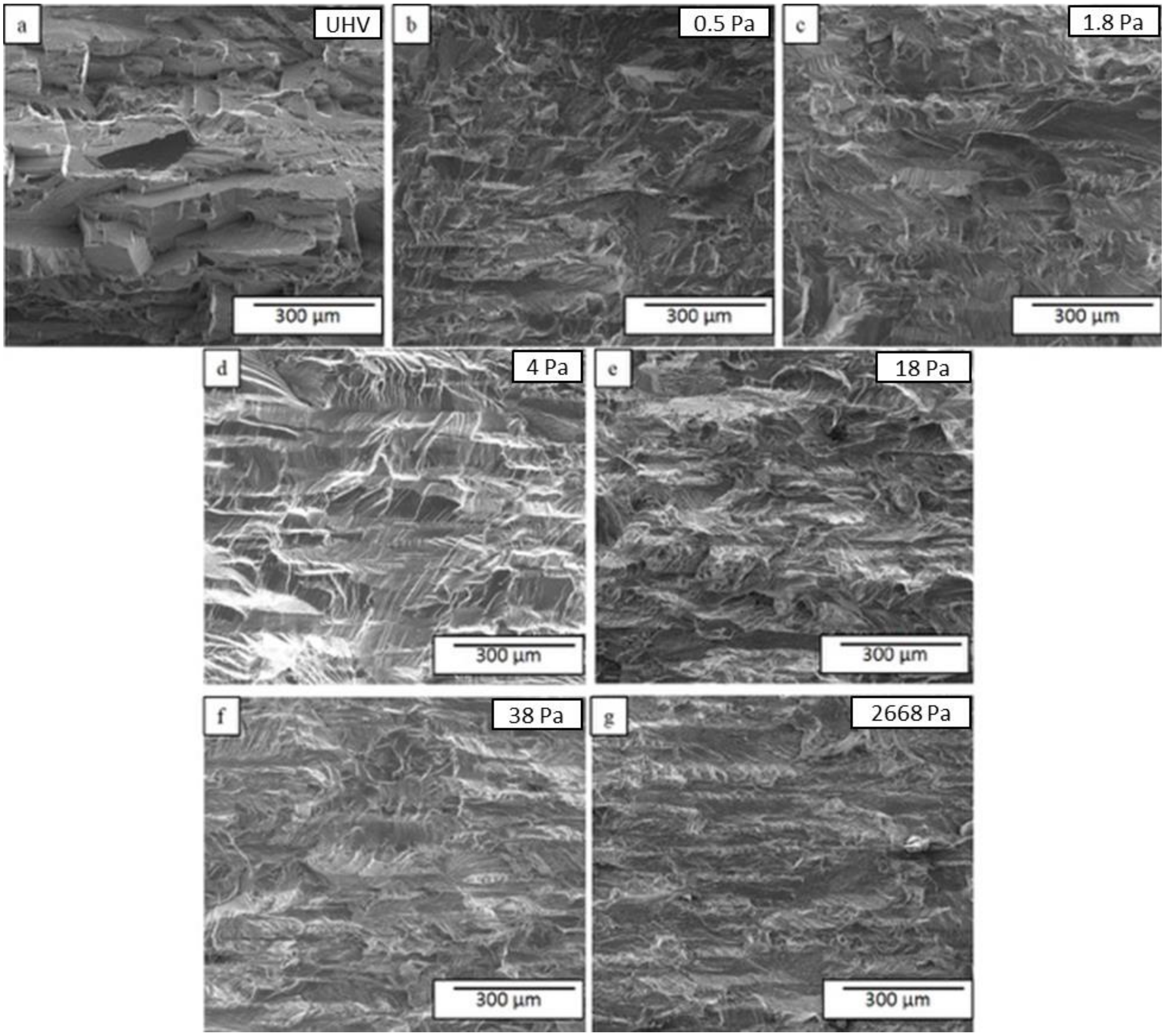

Figure 31: SEM images of the fatigue crack surface of 2199 tested at constant R = 0.5, f = 20 Hz and constant ΔK = 5 MPa√m for an L-T oriented specimen exposed to PH2O of: UHV (a), 0.5 Pa (b), 1.8 (c), 4 (d), 18 (e), 38 (f), and 2668 Pa (g). Crack growth is from left to right in each image (Figure created by Jenny Jones)

4.3.4 Effect of temperature on fatigue crack growth rates versus ΔK at variable P_{H2O}

Figure 32 shows the results of testing at constant P_{H2O} achieved either via (1) controlled ingress of water vapor into a vacuum system at 23 °C, or (2) low temperature conditions where the P_{H2O} is set via the equilibrium water vapor pressure above ice at a given temperature. These tests isolate the effect of temperature on the crack growth behavior of 2199. At and above -15 °C (e.g., 337 Pa at both 23 °C and -4 °C, and 165 Pa at both 23 °C and -15 °C), no temperature dependence is observed (Figure 32). However, at -30°C and below (note there were no tests conducted between -15 and -30°C to identify the T at which this divergence begins), there is a significant effect of temperature on the fatigue behavior. At -65 °C 0.5 Pa, there is again no temperature effect on cracking behavior, as vacuum level fatigue behavior exists for both temperatures. It is important to note that at -65 °C, the water vapor pressure is 0.5 Pa, which, at room temperature, was found to not have any environmental effect on cracking compared to UHV. Specifically, at -30 °C and -50 °C and ΔK of 9 MPa√m, there is roughly an order of magnitude difference in crack growth rate compared to room temperature testing. In fact, above a ΔK of ~7 MPa√m, both -30 °C and -50 °C produce vacuum like crack growth rates. As the stress intensities decrease below ΔK values of ~7 MPa√m, crack growth rates of both tests begin to converge with their room T counterparts. For testing at -50 °C, crack growth rates begin to again fall below those measured at room temperature between ΔK of 5 and 3 MPa√m. Inspection of the chamber water vapor pressure shows that the bulk environment water vapor pressure fell below 1 Pa near 5 MPa√m and hovered near one until the small decrease in crack growth rate at a ΔK of 3.4 MPa√m, at which point, the water vapor pressure rose and stayed above 1 for the remainder of testing. Outside of the ΔK of 5 to 3.4 MPa√m, the average water vapor pressure in the chamber was 2.4 Pa, while it was 1.1 Pa within the ΔK of 5 to 3.4 MPa√m. While the assumption was made during testing that the crack tip water vapor pressure would remain at equilibrium even under slight fluctuations in the bulk chamber water vapor pressure, evidence suggests that when the environment drops below ~1 Pa this may no longer be the case. In all other testing at -30 °C, no small fluctuations in the bulk environment water vapor pressure were found to influence crack growth kinetics. This data shows that at low temperatures and water vapor pressures, the crack growth rate is slowed significantly, independently of water pressure, however it does not appear to have an effect until temperatures drop below -15 °C and continues to have an effect until water vapor pressures drop below an environmentally significant concentration.

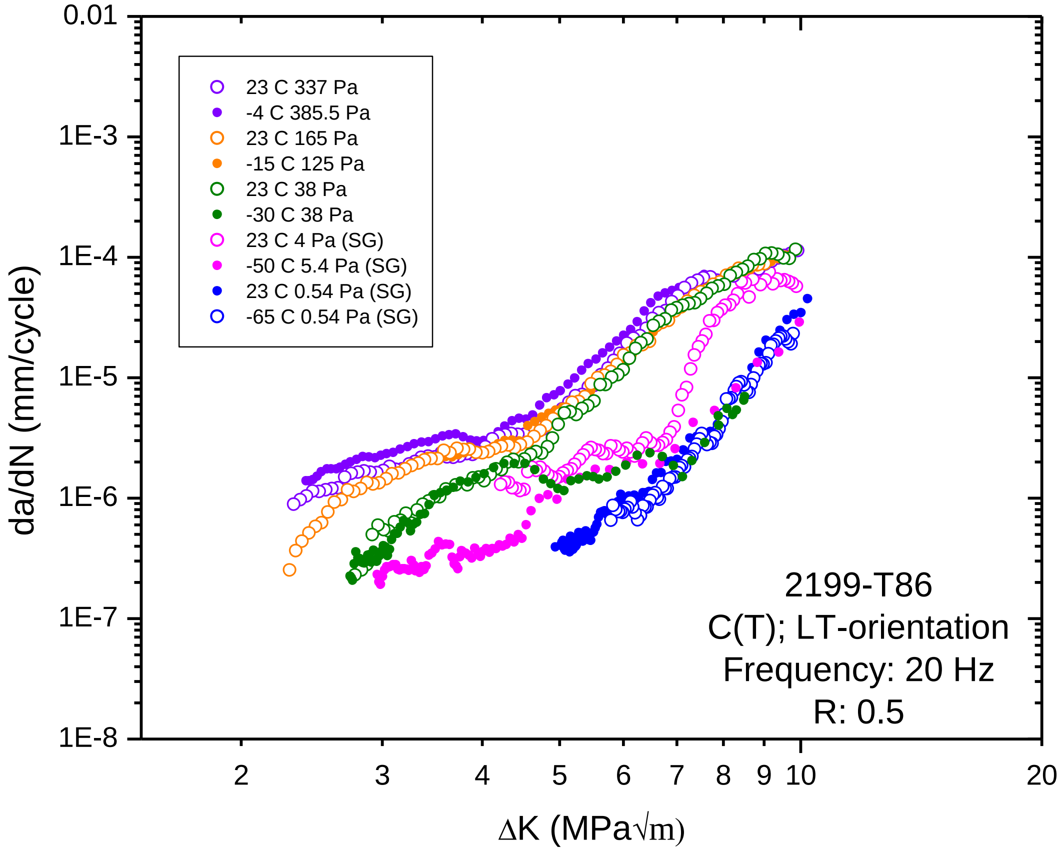

Figure 32: Crack growth rates versus ΔK at constant R of 0.5, f of 20 Hz for 2199 with varying temperature from 23 ◦C to -65 ◦C. Side-grooved samples are indicated as (SG). 23 ◦C, 165 Pa, plot is a combination of side-grooved (above ΔK = 4.8 MPa√m) and standard thickness (below ΔK = 4.8 MPa√m)

4.4 Discussion

The fatigue behavior gathered for 2199 over a wide range of ΔK, P_{H2O}, and temperatures demonstrate that 2199 exhibits many similar trends as those previously reported for 7075. Specifically, there is strong dependence of the crack growth kinetics on the P_{H2O}, the dependence of the da/dN on the P_{H2O} reasonably aligns with mechanism-based models of the rate limiting steps, the TTR behavior is observed and corresponds with regions of enhanced crack roughness. Additionally, the crack growth kinetics are strongly temperature dependent (despite constant P_{H2O}) below -30 ˚C until -65 ˚C where environmental cracking is believed to be eliminated. These data provide the basis to answer several important questions. First, does current data support the extension of the transport limitation-based hypothesis (developed for 7075) to explain the TTR behavior in 2199. Second, what are the subtle differences in the TTR behavior between 7075 and 2199, and can these differences be understood based on the known microstructure induced changes in the slip behavior and/or crack path. Third, 2199 demonstrated temperature dependent behavior as was also observed in 7075, does this provide insights into the possible underlying mechanisms for temperature dependent behavior in aluminum alloys.

4.4.1 Transport Limitation Induced TTR in 2199

The current 2199 fatigue behavior is distinct from the 7075 growth rates reported in Figure 24 (for high humidity and UHV) and also from 7075 kinetics previously reported at intermediate levels of P_{H2O}. Despite the inherent differences in the nature of the crack path and the corresponding crack wake between 7075 and 2199, the fractography presented in Figure 27 and Figure 28 demonstrate that similarities exist in the underlying causes for the TTR in these two alloys. This section will determine the extent to which the transport limited hypothesis can be applied to 2199.

Three primary aspects of the data support the applicability of the transport limited hypothesis to 2199. First, 2199 exhibits a TTR behavior with a sharp decrease, followed by a spike in the growth rates with decreasing ΔK. Second the behavior only occurs at intermediate ΔK and P_{H2O} in both alloys. This is demonstrated in Figure 26 where the TTR behavior is observed at P_{H2O}

levels where the crack growth is proposed to be transport-controlled. This is logical given that in the lower plateau the contribution of the environment to cracking is eliminated due to a lack of sufficient water molecules to support embrittlement. On the upper plateau, there is sufficient bulk water vapor to enable a saturation of water molecules at the crack tip, thus the behavior is not dependent on molecular transport. These data strongly suggest that the TTR only occurs in regions water vapor pressures that environmental cracking is limited by the transport mechanism.

Third, the fracture surface features present in 7075 and 2199 are similar and provide key insights on the mechanism responsible for the FCGR behavior. Analysis of the fracture surface at 4 Pa allows insights to be made on the mechanism by which the TTR develops. According to the transport limited hypothesis, as the roughness begins to develop, transport to the crack tip is inhibited along the crack path due to increased roughness, changing the flow path morphology, which Knudsen flow based molecular transport models have shown to affect the flow behavior.[15,16,31,36] While this will affect the transport of water vapor down the crack path, there will remain a clear path for transport of water vapor from the sample flanks, as they are very near the bulk environment. This suggests that more water molecules would reach the edges of the sample compared to the center, increasing the environmental contribution in these areas. This is exactly what is observed in Figure 27c, d, and Figure 28, where samples that exhibited the TTR behavior (1.8 and 4 Pa) demonstrate a transition to a smoother transgranular cracking that progresses from the sides of the sample due to enhanced environmental contribution. This is consistent with a fatigue cracking morphology that is largely flat and transgranular at these ΔK and at high exposure parameters (Figure 27e-f). While the crack path evolution was not tracked, this crack progression is supported by a companion study on 7075 where loading sequence induced fracture surface markers tracked the evolution of an irregular crack front during the TTR.[28] Due to the enhanced growth kinetics at the crack flanks, an irregular crack front develops, and the stress intensity at the center of this crack increases dramatically. This variation of driving force along the crack front leads to the rapid extension of the center of the crack to equilibrate the driving force; this behavior is responsible for the rapid increase in growth rates observed after the minima in the TTR.[28,64,101,102] *In toto*, these findings are consistent with the transport limited environmental cracking induced by crack wake roughness hypothesis that has been suggested to explain the TTR behavior in 7075.[28]

4.4.2 Alloy Specific TTR Behavior in 2199

While there were many similarities in the TTR behavior between 7075 and 2199, there were also several differences to be addressed. Specifically, the TTR onset occurred at a higher ΔK in 2199 (8.5 MPa√m) compared to 7075 (5.5 MPa√m), different water vapor pressures were affected (1.8 Pa and 4 Pa in 2199 versus 0.2 Pa and 0.5 Pa in 7075), and the magnitude of the drop and subsequent spike were less severe in 2199. Differences in the fracture surface were also observed where the roughened surface occupied a greater area in 2199 compared to 7075.

First, 2199 has a larger intrinsic resistance to fatigue, independent of environmental cracking processes. This can be seen by comparing the growth rates of the two alloys at UHV in Figure 24. As such for a constant ΔK and H concentration in the process zone, a lower growth rate may be expected in 2199. This increased cracking resistance has been postulated to be due to a high degree of slip reversibility present due to shearable precipitates present in 2199.[93,95,100] Secondly, it is possible that for a constant bulk P_{H2O} that there are differences in the extent of H adsorbed at the crack tip for the two alloys. Such differences may arise from the variations in the crack wake morphology as the extent of roughness can impede water vapor transport. This is supported by fractography (Figure 28) that demonstrates that the onset of the TTR behavior corresponds with the ΔK at which there is a change in fracture surface roughness. Other factors such as the aluminum-water vapor reaction rates, differences in film stabilities, and differences in diffusion rate of H in the aluminum could all potentially play a role in the in determining the local crack tip H concentration and therefore, TTR behavior differences in this alloy. Finally, extrinsic toughening due to either crack path tortuosity or crack closure could impact the effective driving force in the TTR region. These could lead to a situation where the nominal continuum driving force is identical between the alloys, but the true crack tip driving force is lower due to one or both of these factors. The current study addressed crack closure by applying the ACR closure correction, however, crack path tortuosity was seen in several tests and could be an unaccounted-for factor.

Fourth, when examining the fracture surfaces of the two different alloys, Figure 27c and d show that in 2199, the roughness encompasses a greater area of the sample and appears to recede towards the middle at a slower rate compared to 7075[28]. Functionally, this results in a less irregular crack front, thus a less extreme differentiation of the driving force (ΔK) along the crack front, which is consistent with the less severe spike in growth rate in 2199. The more modest development of the irregular crack front in 2199 is reasonably understood based on the relative differences between the growth rates expected for environmentally enhanced (at the surface) and environmentally starved (center) regions of the samples. To quantitatively compare this behavior for the two alloys systems, it is useful to look at P_{H2O} conditions that exhibited the most severe TTR behavior (4 Pa for 2199 and 0.2 Pa for 7075). The growth rates at ΔK directly preceding the onset of the TTR behavior (8.5 MPa√m for 2199 and 5.5 MPa√m for 7075[28]), provides a proxy for the growth rates at the crack flanks that have full access to the environment. The magnitude of the difference between this rate and the UHV rate (as a proxy for the rate at the center of the sample) at that same ΔK will give an indication of the expected level of crack irregularity that will develop. There is a 10-fold difference between the 7075 at 0.2 Pa and UHV at a ΔK of 5.5 MPa√m whereas there is only a 5-fold difference between 2199 growth rates at 4 Pa at a ΔK of 8.5 MPa√m. These data support expectation of a more irregular crack front in the 7075 system during the TTR, thus reasonably explain the more severe dip and observed spike.

4.4.3 Effect of temperature on crack growth

The 2199 results clearly demonstrate that for a constant P_{H2O} there is temperature dependent behavior observed at -30 °C and below. A great deal of research has been performed on the mechanical behavior of Al-Li alloys at low temperatures;[57,76,103–108] with the majority performed at cryogenic temperature (< -196 °C). The yield strength,[74,106,107] fracture toughness,[76,104–107] and fatigue performance[57,76] all improved at low temperatures. The improvement in fatigue and fracture resistance at cryogenic temperatures are attributed to delamination that results in shifting the stress state of the material from plane strain to plane stress, which raises the fracture toughness of the material.[76,104–107] Due to the very low temperatures these studies were performed at, the applicability of these cryogenic studies to the current work at more moderately low temperatures is uncertain. One study at moderately low temperatures by Goma et al., found improved fatigue behavior of 2099 at -30 °C [57], which was attributed to a reduction in environmental cracking.[57]

Previously work on 7075 identified seven mechanisms by which aluminum fatigue behavior could be improved at low temperatures. (1) An extrinsic strengthening mechanism such as crack closure could affect the effective stress intensity applied during testing. The intrinsic toughening of the material could be increased via either (2) changes in dislocation structures due to elimination of cross-slip and other thermally activated processes being deactivated at low temperatures, or (3) due to increases in yield strength at lower temperatures. The environmental process could be affected via (4) surface reaction kinetics, (5) the diffusion rate of H to the process zone, (6) transport of water vapor to the crack tip, or (7) H-dislocation interactions.

The rigor of each of these proposed mechanisms need to be evaluated in order to understand if they are responsible for the reduction of FCGR at low temperatures in 2199. At a high R of 0.5, closure effects are mitigated, and the current data has been closure corrected using ACR. These two factors make it unlikely that crack closure is responsible for the retardation in crack growth rate at low temperatures. Intrinsic toughening due to dislocation structure changes,[109–112] surface reaction of H_2O and absorption of H into the material,[36,40] as well as diffusion of H to the process zone[40,51] have all been shown to have an Arrhenius relationship with respect to temperature. This is not consistent with the results of this study; specifically, the fatigue behavior is temperature independent above -15 °C and at -65 °C. Yield strength has been shown to increase in Al-Li alloys at low temperatures,[74,106,107] this would impact the CTOD which is a commonly used metric for fatigue crack driving force. Using reported low temperature (-196 °C) values of E and σ_{ys} for an Al-Li alloy (2090) to calculate CTOD (CTOD = $0.6*K_{max}^2/ (2\sigma_{ys}*E)$) demonstrated that the decrease in temperature would only decrease the CTOD by 7.6%. Such a reduction would be an upper-bound given that the current experiments were performed at higher temperatures, even so this is not a sufficiently large increase to account for the observed decrease in growth rates. Finally, the inherent rate of transport of water vapor to the crack mouth was previously found to not be greatly affected by temperature.[17]

In the study of low temperature effects of cracking on 7075, it was suggested that temperature induced changes in crack wake roughness morphology could slow the transport process. This effectively limits hydrogen embrittlement and thus could be responsible for the observed deviations in growth behavior at different temperatures (but constant P_{H2O}).[5] However, several aspects of the current data suggestion that this is not the source of the temperature dependent deviations in 2199. First, the fracture surfaces of the -30°C and 23°C at 38 Pa samples in Figure 33 do not show substantial differences. The fracture surface at 23 °C shows a relatively flat, uniform crack wake surface with a small region of roughened surface between ΔK of 7 and 9 MPa√m. At -30 °C the crack surface is relatively uniform with a small region of roughened surface between 5 and 7 MPa√m. Second, the nature of the temperature dependent growth kinetics is fundamentally different between 7075 and 2199. Specifically, in 7075 the growth rates were similar at high ΔK, and differences arose due to varying onsets of TTR behavior as the ΔK decreased. Conversely, for 2199 the low temperature growth rates begin substantially lower and converge with the 23C behavior at lower ΔK. These findings strongly suggest that crack wake roughness induced changes in molecular transport are not responsible for the temperature dependent growth kinetics at a constant P_{H2O}.

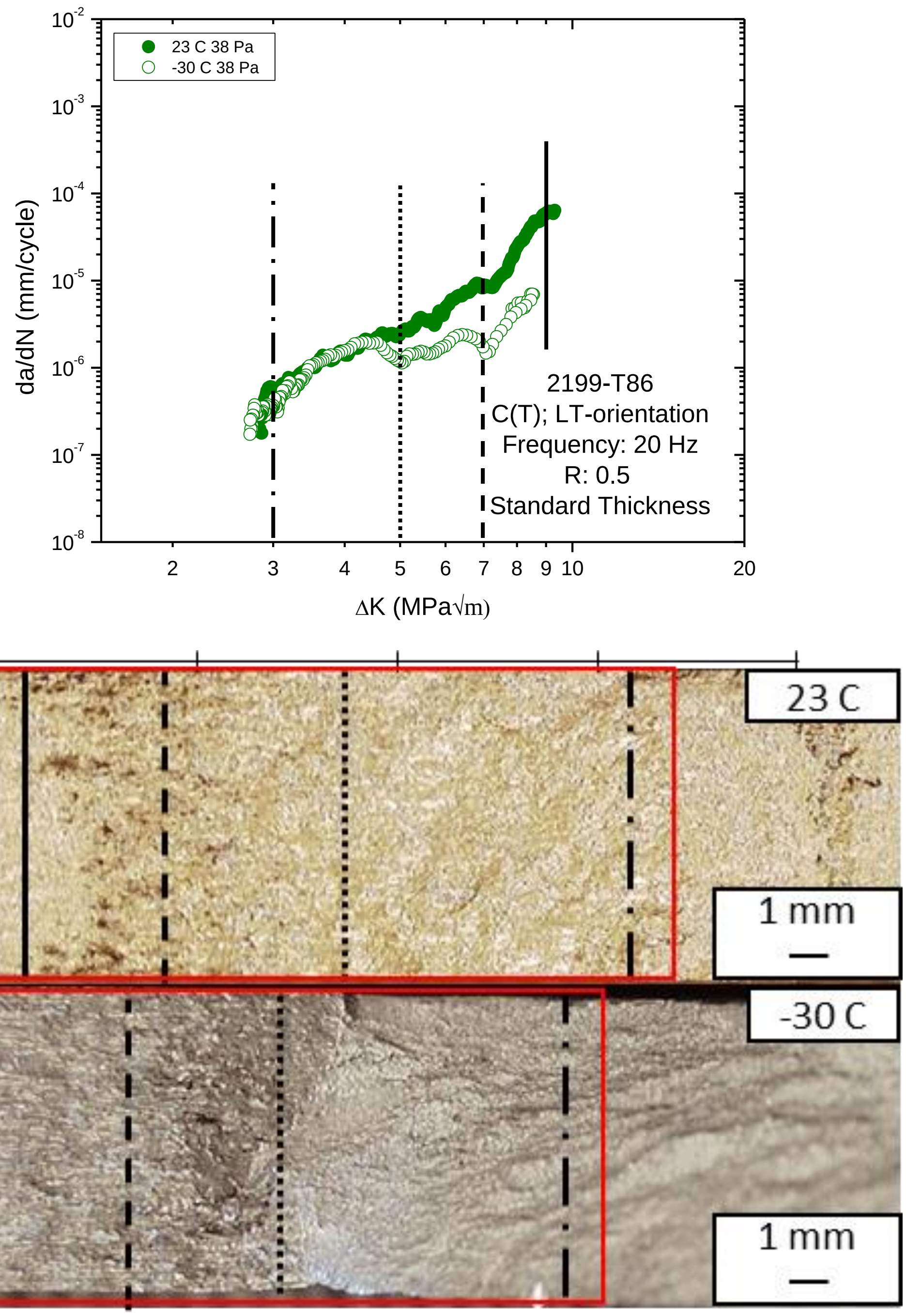

Figure 33: Crack growth rates versus ΔK at constant R of 0.5, f of 20 Hz and standard thickness for 2199 at 38 Pa for both 23 ◦C and -30 ◦C. Optical fractography of both 23 ◦C (a) and -30 ◦C (b) are shown as well. Red boxes indicate the area cracked during the K- shed. Black lines locate the crack position at ΔK of 9 (solid), 7 (dashed) 5 (dotted), and 3 (dash-dot) MPa√m on both the fracture surfaces and on the growth rate graph.

The remaining potential mechanism responsible for the decrease in growth rates at low temperatures is a change in the H-dislocation interactions at low temperatures. Coupled hydrogen and dislocation interactions models such as HELP, AIDE, HEDE, among others, serve as a promising approach to explaining FCGR changes with lowering temperature. While a full investigation is outside of the scope of the current study, the preceding discussion suggests H-dislocation interactions are in some way responsible for the observed temperature dependent behavior. Ongoing work is applying modern characterization techniques [48,113–115] to probe difference in the crack wake dislocation structure evolution to provide insight into this temperature dependent phenomenon.

A recent study on the environmental fatigue of 7075 at low temperatures in UHV environment showed that as the temperature decreased, the FCGR decreased.[59] This proves that at least some portion of the decrease in FCGR at low temperatures previously observed for 7075 is independent of water vapor pressure. This is in disagreement with this study as the lack of an Arrhenius relationship at -15 °C and no effect of temperature below the critical water vapor pressure for environmental cracking at -65 °C suggest that environmental factors are controlling the decrease in growth rate at low temperatures. While it is certainly possible the different alloys have different mechanisms controlling this behavior, it suggests that other factors could be at play. The recent experiments in 7075 had a more sophisticated experimental equipment and were able to control pressure and temperature independently of each other. Further study of 2199 in a similar setup should be explored in order to ensure that the current experimental setup was able to properly capture the low temperature behavior.

4.5 Conclusions

Environmental fatigue testing of 2199 in high altitude environments established over a wide range of ΔK was performed. This testing established the following conclusions regarding the effect of low water vapor pressure and low temperature on the fatigue crack growth rates.

- Reduction of P_{H2O} at 23 °C resulted in a systematic reduction of crack growth rates, resulting from a reduction in H needed for the HEE process. However, above 165 Pa, changes in P_{H2O} do not result in increased crack growth rates, reinforcing Wei's early finding that the environmental contribution reaches a saturation point. At 0.5 Pa FCGR matched those at UHV, indicating that at these low pressures, there is no longer any environmental contribution to cracking.
- A precipitous drop in crack growth rates at low water vapor pressures, followed by an increase in crack growth rates with decreasing ΔK has been termed the threshold transition region. This behavior has been suggested to be due to a rough crack wake impeding transport of water molecules to the crack tip, decreasing the growth rate. This is followed by preferential cracking from the side, creating an irregular crack front that rapidly increases in length, resulting in the increase in growth rates. The effect of the TTR is less extensive in 2199 compared to 7075.
- Low temperature testing showed that decreasing the temperature had no effect on growth kinetics down to -15 °C. Between -30 °C and -50 °C decreased crack rates were observed at these lower temperatures. When temperature was lowered to -65 °C 0.5 Pa, temperature again had no effect on crack behavior indicating that temperature is solely affecting the H-embrittlement process. This behavior is suggested to be due to dislocation

interactions with H changing as temperature decreased though no work was able to be performed to evaluate this in this study.

Chapter 5 – Incorporation of High-Altitude Environmental Effects in the LEFM-based Modeling of Aluminum Alloy 7075

Note: Work on this chapter culminated in the publication of journal article entitled *Incorporation of high-altitude environmental effects in the linear elastic fracture mechanics-based modeling of aluminum alloy 7075,* in the journal Fatigue and Fracture of Engineering Materials & Structures in 2022.

5.1 Introduction:

5.1.1 Overview of Current Approaches to Fatigue Life Estimates

Aluminum alloys are heavily used in aerospace applications where cyclic loading induced fatigue cracking is a primary failure mode.[116,117] Linear elastic fracture mechanics (LEFM) models have been widely applied to inform damage tolerant-based structural integrity management strategies in airframe structural components.[22,118–120] In this paradigm a flaw is assumed to exist in the structural component, cyclic loads induce a driving force for sub-critical crack extension which lengthens the crack. The crack progresses according to a fracture mechanics-based relationship between the crack tip driving force (stress intensity range, ΔK) and the crack growth kinetics (da/dN) until some failure criteria (e.g., exceedance of the fracture toughness, net-section yield, etc.). Several LEFM-based software models (e.g., NASGRO, AFGROW, DARWIN, BEASY, etc.)[121–123] exist which will integrate the da/dN vs. ΔK relationship to predict the crack extension as a function of applied loading cycles. The damage tolerant approach to structural management applies regular inspections in order to find and repair/replace cracked components before rapid crack growth and/or final fracture occurs.[118] This approach relies on accurate loading profiles, an assumed initial flaw size, rigorous stress intensity solutions, and assumes that fracture mechanics similitude (e.g., constant da/dN for a given ΔK) is maintained between laboratory samples and in-service components.

5.1.2 Current Growth Rates Being Applied in Fatigue Life Models

There is an extensive database of fatigue crack growth rates (FCGR; da/dN) versus stress intensity range relationships for alloys used in airframe structures; such data is typically generated in ambient laboratory conditions. However, aluminum alloys (and other structural alloys)[109,124,125] have drastically slower FCGR behavior at low temperature and low water vapor pressure environments.[5,10,21,11,13–16,18–20] Such environments are pertinent to high-altitude operation, where a significant portion of loading of can occur for airframe structural components.[5,21] The phenomenological and mechanistic underpinnings of the low moisture environment effect on aerospace aluminum alloys fatigue cracking behavior has been extensively studied.[5,10,33–40,42,43,13,16,27–32] It is understood that in moist air, the environmental cracking contribution is governed by hydrogen environment embrittlement.[15,35,44–46] Water molecules from the bulk environment travel through the crack wake channel to the freshly exposed aluminum at the crack tip. This water reacts with the aluminum, producing atomic hydrogen which is then adsorbed and diffuses to the crack tip process zone to embrittle the material. Typically, the FCGR data used in LEFM based models (that underpin structural integrity management) are obtained in lab air environments; as such the results can be overly conservative and not rigorously relevant to in-service conditions. While these estimates are conservative, they increase the inspection burden, which can be at a significant financial cost and limit airframe availability. In order to improve future modeling efforts by incorporating accurate in-service environments into the LEFM models it is necessary to have (1) a coupled load-environment spectrum that accurately captures the in-service conditions, (2) rigorous environment specific da/dN vs. ΔK relationships, and (3) a software interface capable of selecting environment specific growth rates for each integration step.

5.1.3 Required Components for LEFM Models

Regarding (1), generalized loading spectra have been reported,[126] with some reporting a coupled load-environment spectrum (e.g., ENSTAFF[26]). While generalized loading spectra cannot be applied for estimating fatigue life in-service, they provide a method of comparing results in a realistic loading framework. Furthermore, modern sensors enable straightforward monitoring of these relevant parameters to obtain such spectra. Concerning (2), recent research on aerospace Al alloys has generated crack growth rate database for low water vapor pressure and/or low temperature environments relevant to high altitudes.[5,15,60,103,127–130,16,21,28,30,31,42,45,54] While there are testing protocol challenges to ensure similitude is not compromised by crack wake morphology induced complexities. [10,13,28] mechanistically informed assumptions to obtain crack growth kinetics fit for use in LEFM models have been proposed.[10,28,54,131] As such, high altitude environment relevant FCGR data exists for use in LEFM based fatigue life modeling of AA7075-T651 generated according to ASTM E647.[58] Integration of these data in damage tolerant approaches is possible, provided that the following are available: an initial flaw size, a coupled load-environment spectrum, and a modeling program that can incorporate both environmental and mechanical variables.

Like many similar LEFM-based fatigue crack growth prediction codes, AFGROW has a variety of pre-loaded (or user defined) stress intensity solutions for common geometries and allows the user to input initial crack size, select various loading modes, and define different loading spectrums. Custom variable amplitude load spectra can be input via "Spectrum Manager", a software module designed to easily interface with AFGROW. Furthermore, there is a wide variety of pre-loaded crack growth laws or a tabular look-up function can be used to input custom da/dN vs. ΔK relationships. The inputs above are used in a numerical integration scheme to calculate the crack extension per some user defined cycle increment, this process is repeated until a user defined criterion is meet (e.g., a given crack size, transition to a through-crack, net section yielding, exceedance of the fracture toughness, etc.). The functionality described above has always enabled input of environment specific growth kinetics (and even provides pre-loaded environmental growth rates), however there was previously no automated way to vary the growth law to reflect specific environmental conditions at different points of the loading spectrum.[4] Recently, the "Spectrum Manager" module was modified to enable input of a coupled environment and loading spectra. Specifically, this enhancement enables (1) each load to be assigned an environmental tag, and (2) the input of multiple da/dN vs. ΔK relationships that can be harvested to gather a growth rate that is specific to the calculated ΔK for that load and the environment identified by the environmental tag. This important modification enables modeling of complicated environmental-loading spectrum to determine the magnitude of environmental impact on the fatigue crack propagation life.

5.1.4 Research Goals

Literature has clearly established the strong beneficial impact of high-altitude environments on the da/dN vs. ΔK behavior in 7xxx-Al alloys. However, quantitative evaluation of the effect of these environments on modeling the crack propagation life is limited. Such life predictions will dictate inspection intervals, thus are more relevant to the structural integrity community than simple da/dN vs. ΔK relationships. The overarching goal of the current study is to exercise the AFGROW "Spectrum Manager" module to evaluate the impact of variations in loading environment on the LEFM-predicted crack propagation life. Critically, the goal of this study is not to validate the predictions (such work is being performed in a companion study) rather to evaluate the potential impact and the sensitivities of the predicted life to various load-environment combinations. To do so various coupled environment-loading spectrum with gradually increasing complexity will be evaluated using low water vapor da/dN vs. ΔK relationships. Specific conditions will include (1) constant stress, constant environment, (2) a simple variable stress, variable environment spectrum, (3) a generalized coupled load-environmental spectrum that aims to generally describe in-service airframe conditions (based on ENSTAFF), and (4) an in-service coupled load-environment spectrum for specific airplane models. The results of these models will be discussed in the context of their potential impact of structural integrity management. Furthermore, the remaining technical knowledge gaps and areas for validation will be identified.

5.2 Experimental Methods

5.2.1 High Altitude da/dN vs. ΔK Relationships

Material and environment specific da/dN vs. ΔK inputs for AA 7075-T651 are harvested from prior work and a brief review of the data generation protocol is provided.[13,27,54] Testing was performed on compact tension (CT) samples at a constant stress ratio (R) of 0.5 and frequency (f) of 20 hz using a K-shed protocol following the formula $\Delta K=\Delta K_o \exp[C(a-a_o)]$ with ΔK_o = 14.85 MPa√m, a_o=13.7 mm C=0.08 mm^{-1}.[13,58] It is important to note that only a single R value was tested, as such R-dependent closure and K_{max}-dependent fatigue behavior are not captured in the life predictions. This approach is justified based on (1) the scarcity of high-altitude environment FCGR data, (2) the fact that a large portion of crack extension life in components occurs for small cracks where closure is less potent so the relatively high R (0.5) will reasonably capture these growth rates,[132] and (3) the varying ΔK values associated with the variable amplitude spectrum are still useful to interrogate. Details on the environment control has been detailed in previous work. After the da/dN vs. ΔK curves were generated; thirty characteristic data points were selected (Figure 34) to serve as inputs to the tabular lookup function in AFGROW which are used as the environment specific growth kinetics needed for the modeling efforts. For example, when 38 Pa is referenced in the coupled load-environment spectrum, the light blue curve (Figure 34) is used to establish the da/dN value associated with the ΔK value calculated for a given stress from the spectrum, crack size, and crack geometry (thus K-solution).

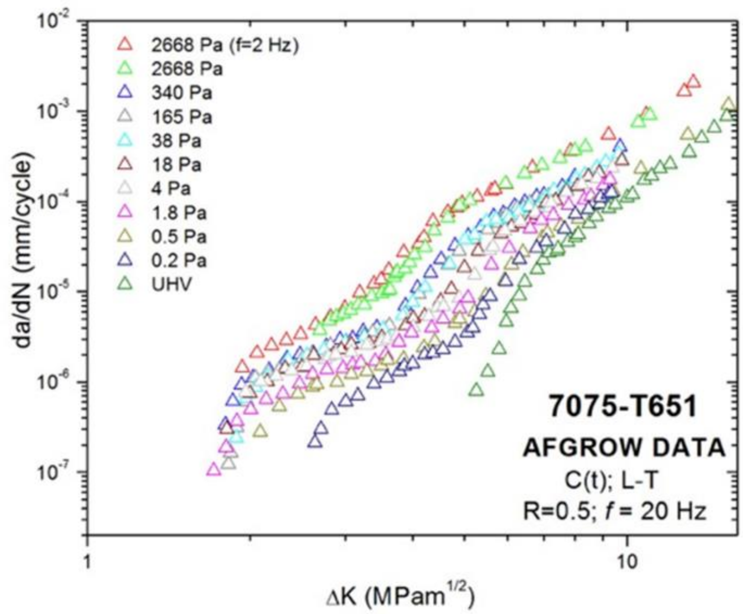

Figure 34: Experimental data truncated to 30 data points for application into AFGROW growth rate tabular input. Da/dN data was generated using K-shed loading protocol at an R=0.5 and a frequency at 20 Hz (unless otherwise noted)

Of note, the AFGROW interface allows the environmental condition to be tagged to some environmental parameter. For this study, temperature was used as the environmental tag as this is how ENSTAFF reported the environmental condition. Therefore, the water vapor pressure above ice at a given temperature is used to relate the data in Figure 34 to temperature values (Table 7). Critically, regardless of the temperature-based tracking approach within AFGROW, the da/dN vs. ΔK relationships used in the modeling are for a given water vapor pressure so the text and charts reflect this reality. Two additional considerations regarding the description of the environmental conditions should be noted. First, water vapor pressure is used to delineate the environment, however literature as well previous chapters in this dissertation have established that water vapor pressure over frequency (P_{H2O}/f) more rigorously describes the environmental severity parameter. Since all data in Figure 34 were established for a constant frequency (20 Hz), the P_{H2O} and P_{H2O}/f parameters are equally descriptive, as such the P_{H2O} is used for simplicity and consistency. Second, it is important to note that recent studies have demonstrated that at constant P_{H2O}/f, data for tests below -15°C exhibit slower growth than those at 23°C.[5,17,60] The mechanistic causes for this temperature induced breakdown in similitude are being investigated, but the fact that low P_{H2O}/f data at 23°C are faster than their low temperature counterparts suggest that the use of the 23°C data (e.g., Figure 34) are conservative.

Altitude (m)	T (°C)	$P_{H2O(-ICE)}$ (Pa)
0	15	≈1,500 @85% RH
1524	5	≈750 @85% RH
3048	-5	402
4572	-14	181
6096	-24	70
7620	-34	25
9144	-44	7
10,668	-54	2
12,192-18,288	-57	1

Table 7: The temperature of and water vapor pressures at altitudes relevant to airframe operation. The water vapor pressure for each temperature corresponds to the vapor pressure above ice for of the temperatures listed.

The da/dN curves generated at low water vapor pressure were loaded at a constant 20 Hz. As the loading frequency impacts the environmental parameter it needs to be noted that water vapor pressure alone is not a perfect proxy for the environmental contribution. It is recognized that this limits the direct quantitative applicability of the current predictions to service components, however this short-coming only reflects the accuracy of the environmental conditions. Since the goal of this paper is to exercise the LEFM model to determine the effect of coupled load-environments on crack propagation (not to develop quantitatively accurate life predictions), the subtle details of linking service environments to lab-testing environments does not compromise the validity of the results and conclusions.

5.2.2 Modeling Condition 1: Constant Stress, Constant Environments

For Condition 1, a constant stress and environment are applied throughout the duration of each test. A sample with a single corner crack at a hole, *a=250 µm, c=250µm,* was loaded cyclically at an R=0.5 in AFGROW until the flaw size reached 1.5 mm. This was repeated at various constant maximum stress levels ranging from 200-450 MPa (input via the stress multiplication factor (SMF) in AGRGROW) and in various constant environments from UHV to 2668 Pa

5.2.3 Modeling Conditions 2: Variable Stress, Variable Environment

Condition 2 applied a stress and environment which varied for each block of cycles (Table 8) This arbitrary loading spectrum was developed to simulate a changing environment during different parts of a loading cycle. In order to do this, Spectrum Manager was used to assign each stress with an environmental tag. This allows for an appropriate growth rate to be called for the duration of the loading block. One model was performed with all high humidity (e.g., 2668 Pa) FCGRs and compared to a model prediction that included variable low water pressure environments. The prediction preferences in AFGROW for modeling Condition 2 used a max growth increment of 5% and outputted the flaw size after each block of cycles. The failure conditions were K_{max} failure criteria (set to 29 MPa√m) and crack growth to free surface. The geometry of the specimen was a bar with a width (W) and thickness (T) of 7.62 mm containing a center semi-elliptic surface flaw with a and c both equal to 1 mm, shown in Figure 35.

Cycles	Max Stress	R	Constant Pressure	Variable Water Pressure
10,000	100 MPa	0.5	2668 Pa	0.54 Pa
5,000	50 MPa	0.1	2668 Pa	2668 Pa
15,000	150 MPa	0.5	2668 Pa	UHV
2,000	250 MPa	0.7	2668 Pa	4 Pa
300	300 MPa	0.1	2668 Pa	UHV

Table 8: Stress and environment spectrum for modeling Condition 1 for both high humidity and mixed environment conditions. FCGR for each water vapor pressure (shown in Figure 34) were then applied appropriately applied according to this table. This loading spectrum was repeated until crack growth reaches a free surface or K max for the material was exceeded

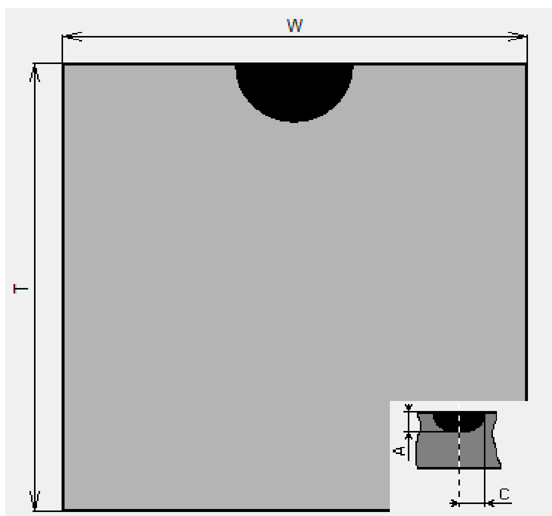

Figure 35: Initial specimen design for modeling conditions 3 and 6 is shown. A surface center elliptical flaw in a bar where the width (W) and length (L) are 7.62 mm for condition 3 and 100 mm for condition 6. The initial flaw has parameters A and C of 0.5 mm for both condition 3 and condition 6. (Definitions of A and C are shown)

5.2.4 Modeling Condition 3: ENSTAFF Generalized Load-Environment Spectrum

In order to develop a loading spectrum consistent with real world applications, the previously developed loading and environment spectrums FALSTAFF and ENSTAFF were used.[44,57] FALSTAFF provides a characteristic loading spectrum, consisting of 200 flights, based on the loads experienced by the wing of a generic fighter in service. ENSTAFF assigns a temperature to each of the load conditions described in the FALSTAFF spectrum. The water vapor pressure is established based on the water vapor pressure above ice at a given temperature, as shown in Table 7 for various relevant flight altitudes. Using Spectrum Manager, each load and temperature were assigned a da/dN vs. ΔK relationship at the appropriate water vapor pressure, as shown in Table 9. After this, two model iterations were conducted at various maximum stress values (50, 100, 150, 200, and 300 MPa), one where all loads were assigned high humidity growth rates, (referred to as high humidity) and another where growth rates were assigned to each load based on the ENSTAFF spectrum (referred to as realistic pressures). The prediction preferences for modeling Condition 3 were more stringent than the previous modeling condition. Cycle-by-cycle beta and Spectrum calculation was performed with an output every 0.02 mm. The failure conditions were K_{max} exceedance and crack growth to a free surface. The geometry of the specimen was a bar with a W and T of 7.62 mm containing a center semi-elliptic surface flaw with a and c equal to 0.5 mm shown in Figure 35.

Temperature (C)	Corresponding altitude	Corresponding water P_{H2O}	Actual P_{H2O} used
75	N/A	N/A	**2668 Pa**
50	N/A	N/A	**2668 Pa**
20	0 ft	1500 Pa	**2668 Pa**
-5	3048 m	402 Pa	**337 Pa**
-25	7620 m	70 Pa	**38 Pa**
-40	11,582 m	14 Pa	**18 Pa**

Table 9: Comparison of structure temperature and corresponding water vapor content with actual water vapor pressure FCGR utilized for ENSTAFF spectrum. This data was previously generated and shown in Figure 34

5.2.5 Modeling Condition 4: Boeing 707 Wing Station 360 Spectrum

A similar modeling approach was executed by SAFE Engineering where loading/environmental spectrum from a Boeing 707 Wing Station 360 Spectrum and a business jet were used. Using spectrum manager, the fatigue life using high altitude growth rates versus high humidity growth rates were compared. The spectrum is shown in Figure 36, including the temperatures used, which were correlated to a water vapor pressure using Table 7. The SMF was 129.35 MPa with a double corner crack at a hole where the thickness is 25.4 mm and the initial crack was 1.27 mm. Using a double corner crack in plate geometry with a W of 25.4 mm, T of 2.54 mm, and a hole diameter (D) of 3.81 mm. The initial flaw size is 1.27 mm in both the a and c crack directions.[133] Figure 37 shows the model inputs.

#	Segment	S_{max} (MPa)	S_{min} (MPa)	Cycles	Altitude (m)	Actual (◦C)	Binned (◦C)
1	TAKEOFF	-38.27	-71.02	3	0	15.02	23
2	FLAPS DOWN DEPARTURE	109.08	54.40	2	305	13.02	23
3	INIT CLIMB	118.04	79.78	3	914	9.07	23
4	FINAL CLIMB	112.39	76.40	3	5181	-18.65	-15
5	CRUISE	118.39	83.84	4	10363	-52.26	-15
6	CRUISE	128.25	73.91	2	10363	-52.26	-50
7	FINAL CLIMB	106.05	82.88	2	10591	-52.26	-50
8	CRUISE	106.94	71.36	7	10820	-54.21	-57
9	CRUISE	112.87	65.50	2	10820	-54.21	-57
10	FINAL CLIMB	92.26	69.57	2	10896	-56.21	-57
11	CRUISE	93.43	63.09	6	11582	-56.48	-57
12	CRUISE	98.74	57.71	2	11582	-56.48	-57
13	FINAL CLIMB	90.05	71.91	2	12039	-56.48	-50
14	CRUISE	87.57	62.95	4	12496	-56.48	-50
15	CRUISE	95.01	55.57	2	12496	-56.48	-37
16	INIT DESCENT	92.26	53.37	4	10058	-50.26	-37
17	CRUISE	78.95	54.19	3	7620	-34.48	-37
18	CRUISE	82.81	50.33	2	7620	-34.48	-37
19	CRUISE	91.29	62.88	3	7620	-34.48	-37
20	CRUISE	96.46	57.71	2	7620	-34.48	-37
21	CRUISE	121.28	83.50	4	7620	-34.48	-37
22	CRUISE	129.35	75.43	2	7620	-34.28	-50
23	FINAL CLIMB	111.84	80.05	3	8991	-42.37	-50
24	CRUISE	118.32	83.77	4	10363	-52.26	-50
25	CRUISE	128.18	73.91	2	10363	-52.26	-57
26	FINAL CLIMB	106.05	83.08	2	10591	-52.26	-57
27	CRUISE	107.15	71.23	7	10820	-54.21	-57
28	CRUISE	112.87	65.50	2	10820	-54.21	-57
29	FINAL CLIMB	92.46	69.78	2	11201	-56.21	-57
30	CRUISE	92.26	64.88	4	11582	-56.48	-57
31	CRUISE	99.15	57.99	2	11582	-56.48	-57
32	INIT DESCENT	93.50	69.02	2	5791	-22.59	-30
33	FINAL DESCENT	106.05	78.67	3	914	9.07	23
34	FLAPS DOWN APPROACH	119.90	75.78	2	305	13.02	23
35	ROLL MANEUVER	99.36	92.32	40	305	13.02	23
36	LANDING ROLLOUT	-24.41	-45.30	5	0	15.02	23
37	GAG	129.35	-71.02	1	Various	-34.28	-30

Figure 36: Boeing 707 Load-Environment spectrum.

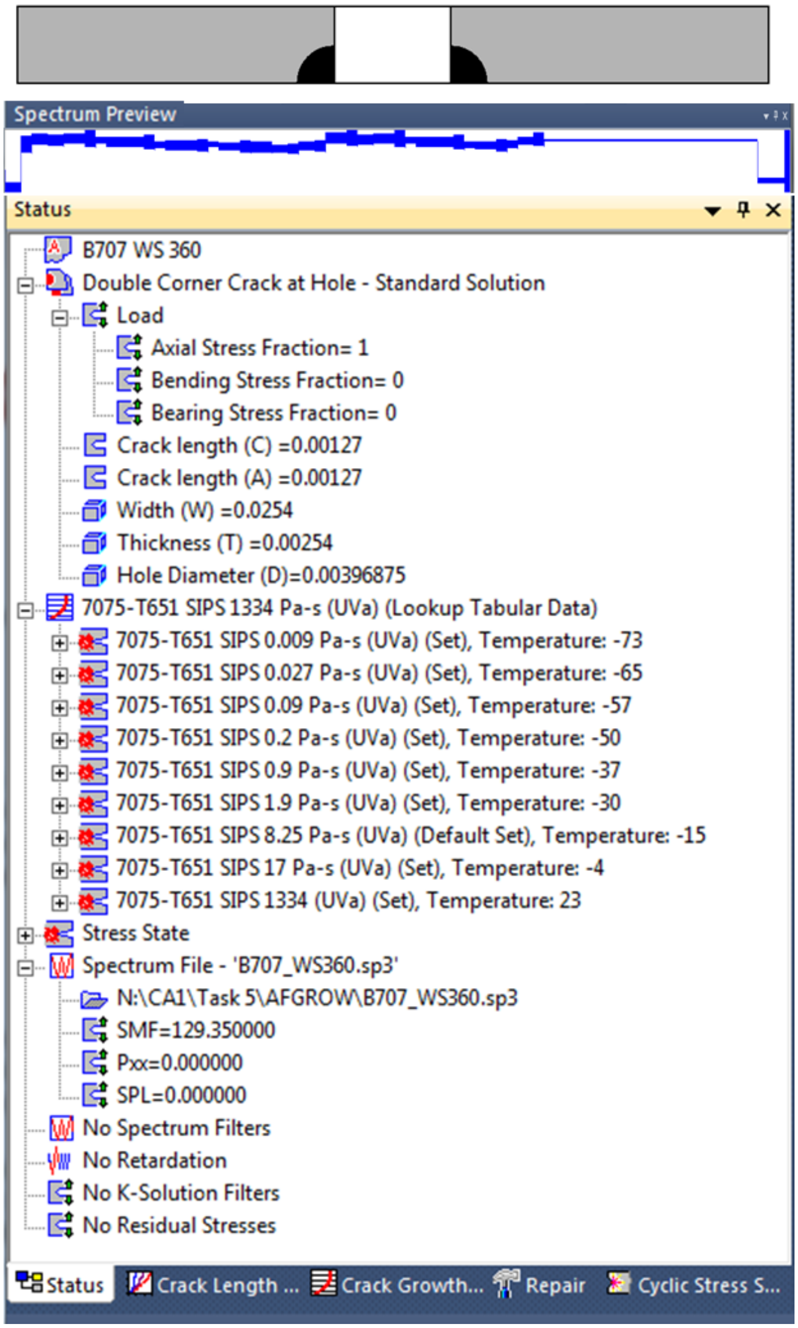

Figure 37: AFGROW model for Boeing 707 and business jet crack life predictions. From top to bottom, double corner crack at holes specimen design, spectrum preview, model inputs.

5.2.6 Modeling Condition 5: Commercial Jet Wing Spectrum

Modeling Condition 5 used the same method AFGROW modeling inputs as Condition 4 with a different loading and environment spectrum (Figure 38).

Segment	S_{max} (MPa)	S_{min} (MPa)	Cycles	Altitude (m)	Actual (◦C)	Binned (◦C)
PRE-FLIGHT TAXI	51.37	19.37	1	0	15.02	23
CLIMB	85.43	62.61	1	1524	5.07	23
CLIMB	89.57	58.47	1	4572	-14.71	-15
CLIMB	90.53	66.19	2	7620	-34.48	-30
CLIMB	86.46	64.61	1	10667	-54.21	-57
CRUISE	101.49	62.37	20	12496	-56.48	-57
DESCENT	71.50	48.61	1	10667	-54.21	-57
DESCENT	73.57	46.54	1	7620	-34.48	-30
DESCENT WITH S/B	69.92	38.75	1	4572	-14.71	-15
DESCENT	75.64	44.47	1	1524	5.07	23
APPROACH	94.12	62.97	8	1524	5.07	23
LANDING	73.02	67.23	2	0	15.02	23
POST-FLIGHT TAXI	4.25	2.28	44	0	15.02	23
GAG	101.49	2.28	1	VARIOUS	16.96	23

Figure 38: Business Jet Load-Environment Spectrum

5.3 Results

5.3.1 Modeling Condition 1: Constant Stress, Constant Environments

The AFGROW predicted life for Modeling Condition 1 is reported in Figure 39. Specifically, the cycles to failure are calculated using growth kinetics (Figure 34) for UHV and 2668, 4, 0.54 Pa environment are plotted for various maximum stress levels. Critically, the 4 Pa and 0.54 Pa conditions reflect environmental conditions relevant to flight environments at 9,144 to 18,288 meters of altitude. Two relevant trends are observed. First, at all stress levels the use of reduced water vapor environment growth kinetics increases the predicted fatigue life. For example, at a maximum stress level of 100 MPa there is 5 to 10-fold increase using data representative of flight environments, and nearly two orders of magnitude increase in life using UHV data. Second, the magnitude of the increase in fatigue life decreases as the stress increases. This is expected given the enhanced role of mechanical damage on the fatigue crack growth kinetics and the decrease in environmental dependence observed in Figure 34 as ΔK increases. Similar modeling efforts have previously been shown to accurately capture crack extension from corrosion features at different temperatures, provided that the respective environment specific growth rates are used.[131] This correspondence validates the application of the similitude principle and justifies the use of such modeling techniques to demonstrate the impact of using environment specific kinetics in life prediction modeling for various configurations and spectrums.

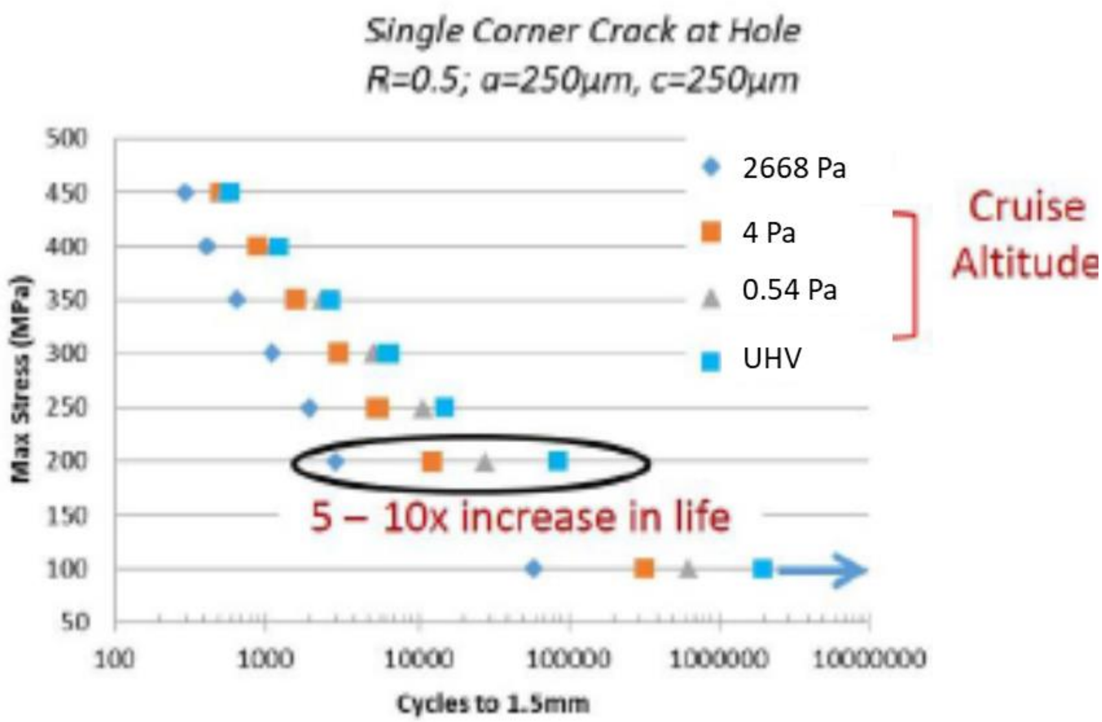

Figure 39: Modeling Condition 1: Max stress (MPa) versus cycles to 1.5 mm crack length for constant load, constant environment model. This was done at a variety of water vapor pressures and max stresses and are shown here.

5.3.2 Modeling Condition 2: Variable Stress, Variable Environments

The stress application (blue) and AFGROW predicted crack extension results for Condition 2, using growth rate data for a constant water vapor pressure (green) or data from various water vapor pressures (red) are reported in Figure 40. While this effort does not scan various maximum stress conditions, it clearly demonstrates that the life extension achieved for constant stress and environment conditions (Figure 39) persists for variable stress levels and variable environment simulations. Specifically, the damage progression was drastically slowed and the cycles to failure increased by 257% when high altitude environment crack growth kinetics were employed for portions of the loading cycles. The crack extension versus cycles plots shows that the increase in life is dominated by slowing of the rapid growth that occurred during the high ΔK final portion of the loading block (e.g., maximum stress of 300 MPa and R=0.1). Despite the decreased disparity between the high humidity and high-altitude environment growth rates at higher ΔK (Figure 34) the impact on life is most potent in that regime due to the fact that the majority of crack advance occurs in response to the cycles with a high ΔK driving force.

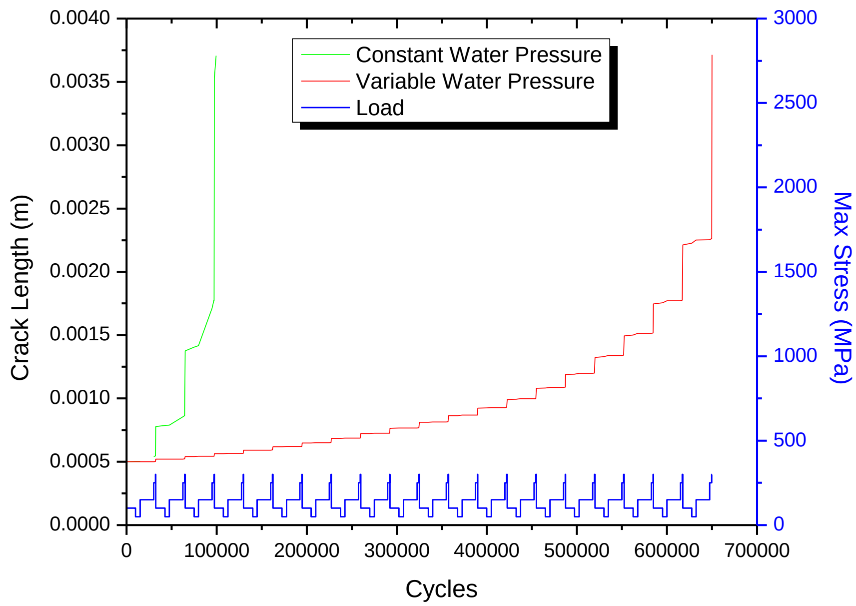

Figure 40: Modeling Condition 2: Crack growth versus cycles for an arbitrary variable load and environment loading condition. Constant water vapor pressure (green) utilized da/dN data generated at 2668 Pa while the variable water pressure curve (red) utilized da/dN from a variety of pressures, detailed in Table 7. The blue curve represents the stress at each cycle and high stresses can be seen to correspond with large jumps in crack length.

5.3.3 Modeling Condition 3: ENSTAFF Generalized Load-Environment Spectrum

Modeling results for Condition 3 are reported in Figure 41 and compare a coupled load-environment spectrum (ENSTAFF; orange), with the same variable load spectrum but a constant high humidity environment (FALSTAFF; blue). Figure 41 and

	Cycles to failure	Cycles to failure	Change in fatigue life
Max Stress (MPa)	Realistic Pressures	High Humidity	% Difference
50	27,813,004	16,057,865	**73.2%**
100	1,426,156	852,299	**67.3%**
150	299,807	191,909	**56.2%**
200	92,273	63,954	**44.2%**
300	12,079	10,005	**20.7%**

Table 10 show that the cycles to failure increased dramatically when the environment-specific da/dN vs. ΔK values are applied, with a 67.3% increase in cycles for the 100 MPa condition. As was observed for Condition 1, the higher the maximum stress, the smaller the observed increase in fatigue life associated with using environment specific da/dN vs. ΔK relationships. Even though the magnitude of increase in fatigue life are lower than in Condition 2, there are still significant increases in fatigue life by applying realistic cracking environments to in-service loading spectrum, particularly at lower stress levels. These results are a strong demonstration of the potential impact of realistic service conditions on the structural integrity management of airframes, albeit for a generalized coupled load-environment spectrum.

	Cycles to failure	Cycles to failure	Change in fatigue life
Max Stress (MPa)	Realistic Pressures	High Humidity	% Difference
50	27,813,004	16,057,865	**73.2%**
100	1,426,156	852,299	**67.3%**
150	299,807	191,909	**56.2%**
200	92,273	63,954	**44.2%**
300	12,079	10,005	**20.7%**

Table 10: Cycles to failure for modeling Condition 3 at a variety of stresses for both mixed da/dN and high humidity FCGR data as well as the relative difference between them.

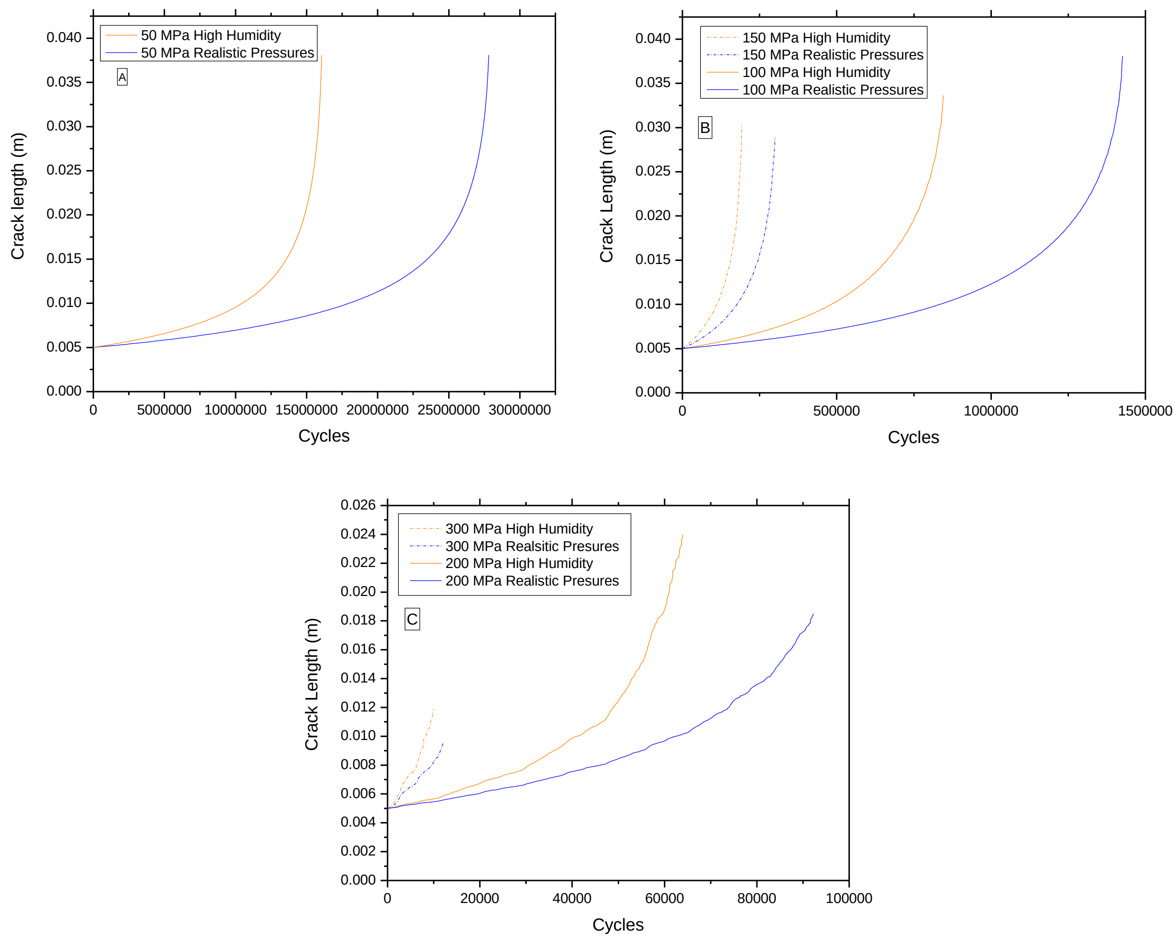

Figure 41: Modeling Condition 3: Crack growth versus cycles to failure for realistic loading-environment spectrum for a general fighter generated from ENSTAFF. High humidity curves (orange) utilized da/dN data from 2668 at all cycles. Realistic pressures curves (blue) utilized da/dN a variety of da/dN curves based on ENSTAFF environmental temperature data and relating these temperatures to an altitude and then a corresponding pressure detailed in Table 5. This was repeated for max stresses of 50 MPa (A), 100 MPa (B), 200 MPa and 300 MPa (C).

5.3.4 Modeling Conditions 4 and 5: Boeing 707 and Business Jet

Conditions 4 and 5, applied environment specific FCGRs to the spectra relevant to: (1) the Boeing 707, and (2) a business jet, respectively. Figure 42 and Figure 43 show that there was a substantial increase in the fatigue life of both planes undergoing in-service loading when the proper environmental growth rate is applied to each load. The Boeing 707 was calculated to have a 79% increase in fatigue life and the business jet saw a 67% increase in fatigue life. It was also estimated, that for the Boeing 707, this increase in fatigue life would decrease the inspection burden by roughly half. This can provide critical savings both in monetary costs for inspection as well as increased airframe availability.

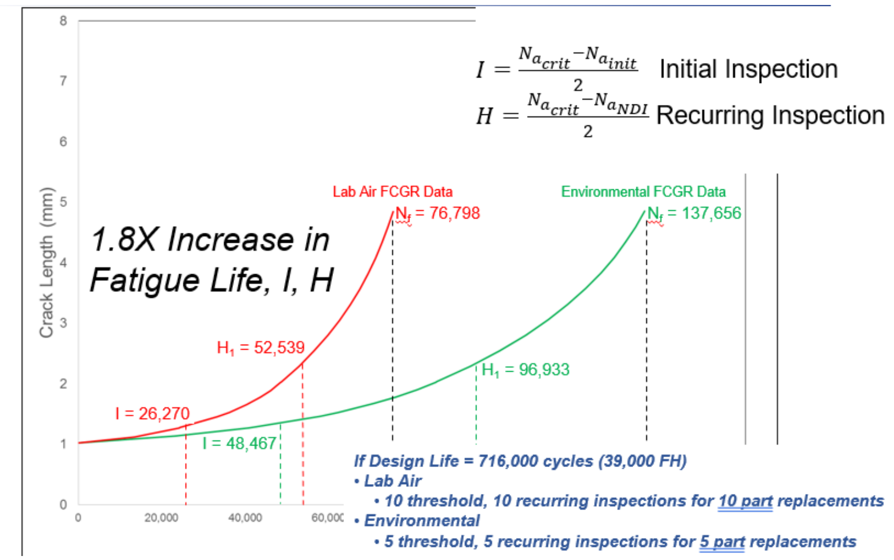

Figure 42: Comparison in inspection intervals for the Boeing 707 using the environmental/mechanical loading spectrum compared to laboratory air fatigue crack growth rates, based on cycles to critical crack length using AFGROW models.

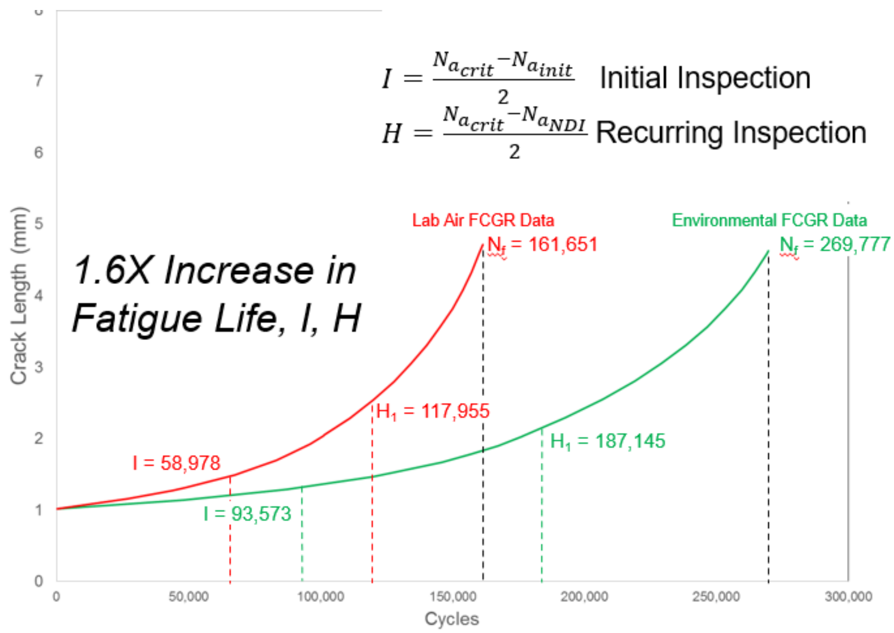

Figure 43: Comparison in inspection intervals for the business jet using the environmental/mechanical loading spectrum compared to laboratory air fatigue crack growth rates, based on cycles to critical crack length using AFGROW models.

5.4 Discussion:

5.4.1 Stress Level Dependent Environmental Fatigue Impact

The increased fatigue lives observed when low water vapor FCGR are applied to LEFM modeling across all modeling conditions indicate that incorporating environment-specific da/dN vs. ΔK relationships can potentially have a significant impact airframe structural management. Modeling Condition 1 demonstrated that the largest increase in fatigue life was seen at low stress levels. The high increases in fatigue life at low stresses is consistent with literature showing that environmental cracking is exacerbated at low ΔK but has a less potent impact at higher ΔK levels where the mechanical driving force dominates.[57]

However, results from Condition 2 indicate that a vast majority of crack advance occurs during high stress portion of the loading profile. This suggests that even if the relative magnitude of the growth rate reduction is highest at low stresses, the more modest growth rate reduction at high stress levels has a more potent impact on the overall fatigue life. For example, if a crack advances 10 µm at low stresses for a given number of cycles, an environment induced 50% reduction in da/dN would decrease crack extension by roughly 5 µm. At higher stresses, say the crack advances 400 µm in a given number of cycles, if the da/dN is reduced by only 25%, the crack advance would be still be reduced by 100 microns. This analysis suggests that even through the relative reduction in da/dN is smaller at higher stress levels (e.g., ΔK levels), the integration of high-altitude specific growth kinetics for the high stress portions of the load cycle can have a more potent impact on the total fatigue life.

To investigate this effect further, an additional series of modeling scenarios was performed (Condition 6). Specifically, an arbitrary load spectrum was developed where 1000 cycles were performed at 0.5σ (σ represents a given stress that can be varied), then 30 cycles at σ. In Scenario 1, the FCGRs for 2668 Pa will be applied for the 0.5σ cycles and UHV for the σ cycles. In Scenario 2, the FCGRs for UHV will be applied for the 0.5σ cycles and 2668 Pa for the σ cycles. This is shown in Table 11. The results of these modeling scenarios will be compared to determine the effect this phenomenon has on crack progression. Cycle-by-cycle beta and spectrum calculation was performed with an output selected every 1 mm. The failure conditions were K_{max} exceedance and crack growth to a free surface. The geometry of the specimen was a center semi-elliptic surface flaw with a W and T of 100 mm and an initial flaw of 0.5 mm shown in Figure 35. Two values of σ were explored (100 MPa and 200 MPa). Consistent with the prior discussion, Scenario 1 (e.g., UHV at σ) exhibited the highest increase in fatigue life (Figure 44) and Scenario 2 (e.g., UHV at 0.5σ) showed a minimal increase in fatigue life. This simple and targeted evaluation confirms the important interaction between the magnitude of the environment induced da/dN reduction, the stress level, and the number of loading cycles.

Stress (MPa)	Cycles	R	Environmental Condition 1	Environmental Condition 2
0.5 σ	1000	0.5	2668 Pa	UHV
σ	30	0.1	UHV	2668 Pa

Table 11: Load and environmental spectrum for modeling Condition 6. σ is a stress that can be varied (σ = 50 MPa and 100 MPa for this study)

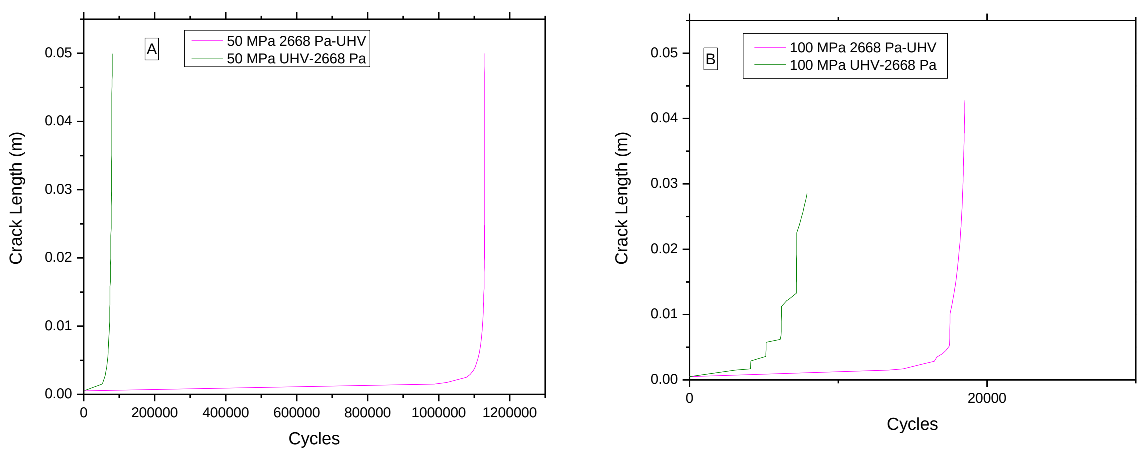

Figure 44: Modeling Condition 6: Crack length versus cycles for study on the effects of low water vapor pressure at high or low stresses. The legend details which environment is assigned at each of the stress levels (shown in Table 9), and what σ is equal to (50 MPa in A, 100 MPa in B). The first pressure corresponds with 1000 cycles at 0.5 σ and the second pressure with 30 cycles at σ.

It is also useful to consider the generalized load-environment spectrum evaluated in Condition 3 which demonstrated 20 - 73% increases in predicted fatigue life. The model was run for 5 different values of stress (Figure 44); critically, this value set the maximum and the rest of the spectrum was proportionally scaled to that value. The results show that there was a higher potency of the environmental effect for lower maximum stress values (73% increase in life for 50 MPa) as compared to the higher maximum stress values (20% for 300 MPa). This finding suggests that while implementing the environmental effect on the high stress peaks within the spectrum will be most influential on the life (per the prior discussion), reducing the overall severity of the spectrum (by reducing the maximum stress to which the spectrum is scaled) resulted in increased potency of the environmental impact.

For any given airframe component, the exact interplay between differences in da/dN reduction at different ΔK values and the overall predicted fatigue life will vary for different load-environment spectrum. This important observation highlights the utility of such LEFM-based prediction tools to the structural integrity management community.

5.4.2 Modeling of Real-world Airframe Components

While the results in Figure 42 and Figure 43 suggest that there is the potential to impact structural management of airframe components, the preceding discussion suggestions that the potency of the impact can vary with the details of the coupled load-environment spectrum. Modeling Conditions 3-5 exercise the environment specific LEFM modeling code for a common generalized spectrum and for two specific airframe components to determine the impact of for service relevant conditions. While the results in Figure 41, Figure 42, and Figure 43 reflect the expected distribution of potency of the environmental effect for different spectra, each of the modeling cases clearly demonstrate a tangible beneficial impact.

Using the coupled load-environment spectrum in Figure 36 for the Boeing 707 in the LEFM crack growth rate modeling tool the benefit of the environmentally influenced crack growth rates becomes clear. The semi-circular initial flaw size of 1.27 mm is based on the detectability limit for non-destructive inspection techniques.[133] The inspection interval for parts is set such that two inspections are required before an initial flaw would grow to a critical crack length.[133] Using the coupled load-environment spectrum was shown to decrease the inspection burden by a factor of 1.8. Figure 42 shows the comparison of the inspection burden for the initial and recurrent inspections using the laboratory air crack growth rate data and the combined spectrum.[133] Using the coupled load-environment spectrum for a business jet reduces the inspection interval by a factor of 1.6.[133] Figure 43 shows the comparison of the time to critical flaw size for the business jet example.[133]

Increased inspection intervals are of great interest to the airframe structural management community due to the potential for cost reductions by eliminating unneeded inspections. For the 707 case the number of required inspections over the life of an aircraft part, assuming 719,000 cycles (39,000 flight hours) would reduce from 10 inspections and 10-part replacements to 5 inspections and replacements. This cost savings would be substantial. Likewise, there is cost savings in reduced aircraft unavailability due to inspection time. While the quantitative accuracy of the model outputs are notional due to the simple modeling assumptions (e.g., no retardation, not accounting for frequency in the exposure parameter, the use of a single R-ratio for FCGRs, etc.), the scale of the environmental effect would persist with increasing model complexity to incorporate these factors. *In toto*, the current data demonstrate that using appropriate spectrum to life aircraft could substantially increase readiness for the Department of Defense and commercial fleets, while also reducing costs.

5.4.3 Opportunities and Challenges

Incorporation of environment-specific fatigue crack growth kinetics into the LEFM-framework used to manage the structural integrity of airframe components allows these models to more accurately reflect in-service conditions of the component. The current study focuses on reaping the beneficial effects of high-altitude environments on AA7075 to decrease the inspection burden and enable enhanced design. However, this environmental cracking framework can be applied to other material and environment combinations that may exhibit spectrum loading during flight. For example, one could envision a spectrum of environments for carrier-based airframes that may range from aqueous (with associated galvanic coupling with other components or metal-pigment laden coatings) to humid air, to dry air for a given mission profile. Generally, any coupled load-environment can be probed so long as there are growth kinetics that are representative of the environment, K-solution for the component, and a coupled load-environment spectrum. Furthermore, while the focus of this paper was to generate life predictions that would inform future structural integrity management, the full breadth of the LEFM approach can also be employed to inform material selection, evaluate mitigation strategies, enhance/optimize component design, and understand the sensitivity of components to a change in operational environment.

The findings reported above are promising, however there remain challenges to incorporating high-altitude environments into LEFM-modeling. First, it is critical that laboratory generated environment specific growth rate data exhibit similitude with components across a wide range of stress intensities. This is particularly relevant for AA7075-T651 in high-altitude environments where both temperature and crack wake roughness can to compromise similitude for constant ΔK and bulk environment (e.g., P_{H2O}/f) conditions.[5,10,134,11,14,17,19,20,28,54,57] Second, the current approach assumes that there is no transient upon transitioning between environments. This assumption is reasonably supported by the underlying H-based mechanisms that govern the growth rate enhancement beyond the pure mechanical behavior observed at UHV. In the H-embrittlement paradigm, H is considered to be generated, adsorbed at the crack tip, and then diffused into the crack tip process zone. In the crack tip region H will align with and be trapped due to the crack tip hydrostatic stress and the local plastic damage structure. As such any environment induced transient associated with switching between environments would be governed by cracking through either a precharged or depleted H-gradient that was caused by the prior environmental condition. While the details of the stress state, the local damage structure, and the diffusion kinetics are complicated, it is reasonable to expect that the H field will be localized within <20 µm of the crack tip based on the localized crack tip stress field (described by conventional HRR fields[135,136] or strain gradient plasticity[137]) and the low diffusivity of H in Al-alloys.[138] At the growth rates reported in Figure 34 the crack would rapidly pass through the first 20 µm. Regardless, further study is needed to validate this assumption. Third, more work is needed to generating load-environment spectrum as each application can vary and accurate coupled spectrums are needed to apply environmental FCGR at high altitude for damage tolerant models. Finally, a systematic validation of the accuracy of the crack progression for a coupled load-environment spectrum is needed.

5.5 Conclusions:

Utilizing an LEFM program, AFGROW, the environmental effect on fatigue life on AA 7075-T651 in aerospace applications was quantitatively determined. Through several different modeling conditions, the fatigue life in low water vapor environments consistently produced significant increases in fatigue life. Of critical interest, the following conclusions were determined.

- Simple, constant stress, constant environment conditions showed up to an order of magnitude increase in fatigue life when comparing high humidity environments with UHV environments. The highest change is observed at low stresses, with smaller increases in fatigue life at higher stresses.
- As more realistic loading-environment spectra were used in modeling Conditions 2-5, significant increases in fatigue life were observed, though no longer orders of magnitude as was seen in the single environment modeling condition. Again, at low stresses, the relative change in fatigue life was greater across all different modeling conditions.
- While environmental effects are most potent in the near-threshold regime of the da/dN vs. ΔK relationship, targeted modeling demonstrates that the majority of the crack extension occurs at high stresses (thus high ΔK). This leads to the counter-intuitive conclusion that, despite the lower relative impact of environment on the da/dN at high ΔK, the environmental effect at high stress levels has a more significant impact on the total fatigue life.
- Through these results, it is clear that implementation of low water vapor pressure, low temperature, environmental FCGR into the next generation of airframe structural

integrity management models can have a profound impact. While more work is needed to be done to reach this goal, this research makes a compelling case for continuing the needed research to make this goal a reality.

Chapter 6 – Final Conclusions

This work found that the exposure parameter, which had previously been used to describe the severity of the low water vapor pressure environment, has situations where it fails to predict environmental cracking of aluminum alloy 7075. At high water vapor pressures, the frequency no longer has an effect on the crack growth rate, and the exposure parameter is no longer a valid descriptor of the environment. The exposure parameter is still the best variable to describe the environment in low to intermediate water vapor pressures so it can still be a useful environmental parameter. Caution must be used to ensure the environments it is being applied to are within the range of water vapor pressures it describes.

Investigations into the threshold transition regime (TTR) behavior showed that sample thickness has no impact on the crack behavior across all water vapor pressures, even those experiencing the TTR. Investigations into this result using Franc3D, demonstrated that the irregular crack front results in a large increase in the ΔK at the center of the sample. Additionally, further modeling showed that constant size side cracks for all three thicknesses did not result in a similar ΔK profile, as suggested by the identical da/dN curves. Further modeling is needed to investigate this result and iterate on the currently proposed hypothesis to explain this behavior.

Study of the high atmosphere environment in AA 2199 showed that a similar behavior was observed compared to 7075 at room temperature. 2199 did experience an earlier limit on environmental damage where no environmental cracking was occurring compared to 7075. The TTR was present in 2199 as well but it was overall less severe which was attributed to the smaller effect of H on the 2199. Low temperature testing showed that above -15 °C, temperature had no effect on the growth rates. When above the critical water vapor for environmental cracking, lower temperatures decreased, leading to the conclusion that environmental cracking was being affected. It was suggested this was due to changes in the H-dislocation interactions as temperatures decreased.

When applying low water vapor crack growth rates to linear elastic fracture mechanics (LEFM) fatigue life models, large increases in fatigue life were observed in simple environments, more modest but significant life extension was observed as in-service conditions were applied. Additionally, an interesting interplay was discovered where even though low stresses have a larger impact of environmental damage, it was found that having the high stress loads occur at a low water vapor pressure had a larger overall impact on the fatigue life estimates. These findings suggest that further study into the high atmosphere environment is warranted to hopefully better understand the complicated environmental cracking behavior of aluminum alloys.

Acknowledgments

I would like to first of thank my advisor, James Burns for working with me on this project over the last five years. Additionally, I would like to thank my thesis committee members, Sean Agnew, Rob Kelly, James Fitzgerald, and Haibo Dong for their time and effort helping to guide my path forward on my dissertation. I would like to thank my group members over the years for their comradery and help, particularly Adam Thompson who worked with me a great deal on the third chapter of my dissertation I would like to thank Jenifer Locke and Jenny Jones who performed the experimental work and were coauthor on the fourth chapter of my thesis. I want to thank Sarah Galyon Dorman with SAFE engineering who performed work on the Boeing 707 and Business jet AFGROW modeling work on the fifth chapter of my thesis. Finally, I would like to thank Joe Cochran and Jake Hochhalter who performed the stress intensity modeling of the irregular crack front in the third chapter of my dissertation.

Finally, I would like to thank all of my family and friends who supported me during grad school both in Charlottesville and back home in Orlando. Without these relationships I would not have chosen to finish my dissertation but their friendship made my time in Charlottesville better than I could have envisioned. Thank you for finishing first year homework's up together at 3 A.M., driving me to the emergency room, helping me unflood my apartment, go to basketball games together, help move me 5 times in one year, take me to pick up my car stuck in a field for a month, and yell at me that I wasn't allowed to graduate with my just my master degree. You guys are the best.

References

[1] Molent L. Fatigue crack growth from flaws in combat aircraft. Int J Fatigue 2010;32:639–49. https://doi.org/10.1016/j.ijfatigue.2009.09.002.

[2] Wanhill RJH, Koolloos MFJ. Fatigue and corrosion in aircraft pressure cabin lap splices. Int J Fatigue 2001;23:337–47. https://doi.org/10.1016/s0142-1123(01)00147-5.

[3] Wallace W, Hoeppner D, Kandachar P. AGARD Corrosion HandBook Volume 1 Aircraft Corrosion: Causes and Case Histories. vol. 1. 1985.

[4] Lynch SP. Failures of Engineering Components Due to Environmentally Assisted Cracking. vol. 3. 2003.

[5] Burns JT, Jones JJ, Thompson AD, Locke JS (Warner. Fatigue crack propagation of aerospace aluminum alloy 7075-T651 in high altitude environments. Int J Fatigue 2018. https://doi.org/10.1016/j.ijfatigue.2017.09.017.

[6] de Jonge JB, Schutz D, Lowak H, Schijve J. A standarized load sequence for flight simulation tests on transport aircraft wing structures. 1973.

[7] de Jonge JB, Spickhout DJ. Use of AIDS recorded data for assessing service load experience. In: Abelkis PR, Potter JM, editors. Serv. fatigue loads Monit. simulation, Anal., West Conshohocken, PA: ASTM; 1979, p. 48–66.

[8] Hunt EH, Reid DH, Space DR, Tilton FE. Commercial Airliner Environmental Control System Engineering Aspects of Cabin Air Quality. 1995.

[9] Sampieri RH. U.S. Standard Atosphere 1976. 1976.

[10] Burns JT. Effect of water vapor pressure on the fatigue crack propagation of aerospace aluminum alloys 7075-T651 and 2199-T86. Proc. DoD Corros. Conf., 2013.

[11] Burns JT. THE EFFECT OF INITIATION FEATURE AND ENVIRONMENT ON FATIGUE CRACK FORMATION AND EARLY PROPAGATION IN Al-Zn-Mg-Cu. University of Virginia, 2010.

[12] Weiderhold PR. Water Vapor Measurement: Methods and Instrumentation. 1997.

[13] Burns JT, Bush RW, Ai JHH, Jones JLL, Lee Y, Gangloff RPP. Effect of water vapor pressure on fatigue crack growth in Al-Zn-Cu-Mg over wide-range stress intensity factor loading. Eng Fract Mech 2015;137:34–55. https://doi.org/10.1016/j.engfracmech.2014.11.009.

[14] Petit J, Sarrazin-Baudoux C. Some critical aspects of low rate fatigue crack propagation in metallic materials. Int J Fatigue 2010;32:962–70. https://doi.org/10.1016/j.ijfatigue.2009.10.013.

[15] Wei RP, Pao PS, Hart RG, Weir TW, Simmons GW. Fracture Mechanics and Surface Chemistry Studies of Fatigue Crack Growth in an Aluminum Alloy. Metall Trans A 1980;11:151–8. https://doi.org/10.1007/BF02700451.

[16] Ruiz J, Elices M. Effect of water vapour pressure and frequency on fatigue behaviour in

7017-T651 aluminium alloy plate. Acta Mater 1997;45:281–93. https://doi.org/10.1016/S1359-6454(96)00147-4.

[17] Burns JT, Gangloff RP. Effect of Low Temperature on Fatigue Crack Formation and Microstructure-Scale Growth from Corrosion Damage in Al-Zn-Mg-Cu. Metall Mater Trans A 2013;44:2083–105. https://doi.org/10.1007/s11661-012-1374-3.

[18] Pettit DE, van Orden JM. Evaluation of Temperature Effects on Crack Growth in Aluminum Sheet Material. Fract Mech 1979:106–24. https://doi.org/10.1520/stp34909s.

[19] Yarullin R, Ishtyryakov I. Fatigue Surface Crack Growth in Aluminum Alloys under Different Temperatures. Procedia Eng 2016;160:199–206. https://doi.org/10.1016/j.proeng.2016.08.881.

[20] Park KJ, Lee CS. Fatigue crack propagation in Al-Li 8090 alloy at room (300K) and cryogenic (77K) temperatures. Scr Mater 1996;34:215–20. https://doi.org/10.1016/1359-6462(95)00505-6.

[21] Abelkis PPR, Harmon MMB, Hayman EL EL, Mackay TT., Orlando J, Orlanod J, et al. Low Temperature and Loading Frequency Effects on Crack Growth and Fracture Toughness of 2024 and 7475 Aluminum. Fatigue Low Temp ASTM STP 857 1985:257–73. https://doi.org/10.1520/stp32760s.

[22] Burns JT, Gangloff RP. Scientific advances enabling next generation management of corrosion induced fatigue. Procedia Eng 2011;10:362–9. https://doi.org/10.1016/j.proeng.2011.04.062.

[23] Smith MA, King HF. Airframe Fatigue: A.R.B's chief technical officer gives the second Barnwell Lecture. Flight Aircr Eng 1955:347–52.

[24] Harper RHT. Fatigue in aircract structures. New Sci 1957:23–5.

[25] Press H, Steiner R. An approach to the problem of estimating severe and repeated gust loads for missle operations. Natl. Advis. Comm. Aeronaut. Collect., Langley Field, Va.: 1958.

[26] Schutz D, Gerharz JJ. ENSTAFF A Standard Test Sequence For Composite Components Combining Load And Environment. ICAF, 1987, p. 425–44.

[27] McMurtrey MD, Jones JL, Burns JT. Effect of High Altitude Environments on Fatigue Crack Propagation Rates in Aerospace aluminum Alloys. NACE DOD corroison Conf., 2015.

[28] Jones JL, McMurtrey MD, Brown L, Burns JT. The effect of crack wake roughness on the environmentally assisted fatigue behavior of an aerospace Al-alloy in low moisture environments. Eng Fract Mech 2018;199. https://doi.org/10.1016/j.engfracmech.2018.05.038.

[29] Gao M, Wei RP, Pao PS. Chemical and metallurgical aspects of environmentally assisted fatigue crack growth in 7075-T651 aluminum alloy. Metall Trans A 1988;19:1739–50. https://doi.org/10.1007/BF02645142.

[30] Pao PS, Gao M, Wei RP. Environmentally assisted fatigue-crack growth in 7075 and 7050 aluminum alloys. Scr Metall 1985;19:265–70. https://doi.org/10.1016/0036-9748(85)90310-2.

[31] Ruiz J, Elices M. The role of environmental exposure in the fatigue behaviour of an aluminium alloy. Corros Sci 1997;39:2117–41. https://doi.org/10.1016/S0010-938X(97)00095-4.

[32] Bonakdar A, Wang F, Williams JJ, Chawla N. Environmental Effects on Fatigue Crack Growth in 7075 Aluminum Alloy. Metall Mater Trans A 2012;43:2799–809. https://doi.org/10.1007/s11661-011-0810-0.

[33] Henaff G, Marchal K, Petit J. On fatigue crack propagation enhancement by a gaseous atmosphere: Experimental and theoretical aspects. Acta Metall Mater 1995;43:2931–42. https://doi.org/10.1016/0956-7151(95)00002-D.

[34] Bennett JA. Changes in the influence of atmospheric humidity during fatigue of an aluminum alloy. J Res Natl Bur Stand Sect C Eng Instrum 1964;68C:91–100. https://doi.org/10.6028/jres.068c.010.

[35] Petit J, Hénaff G, Sarrazin-Baudoux C. Environmentally Assisted Fatigue in the Gaseous Atmosphere. Compr. Struct. Integr., Elsevier; 2003, p. 211–80. https://doi.org/10.1016/B0-08-043749-4/06130-9.

[36] Weir TW, Simmons GW, Hart RGG, Wei RP. A Model for Surface Reaction and Transport Contolled Gatigue Crack Growth. Scr Metall 1980;14:357–64. https://doi.org/10.1016/0036-9748(80)90359-2.

[37] Pao PS, Gao M, Wei RP. Critical assessment of the model for transport-controlled fatigue crack growth. In: Wei RP, Gangloff RP, editors. Basic Quest. fatigue, ASTM STP 924, West Conshohocken, PA: ASTM International; 1987, p. 182–95.

[38] Wei RP, Simmons GW. Surface Reactions and Fatigue Crack Growth. 1981. https://doi.org/10.1057/9780230360341.0191.

[39] Achter MR. The adsorption model for environmental effects in fatigue crack propagation. Scr Metall 1968;2:525–7. https://doi.org/10.1016/0036-9748(68)90187-7.

[40] Wei RP, Gao M. Hydrogen embrittlement and environmentally assisted crack growth. Hydrog. Eff. Mater. Behav., 1990, p. 789–816.

[41] Weir TW, Simmons GW, Hart RG, Wei RP. A model for surface reaction and transport controlled fatigue crack growth. Scr Metall 1980;14:357–64. https://doi.org/10.1016/0036-9748(80)90359-2.

[42] Ro Y, Agnew SR, Bray GH, Gangloff RP. Environment-exposure-dependent fatigue crack growth kinetics for Al–Cu–Mg/Li. Mater Sci Eng A 2007;468–470:88–97. https://doi.org/10.1016/J.MSEA.2007.01.155.

[43] Gangloff RP. Environment sensitive fatigue crack tip processes and propagation in

aerospace aluminum alloys. Fatigue 2002;2:3401–33.

[44] Nagao A, Smith CD, Dadfarnia M, Sofronis P, Robertson IM. The role of hydrogen in hydrogen embrittlement fracture of lath martensitic steel. Acta Mater 2012;60:5182–9. https://doi.org/10.1016/J.ACTAMAT.2012.06.040.

[45] Moreto JA, Júnior FAP, MacIel CIS, Bonazzi LHC, Júnior JFL, Terra Ruchert COF, et al. Environmentally-assisted fatigue crack growth in AA7050-T73511 al alloy and AA2050-T84 Al-Cu-Li alloy. Mater Res 2015;18:1291–7. https://doi.org/10.1590/1516-1439.018915.

[46] Wilhelm M, Nageswararao M, Meyer R. Factors Influencing Stage I Crack Propagation in Age-Hardened Alloys. Fatigue Mech., West Conshohocken, PA: ASTM International; n.d., p. 214–33. https://doi.org/10.1520/STP35891S.

[47] Wei R. Fracture Mechanics: Integration of Mechanics, Materials Science and Chemistry. New York: Cambridge University Press; 2010.

[48] Robertson IM, Sofronis P, Nagao A, Martin ML, Wang S, Gross DW, et al. Hydrogen Embrittlement Understood. Metall Mater Trans B 2015;46:1085–103. https://doi.org/10.1007/s11663-015-0325-y.

[49] Gerberich WW, Stauffer DD, Sofronis P. A coexistent view of hydrogen effects on mechanical behavior of crystals: HELP and HEDE. Proc 2008 Int Hydrog Conf - Eff Hydrog Mater 2009:38–45.

[50] Birnbaum HK, Sofronis P. Hydrogen-enhanced localized plasticity-a mechanism for hydrogen-related fracture. Mater Sci Eng A 1994;176:191–202. https://doi.org/10.1016/0921-5093(94)90975-X.

[51] Wei RP. Environmental considerations for fatigue cracking. Fatigue Fract Eng Mater Struct 2002;25:845–54. https://doi.org/10.1046/j.1460-2695.2002.00551.x.

[52] Wei RP, Gao M, Pao PS. The role of magnesium in CF and SCC of 7000 series aluminum alloys. Scr Metall 1984;18:1195–8. https://doi.org/10.1016/0036-9748(84)90104-2.

[53] Gasem Z, Gangloff RP. Rate-Limiting Processes in Environmental Fatigue Crack Propagation in 7000-weries Aluminum Alloys. Chem. Electrochem. Stress Corros. Crack. A Symp. Honor. Contrib. R.W. Staehle, 2001, p. 501–21.

[54] Jones J. The Effect of Water Vapor Pressure on the Fatigue Crack Propagation Rates in Aerospace Aluminum Alloys 7075-T651 and 2199-T86. University of Virginia, 2015.

[55] Wright MA, Hordon MJ. Effect of Residual Gas Composition on the Fatigue Behavior of Aluminum. Trans Metall Soc AIME 1968;242:713–4.

[56] Bradshaw FJ, Wheeler C. The influence of gaseous environment and fatigue frequency on the growth of fatigue cracks in some aluminum alloys. Int J Fract Mech 1969;5:255–68. https://doi.org/10.1007/BF00190956.

[57] Tchitembo Goma FA, Larouche D, Bois-Brochu A, Blais C, Boselli J, Brochu M. Effect of extrusion aspect ratio and test temperatures on fatigue crack growth behavior of a 2099-T83 Al-Li alloy. Int J Fatigue 2014;59:244–53. https://doi.org/10.1016/j.ijfatigue.2013.08.013.

[58] ASTM E647-13. Standard Test Method for Measurement of Fatigue Crack Growth Rates. Am Soc Test Mater 2013:1–49.

[59] Thompson A. The effect of high altitude environments on the dislocation structure evolution during fatigue cracking of legacy aeropsace aluminum alloy 7075-T651. 2022.

[60] Brown L, Jones JL, (Warner) Locke JS, Burns JT. Effect of low temperature, low water vapor pressure environments on the fatigue behavior of an Al-Li aerospace alloy. Int J Fatigue 2021;148:106215. https://doi.org/10.1016/j.ijfatigue.2021.106215.

[61] Akhurst KN, Baker TJ. The threshold stress intensity for hydrogen-induced crack growth. Metall Trans A 1981 126 1981;12:1059–70. https://doi.org/10.1007/BF02643487.

[62] Branco R, Antunes F V., Martins RF. Modelling fatigue crack propagation in CT specimens. Fatigue Fract Eng Mater Struct 2008;31:452–65. https://doi.org/10.1111/J.1460-2695.2008.01241.X.

[63] Bakker A. THREE-DIMENSIONAL CONSTRAINT EFFECTS ON STRESS INTENSITY DISTRIBUTIONS IN PLATE GEOMETRIES WITH THROUGH-THICKNESS CRACKS. Fatigue Fract Eng Mater Struct 1992;15:1051–69. https://doi.org/10.1111/J.1460-2695.1992.TB00032.X.

[64] Luchi ML, Rizzuti S. Boundary element analysis of CT specimens with straight and curved crack fronts. Int J Fract n.d.;34:23–40. https://doi.org/10.1007/bf00042122.

[65] Brown L, Jones JL, (Warner) Locke JS, Burns JT. Effect of low temperature, low water vapor pressure environments on the fatigue behavior of an Al-Li aerospace alloy. Int J Fatigue 2021;148. https://doi.org/10.1016/J.IJFATIGUE.2021.106215.

[66] Jata K V., Starke EA. Fatigue crack growth and fracture toughness behavior of an Al-Li-Cu alloy. Metall Trans A 1986;17:1011–26. https://doi.org/10.1007/BF02661267.

[67] Rao KTV, Ritchie RO. Fatigue of aluminium—lithium alloys. Int Mater Rev 1992;37:153–86. https://doi.org/10.1179/imr.1992.37.1.153.

[68] Duva JM, Daeubler MA, Starke EA, Luetjering G. Large shearable particles lead to coarse slip in particle reinforced alloys. Acta Metall 1988;36:585–9. https://doi.org/10.1016/0001-6160(88)90091-0.

[69] Piascik RS, Gangloff RP. Environmental fatigue of an Al-Li-Cu alloy: Part II. Microscopic hydrogen cracking processes. Metall Mater Trans A 1993;24:2751–62. https://doi.org/10.1007/BF02659499.

[70] Pao PS, Cooley LA, Imam MA, Yoder GR. Fatigue-crack growth in 2090 Al-Li alloy. Scr Metall 1989;23:1455–60. https://doi.org/10.1016/0036-9748(89)90076-8.

[71] Blankenship CP. Optimizing Mechanical Properties in Al-Li-X Alloys by microstructural Design. 1992.

[72] YODER GR, PAO PS, IMAM MA, COOLEY LA. Unusual Fracture Mode in the Fatigue of an Al-Li Alloy. Proc 7th Int Conf Fract 1989:919–27. https://doi.org/10.1016/B978-0-08-034341-9.50104-2.

[73] Rao KTV, Yu W, Ritchie RO. Fatigue crack propagation in aluminum-lithium alloy 2090: Part II. small crack behavior. Metall Trans A 1988;19:563–9. https://doi.org/10.1007/BF02649270.

[74] Yoder GR, Pao PS, Imam MA, Cooley LA. Micromechanisms of fatigue facture in Al-Li alloy 2090. In: Sanders TH, Starke EA, editors. Aluminum-Lithium Alloy. Proc. 5th Aluminum-Lithium Conf., 1989, p. 1033–41.

[75] Yoder GR, Pao PS, Imam MA, Cooley LA. Prediction of slip-band facet angle in the fatigue crack growth of an AlLi alloy. Scr Metall 1988;22:1241–4. https://doi.org/10.1016/S0036-9748(88)80139-X.

[76] Xu YB, Wang L, Zhang Y, Wang ZG, Hu QZ. Fatigue and Fracture Behavior of an Aluminum-Lithium Alloy 8090-T6 at Ambient and Cryogenic Temperature. Metall Mater Trans A 1991;22:723–9. https://doi.org/10.1007/BF02670295.

[77] Slavik DC, Blankenship CP, Starke EA, Gangloff RP. Intrinsic fatigue crack growth. Metall Trans A 1993;24:1807–17. https://doi.org/10.1007/BF02657855.

[78] Kim S, Burns JT, Gangloff RP. Fatigue crack formation and growth from localized corrosion in Al–Zn–Mg–Cu. Eng Fract Mech 2009;76:651–67. https://doi.org/10.1016/J.ENGFRACMECH.2008.11.005.

[79] Hoffman ME, Hoffman PC. Corrosion and fatigue research — structural issues and relevance to naval aviation. Int J Fatigue 2001;23:1–10. https://doi.org/10.1016/S0142-1123(01)00115-3.

[80] Hoffman PC. Fleet management issues and technology needs. Int J Fatigue 2009;31:1631–7. https://doi.org/10.1016/J.IJFATIGUE.2008.11.016.

[81] Liu C, Rafla VN, Scully JR, Kelly RG. Mathematical modeling of potential and current distributions for atmospheric corrosion of galvanic coupling in airframe components. NACE - Int. Corros. Conf. Ser., 2015.

[82] Rafla V, Davenport A, Scully JR. Determination of Cathodic and Anodic Charge from Operando X-Ray Tomography Observation of Galvanic Corrosion of Aluminum Alloy 7050-T7451 and 304 Stainless Steel in a Simulated Fastener. CORROSION 2015;71:1300–3. https://doi.org/10.5006/1871.

[83] Rafla V, King AD, Glanvill S, Parsons A, Davenport A, Scully JR. Operando Observation of Galvanic Corrosion Between Aluminum Alloy 7050-T7451 and 304 Stainless Steel in a Simulated Fastener Arrangement Using X-Ray Tomography. CORROSION 2015;71:1171–

6. https://doi.org/10.5006/1813.

[84] Gangloff RP, Kim S. Laboratory characterization and fracture mechanics modeling of corrosion-fatigue interaction for aluminum alloy substitution. 2005.

[85] DuQuesnay D., Underhill P., Britt H. Fatigue crack growth from corrosion damage in 7075-T6511 aluminium alloy under aircraft loading. Int J Fatigue 2003;25:371–7. https://doi.org/10.1016/S0142-1123(02)00168-8.

[86] Campbell FC. Aluminum. Manuf Technol Aerosp Struct Mater 2006:15–92. https://doi.org/10.1016/B978-185617495-4/50002-0.

[87] Burns JT, LARSEN JM, GANGLOFF RP. Driving forces for localized corrosion-to-fatigue crack transition in Al-Zn-Mg-Cu. Fatigue Fract Eng Mater Struct 2011;34:745–73. https://doi.org/10.1111/j.1460-2695.2011.01568.x.

[88] Liao C-M, Olive JM, Gao M, Wei RP. In-Situ Monitoring of Pitting Corrosion in Aluminum Alloy 2024. CORROSION 1998;54:451–8. https://doi.org/10.5006/1.3284873.

[89] Dixit M, Mishra RS, Sankaran KK. Structure–property correlations in Al 7050 and Al 7055 high-strength aluminum alloys. Mater Sci Eng A 2008;478:163–72. https://doi.org/10.1016/J.MSEA.2007.05.116.

[90] Chen JF, Zhen L, Jiang JT, Yang L, Shao WZ, Zhang BY. Microstructures and mechanical properties of age-formed 7050 aluminum alloy. Mater Sci Eng A 2012;539:115–23. https://doi.org/10.1016/J.MSEA.2012.01.067.

[91] Deshpande NU, Gokhale AM, Denzer DK, Liu J. Relationship between fracture toughness, fracture path, and microstructure of 7050 aluminum alloy: Part I. Quantitative characterization. Metall Mater Trans A 1998;29:1191–201. https://doi.org/10.1007/s11661-998-0246-3.

[92] Giummarra C, Thomas B, Rioja R. New aluminum lithium alloys for aerospace applications. Light Met. Technol. Conf., 2007.

[93] Piascik RS, Gangloff RP. Environmental fatigue of an Al-Li-Cu alloy: part I. Intrinsic crack propagation kinetics in hydrogenous environments. Metall Trans A 1991;22:2415–28. https://doi.org/10.1007/BF02665008.

[94] Giummarra C, Rioja R, Bray GH, Magnusent PE, Moran JP. Al-Li alloys: Development of corrosion resistant, high toughness, aluminum-lithium aerospace alloys. Alum. Alloy. Their Phys. Mech. Prop., 2008.

[95] Venkateswararao KT, Yu W, Ritchie RO. Fatigue crack propagation in aluminum- lithium alloy 2090: Part I. long crack behavior. Metall Trans A 1988;19:549–61. https://doi.org/10.1007/BF02649269.

[96] Zhao H, Pan Q, Qin Q, Wu Y, Su X. Effect of the processing parameters of friction stir processing on the microstructure and mechanical properties of 6063 aluminum alloy. Mater Sci Eng A 2019;751:70–9. https://doi.org/10.1016/j.msea.2019.02.064.

[97] Gupta VK, Agnew SR. Fatigue crack surface crystallography near crack initiating particle clusters in precipitation hardened legacy and modern Al–Zn–Mg–Cu alloys. Int J Fatigue 2011;33:1159–74. https://doi.org/10.1016/J.IJFATIGUE.2011.01.018.

[98] Petit J, de Fouquet J, Henaff G. Influence of ambient atmosphere on fatigue crack growth behaviour of metals. Handb Fatigue Crack Propag Met Struct 1994:1159–203. https://doi.org/10.1016/B978-0-444-81645-0.50010-X.

[99] BRANCO R, ANTUNES F V., MARTINS RF. Modelling fatigue crack propagation in CT specimens. Fatigue Fract Eng Mater Struct 2008;31:452–65. https://doi.org/10.1111/j.1460-2695.2008.01241.x.

[100] Ro YJ, Agnew SR, Gangloff RP. Crystallography of fatigue crack propagation in precipitation-hardened Al-Cu-Mg/Li. Metall Mater Trans A Phys Metall Mater Sci 2007;38 A:3042–62. https://doi.org/10.1007/s11661-007-9344-x.

[101] Horstman R, Peters K, Meltzer R, Bruce Vieth M, Towers O. Fatigue Crack Front Shape and Its Effect on Fracture Toughness Measurements. J Test Eval 1983;11:34. https://doi.org/10.1520/jte11584j.

[102] Towers OL, Smith AP. Stress intensity factors for curved crack fronts in compact tension specimens. Int J Fract 1984;25:R43–8. https://doi.org/10.1007/BF01141559.

[103] Glazer J, Verzasconi SL, Dadler ENC, Yu W, Emigh RA, Ritchie RO, et al. Cryogenic Mechanical Properties of Al-Cu-Li-Zr alloy 2090. Adv. Cryognic Eng. Mater., 1986, p. 397–404.

[104] Venkateswara Rao KT, Hayashigatani HF, Yu W, Ritchie RO. On the fracture toughness of aluminum-lithium alloy 2090-T8E41 at ambient and cryogenic temperatures. Scr Metall 1988;22:93–8. https://doi.org/10.1016/S0036-9748(88)80312-0.

[105] Rao KTV, Ritchie RO. Fracture-toughness behavior of 2090-T83 aluminiumlithium alloy sheet at ambient and cryogenic temperatures. Scr Metall 1989;23:1129–34. https://doi.org/10.1016/0036-9748(89)90313-X.

[106] Rao KTV, Ritchie RO. Mechanisms influencing the cryogenic fracture-toughness behavior of aluminum-lithium alloys. Acta Metall Mater 1990;38:2309–26. https://doi.org/10.1016/0956-7151(90)90098-2.

[107] Jata K V., Starke Jr. EA. Fracture Toughness of Al-Li-X Alloys at Ambient And Cryogenic Temperatures. Scr Metall 1988;22:1553–6.

[108] Chu D, Tseng C, Morris JW. Microstructural Influence on the Work Hardening of Aluminum-Lithium Alloy 2090 at Cryogenic Temperatures. Materials (Basel) 1992:37–44. https://doi.org/10.1007/978-1-4757-9050-4_5.

[109] Verkin BII, Grinberg NMM, Serdyuk VAA, Yakovenko LFF. Low temperature fatigue fracture of metals and alloys. Mater Sci Eng 1983;58:145–68. https://doi.org/10.1016/0025-5416(83)90041-1.

[110] Kawasaki T, Nakanishi S, Sawaki Y, Hatanaka K, Yokobori T. Fracture Toughness and Fatigue Crack Propagation in High Strength Steel from Room Temperature to -180 C. Eng Fract Mech 1975;7:465–72.

[111] Yokobori T, Yokobori Jr AT, Kamel A. Dislocation Dynamics Theory for Fatigue Crack Growth. Int J Fract 1975;11:781–8. https://doi.org/10.1017/CBO9781107415324.004.

[112] Yokobori T, Yoshida M. Kinetic Theory Approach to Fatigue Crack Propagation interms of Dislocation Dynamics. Int J Fract 1974;10:467–70. https://doi.org/10.1017/CBO9781107415324.004.

[113] Ro Y, Agnew SR, Gangloff RP. Effect of Environment on Fatigue Crack Wake Dislocation Structure in Al-Cu-Mg. Metall Mater Trans A 2012;43:2275–92. https://doi.org/10.1007/s11661-012-1089-5.

[114] Martin ML, Somerday BP, Ritchie RO, Sofronis P, Robertson IM. Hydrogen-induced intergranular failure in nickel revisited. Acta Mater 2012;60:2739–45. https://doi.org/10.1016/J.ACTAMAT.2012.01.040.

[115] Martin ML, Sofronis P, Robertson IM, Awane T, Murakami Y. A microstructural based understanding of hydrogen-enhanced fatigue of stainless steels. Int J Fatigue 2013;57:28–36. https://doi.org/10.1016/J.IJFATIGUE.2012.08.009.

[116] Findlay SJ, Harrison ND. Why aircraft fail. Mater Today 2002;5:18–25. https://doi.org/10.1016/S1369-7021(02)01138-0.

[117] Shoales GA, Fawaz SA, Walters MR. Compilation of Damage Findings from Multiple Recent Teardown Analysis Programs. ICAF Symp 2009:187–207. https://doi.org/10.1007/978-90-481-2746-7.

[118] Medlar PC, Berens AP, Gunderson A, Gallegher JP. USAF Damage Tolerant Design Handbook: Guidelines For The Analysis and Design of Damage Tolerant Aircraft Strucutres 2002.

[119] Schijve J. Fatigue damage in aircraft structures, not wanted, but tolerated? Int J Fatigue 2009;31:998–1011. https://doi.org/10.1016/j.ijfatigue.2008.05.016.

[120] Grandt AJ. Fundamentals of Structural Integrity: Damage Tolerance Design and Nondestructive Evaluation. Wiley; 2003.

[121] Neves AC, Adey RA, Baynha JMW, Niku SM. Automatic 3D crack growth using BEASY 1997;19:819–27.

[122] McClung RC, Enright MP, Moody JP, Lee Y-D, Sobotka JC, Bhamidipati V, et al. A Comprehensive Framework for Probabilistic Damage Tolerant Design of Aerospace Components. 29th ICAF Symp 2017:7–9.

[123] Craig McClung R, Enright MP, Moody JP, Lee Y Der, Sobotka JC, Bhamidipati V, et al. A general framework for probablistic fracture mechanics analysis of components. ICF 2017 - 14th Int Conf Fract 2017;2:408–9.

[124] Fassina P, Brunella MF, Lazzari L, Re G, Vergani L, Sciuccati A. Effect of hydrogen and low temperature on fatigue crack growth of pipeline steels. Eng Fract Mech 2013;103:10–25. https://doi.org/10.1016/j.engfracmech.2012.09.023.

[125] Shen Y, Huang X, Wang Z, Wei X, Haapasalo M. Low Environmental Temperature Influences the Fatigue Resistance of Nickel-titanium Files. J Endod 2018;44:626–9. https://doi.org/10.1016/j.joen.2017.11.004.

[126] Heuler P, Klätschke H. Generation and use of standardised load spectra and load-time histories. Int. J. Fatigue, vol. 27, Elsevier; 2005, p. 974–90. https://doi.org/10.1016/j.ijfatigue.2004.09.012.

[127] Richard S, Gasquères C, Sarrazin-Baudoux C, Petit J. Coupled influence of microstructure and atmosphere environment on fatigue crack path in new generation Al alloys. Eng Fract Mech 2010;77:1941–52. https://doi.org/10.1016/j.engfracmech.2010.04.027.

[128] Cox J, Pettit D, Langenbeck S. Effect of Temperature on the Fatigue and Fracture Properties of 7475-T761 Aluminum. Fatigue Low Temp 1985:241–56. https://doi.org/10.1520/stp32759s.

[129] Ostash OP, Kostyk EM, Kudryashov VG, Andreiko IM, Skotnikov IA. Low-temperature Cyclic Cracking Resistance of High-Strength Aluminum Alloys in Crack Initiation and Growth Stages 1990;26:281–8.

[130] Ostash OP, Zhmur-Klimenko VT. Fatigue Crack Growth in Metals At Low Temperatures (A Review) 1987;23:124–35.

[131] Burns JT, Gangloff RP, Bush RW. Effect of environment on corrosion induced fatigue crack formation and early propagation in aluminum alloy 7075-T651, Palm Springs, California: DOD NACE Corrosion Conference; 2011.

[132] Herman WA, Hertzberg RW, Jaccard R. A simplified laboratory approach for the prediction of short crack behavior in engineering structures. Fatigue Fract Eng Mater Struct 1988;11:303–20.

[133] En-SB-08-012 Revision D: In-Service Inspection Crack Size Assumptions for Metallic Structures. 2018.

[134] Burns JT, Gupta VK, Agnew SR, Gangloff RP. Effect of low temperature on fatigue crack formation and microstructure-scale propagation in legacy and modern Al-Zn-Mg-Cu alloys. Int J Fatigue 2013;55:268–75. https://doi.org/10.1016/j.ijfatigue.2013.06.025.

[135] Hutchinson JW. Singular behaviour at the end of a tensile crack in a hardening material. J Mech Phys Solids 1968;16:13–31. https://doi.org/10.1016/0022-5096(68)90014-8.

[136] Rice JR, Rosengren GF. Plane strain deformation near a crack tip in a power-law hardening material. J Mech Phys Solids 1968;16:1–12. https://doi.org/10.1016/0022-5096(68)90013-6.

[137] Komaragiri U, Agnew SR, Gangloff RP, Begley MR. The role of macroscopic hardening and

individual length-scales on crack tip stress elevation from phenomenological strain gradient plasticity. J Mech Phys Solids 2008;56:3527–40. https://doi.org/10.1016/j.jmps.2008.08.007.

[138] Scully JR, Young GA. Hydrogen embrittlement and hydrogen environment embrittlment in Al alloys. In: Gangloff RP, Somerday BP, editors. Gaseous Hydrog. Embrittlement Met. Energy Technol., Cambridge, UK: Woodhead Publishing Ltd.; n.d.